INTERACTION OF NANOPARTICLES WITH RF, AC, AND STATIC MAGNETIC FIELDS IN THERMAL AND NON-THERMAL CANCER THERAPY APPLICATIONS

A Dissertation

Presented to

the Faculty of the Department of Electrical and Computer Engineering

University of Houston

In Partial Fulfillment

of the Requirements for the Degree

Doctor of Philosophy

in Electrical Engineering

by

Dhivya Ketharnath

August 2014

INTERACTION OF NANOPARTICLES WITH RF, AC, AND STATIC MAGNETIC FIELDS IN THERMAL AND NON-THERMAL CANCER THERAPY APPLICATIONS

Dhivya Ketharnath

Approved:

Co-Chair of the Committee
Jarek Wosik, Research Professor,
Electrical and Computer Engineering

Co-Chair of the Committee
Wanda Wosik, Associate Professor,
Electrical and Computer Engineering

Committee Members:

David Jackson, Professor,
Electrical and Computer Engineering

Paolo Decuzzi, Senior Member,
Department of Translational Imaging
The Methodist Hospital Research Institute

John H. Miller, Jr., Professor,
Physics

Biana Godin, Assistant Member,
Department of Nanomedicine,
The Methodist Hospital Research Institute

Suresh K. Khator, Associate Dean,
Cullen College of Engineering

Badrinath Roysam, Professor and Chair,
Electrical and Computer Engineering

INTERACTION OF NANOPARTICLES WITH RF, AC, AND STATIC MAGNETIC FIELDS IN THERMAL AND NON-THERMAL CANCER THERAPY APPLICATIONS

An Abstract

of a

Dissertation

Presented to

the Faculty of the Department of Electrical and Computer Engineering

University of Houston

In Partial Fulfillment

of the Requirements for the Degree

Doctor of Philosophy

in Electrical Engineering

by

Dhivya Ketharnath

August 2014

Abstract

Electromagnetics plays a crucial role in the interdisciplinary science of addressing the complex problem of targeted cancer therapy. Thermal therapies such as radio-frequency and microwave hyperthermia and ablation techniques though effective in ablating tumors are non-target specific. The dissertation focus on alternate thermal and non-thermal approaches inducing cancer cell apoptosis by external magnetic fields.

Nanoparticle based target specific *rf* hyperthermia is explored by designing an LCR resonator. Specific Absorption Rate (SAR) of the NPs are determined to quantify *rf* heat enhancement due to the presence of NPs. Interaction of all field components with the NPs and their heat loss origin are investigated to study the SAR discrepancy in literature. Through measurements and finite element method simulations we determine the interaction of axial electric field with the electric double layer at the NPs/protein/ions interface leads to the SAR overestimation. To improve efficiency of NP targeting, a thermal therapy targeting specific heat sensitive ion channels which overcomes the drawbacks of nanoparticle hyperthermia such as particle concentration is explored. A low frequency ferrite core LCR resonator was designed to characterize magnetic nanoparticles in strong magnetic field with improved focusing and selectivity.

A non-thermal approach to induce cancer cell death through mechanical stress on the cell membrane via external magnetic field gradients was developed. The mechanical force acting on the microenvironment of the cell, affects the cytoskeleton which in turn induces internal biochemical forces/interactions which cause apoptosis. Static and *ac* (sweeping) magnetic field gradient generator was designed to be placed in an incubator to study the effects of magnetic force on cancer cell line. Further, the cells are dosed with

magnetic nanoparticles (MNPs) functioning as force enhancers due to the added rotational force under *ac* fields. The field distributions, magnetic field gradient strength are visualized through finite element method simulations of the static and *ac* magnetic field generator. Pancreatic adenocarcinoma cell line, AsPC-1 stained with DRAQ7 are exposed to the magnetic field gradients to observe cell viability.

Table of Contents

List of Figures

List of Tables

Chapter 1 Introduction

Cancer is a major worldwide health concern where more than twice as many people die than from AIDS, malaria, and tuberculosis combined. WHO projects the global cancer deaths are to increase from 7.1 million in 2002 to 11.5 million in 2030, nearly an 80% increase [1-3]. Statistical studies show that over the period 2006-2010, there has been a steady decrease in colorectal, prostrate and lung cancer due to better screening. Decline in cancer incidence rates reflects improvement in screening and prognosis. However, thyroid cancer and liver cancer have the largest increase by 5.4% and 3.7% respectively in adults [2, 4]. The leading cancer types that occur in children are different from adults. The predominant cancer types that occur in children are leukemia (26%), brain and central nervous system (18%) and lymphoma (14%) [2]. Combined treatments including surgery, radiation exposure and chemotherapy have only minimally improved the survival rate in cancer patients. The difficult prognosis for malignant tumors is multi-fold, (i) deep seated tumor limiting surgical efficacy, (ii) the resistance of tumor cells to most cancer cytotoxic agents, (iii) cancer diversity [5].

Over the last few decades, there has been an immense growth is technological innovations leading to path-breaking applications of electromagnetics in the medicine [6]. The advent of electromagnets, permanent magnets and their miniaturization alongside the discovery of superconductivity, allowed for the several medical applications such as in MRI, NMR, SQUID, cardiomagnetism etc. Specifically, electromagnetics in cancer therapy has opened possibilities for alternate methods of diagnostics, imaging and treatments [7]. Thermal therapies using electromagnetic fields such as *rf* and microwave ablations have shown promising results for certain types of cancer [8, 9].

Today's cancer therapies, including thermal ablations, radiation exposure, chemotherapy and surgery have several drawbacks. For instance, *rf* and microwave ablation techniques apart from being invasive have heterogeneous heating which damage healthy tissues [10]. Similarly, chemotherapeutic drugs in the process of killing cancer cells also damage healthy tissues. To improve the treatment efficiency, one of the key issues to be addressed is tumor targeting. Recent developments in nanotechnology has ushered in a new era of nanomedicine, wherein bio-functionalized nanoscale particles efficiently target the cancer at a cellular level [11, 12]. The goal of nanomedicine is to develop a safer and more effective cancer therapy by improving selectivity of tumor targeting at a cellular and sub-cellular level. Nanomedicine has developed rapidly leading to advancements in drug delivery, molecular imaging, diagnostic and treatments using targeted functionalized nanoparticles [13, 14].

Using electromagnetic fields to activate or actuate nanoparticle has gained a lot of interest over the last few years [15]. Recent research show a three-fold electromagnetic actuation of nanoparticles (i) to deliver therapeutic drugs, (ii) act as local heat enhancers and, (iii) act as force enhancers on the cancer cell [11, 16]. Local hyperthermia where temperatures of 45˚C-50˚C are reached can be achieved by targeting bio-conjugated nanoparticles to the tumor site [17-19]. By varying the frequency and strength of the external magnetic field, it is possible to move from local hyperthermia to targeting specific heat sensitive ion channels [20]. Cells are known to contain several heat sensitive ion channels that are affected at much lower temperature. For example the TRPV1 ion channel also known as a capsaicin receptor are activated by reaching temperature greater than 43˚C [21]. Targeting and triggering specific ion channels overcomes the drawbacks of

nanoparticle hyperthermia such as particle concentration. Targeting heat sensitive ion channels can be further combined with drug delivery by using multistage vectors designed to encapsulate drugs and nanoparticles and programmed to deliver them at specific sites. For the purpose of actuating the nanoparticle or multistage vector, magnetic field generators can be designed at specific frequency and power to cause minimum damage to healthy tissue [20].

Novel non-thermal approach of treating cancer using external electromagnetic fields are currently being explored by several research groups. One of the methods, exploits the effects of mechanical stress on the cell microenvironment-cell membrane, cytoplasm and extra cellular matric transducing stress to internal biochemical reactions [22-24]. Stress on the cell can be exerted by utilizing an external magnetic field either static or AC [25, 26]. Further, addition of magnetic nanoparticle can serve as force enhancers to trigger cell physiological changes linked to membrane stress response thereby causing apoptosis [25, 27].

1.1 Thesis outline

In this thesis, thermal and non-thermal approach to cancer therapy was studied in detail from an engineering point of view. Focus was on the device development, such as efficient high frequency and low frequency magnetic field generators. Interaction mechanism of the fields with the magnetic nanoparticles and their thermal and non-thermal effects were studied in depth. In the first chapter, we introduce the applications of electromagnetics in medicine, specifically the role of magnetic fields in cancer therapy. Progress in the field of nanotechnology leading to nanomedicine and eventually its role in cancer therapy is also introduced.

Chapter 2 aims to study the interaction mechanisms of the electromagnetic fields with the human body and their effects, as a result of both thermal and non-thermal interaction mechanisms. Interaction mechanisms that result in temperature change of the tissue/cell are classified as thermal mechanisms. Non-thermal mechanisms are not linked to any temperature change but rather to some other physiological change produced in the tissue/cell. In thermal mechanism the temperature change is facilitated by energy transfer between the EM source and the tissue/cells. Further, we look into a few example of such thermal and non-thermal effects on the human body arising from prolonged exposure to electromagnetic fields such as cell phones. We also explore the medical applications of electromagnetic fields specifically existing thermal and non-thermal cancer therapies.

In Chapter 3, the advent of nanotechnology and its impact on cancer therapeutics leading to the interdisciplinary branch of nanomedicine is described. Nanomedicine offers a unique target specific ability to target the tumor at a cellular and sub-cellular level. Further these nanoscale particles of various shapes and materials can be bio-conjugated with proteins, antibodies to seamlessly adapt to the bio-environment and for enhanced targeting capability. Further, the chapter explores the idea of utilizing the nanoparticles as "heat-enhancers" to cause localized hyperthermia leading to cancer cell death. Specifically, the properties of superparamagnetic iron oxide nanoparticles and their role as heat enhancers.

Rf hyperthermia using magnetic nanoparticles is explored in Chapter 4 both experimentally and via simulation studies. A high frequency *rf* resonator capable of producing both electric and magnetic fields was built to characterize nanoparticles. System calibration, cooling and field measurements are meticulous carried out. Fields generated

were further explored using FEM simulations. Magnetic nanoparticles were measured for their temperature response to the fields and their SARs were calculated.

Extensive research on magnetic nanoparticle characterization has already been carried out. However, the underlying physics behind the reported *rf* heating of magnetic NPs is not fully explored. Besides the well-understood basics of *rf* magnetic field interaction with magnetic NPs very limited literature is available on other heating mechanisms. Furthermore, there are disparities in NPs' heating efficiency measured for colloidal suspensions *in-vitro* and *in-vivo*. In this Chapter 5, we aim to demystify the disparities by understanding better the magnetic field generator. The different fields generated by the solenoid were studied as an electromagnetic problem. Further, they are delineated to observe the individual field effects on the MNPs and the loss mechanism through experiments and simulation studies.

In chapter 6, a magnetic field generator for thermal trigger of nanoparticles to be used in either dug delivery or to activate heat sensitive ion channels was designed and built. The frequency of the magnetic field was lowered to develop a magnetic field generator with minimum heat deposition to the surrounding tissues. A ferrite core was used to maximize magnetic field and enhance its focusing ability to target a specific area. System characterization, cooling and stabilization are done to achieve maximum field with minimum power input. Further, MNPs were tested in the system and their SAR was calculated.

Non-thermal cancer therapy through magnetic field gradients is explored in Chapter7. A magnetic gradient generator was built to extend force on the cell membrane to trigger apoptosis. First, the various magnetic forces and their dependencies were studied.

Simulations of the magnetic field gradient strength were carried out using COMSOL (FEM) Multiphysics. Further, the device was modified to test for nanoparticles rotational force in their role as force enhances on the cell membrane. Several nanoparticles including iron oxide nanoparticles were tested for rotational movement in AC magnetic field. As a proof of concept, we carried out cell studies using AsPC-1 cells. The effect of static and alternating magnetic field gradients on the cell viability was tested. Cells were dosed with iron oxide nanoparticles to check for increased force and subsequently increased cell death.

As future work, we propose further development of the magnetic field gradient system. Further experiments for the influence of high magnetic field gradients with variable sweeping frequency on NPs and cells. Specifically, the effects of higher magnetic field gradients on cell apoptosis as well as bio-functional linked morphology changes should be investigated.

Chapter 2 Background - Bioelectromagnetics

2.1 Properties of Biological (Lossy) Materials

Classification of biological materials according to their material propertied such as permittivity, conductivity, permeability and depth of penetration is vital to understand their interaction with electromagnetic waves. Depending on these material properties and the frequency of the electromagnetic wave incident, tissue loss vary. Understanding the interaction plays an important role in diagnostics and therapeutic applications of electromagnetic field.

2.1.1 Permittivity and Conductivity

Material parameters such as permittivity, conductivity and permeability account for its interactions with the electric field and magnetic fields. Permittivity accounts for the induced polarization and orientation of permanent dipoles while conductivity accounts for the conduction current for an applied electric field [28]. The complex permittivity of a lossy material is expressed as

$$\varepsilon_c = \varepsilon - j\sigma/\omega, \tag{2.1}$$

where $\varepsilon = \varepsilon_{real}$ accounts for the lossless interaction of bound charges in response to an external electric field. The effective conductivity term $\sigma = \sigma_c + \omega\varepsilon_{imag}$ accounts for the frictional losses due to free charges and polarization respectively. In practice, the complex permittivity is usually represented as $\varepsilon_c = \varepsilon' - j\varepsilon''$ where ε' corresponds to the real part of permittivity and ε'' corresponds to the loss term.

Figure 2-1 shows the plots of relative permittivity for frequency from 10 Hz to 100 GHz for several important biological constituents of varying physical and electrical

properties such as blood, body fluid, fat, muscle, brain grey material and brain white material. The data points are based on experimental data obtained by previous research groups [29, 30]. The relative permittivity of the tissue varies according to its water content. At low frequencies, tissue conductivity dominates the electric field behavior while at higher frequencies permittivity is the dominant factor. This can be observed from the loss tangent, $\tan\delta = \varepsilon^{''}/\varepsilon^{'}$ where $\varepsilon^{''} = \sigma/\omega$.

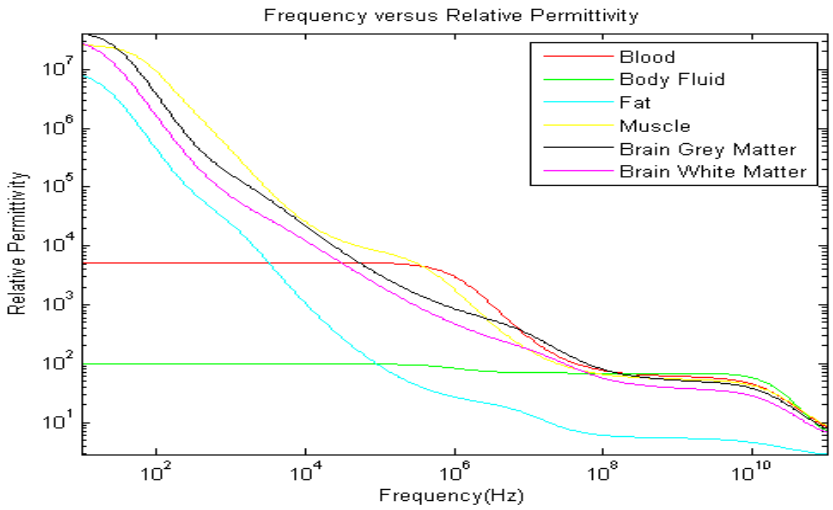

Figure 2-1 Comparison of relative permittivity as a function of frequency of several biological materials

Figure 2-2 and Figure 2-3 show the variation of conductivity and loss tangent as a function of frequency. At higher frequency, the tissues are more conducting and less lossy as expected from Eq. 2.1.

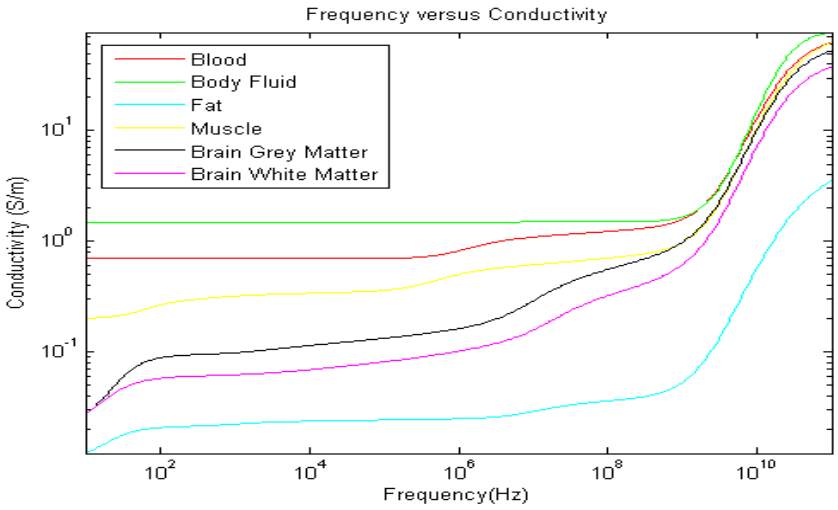

Figure 2-2 Comparison of conductivity as a function of frequency of several biological materials

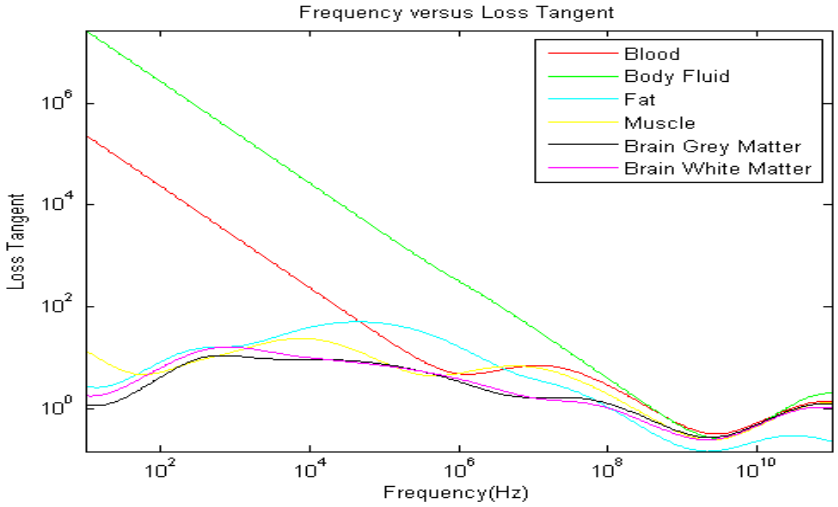

Figure 2-3 Comparison of loss tangent as a function of frequency of several biological materials

2.1.2 Permeability

Magnetic field interaction with magnetic materials occurs through the alignment of magnetic dipoles. The interaction mechanism is dependent on the magnetic properties of the material (ferromagnetic, diamagnetic etc.). The orientation of magnetic dipoles in response to an applied magnetic field is given by permeability. Similar to complex permittivity the complex permeability is given as

$$\mu_c = \mu' - j\mu'', \tag{2.2}$$

where μ' describes the lossless interaction of the material with the external magnetic field and μ'' accounts for the losses involved in the orientation of the magnetic dipoles. The complex permeability in most biological material can be approximated to the permeability of air $\mu_c \sim \mu_o$ since the human body is considered to be weakly magnetic [31].

2.1.3 Depth of Penetration and Propagation:

In a lossy material, the magnitude of the incident wave decreases exponentially as it propagates through the medium. The propagation constant is defined as

$$\gamma = \alpha + j\beta = j\omega\sqrt{\mu_c \varepsilon_c}, \tag{2.3}$$

where, α is the attenuation constant in nepers per meter which represents how fast the wave attenuates and β is the phase constant which describes the phase change as the wave propagates. Expanding the complex permittivity and permeability the attenuation constant can be determined as

$$\alpha + j\beta = j\omega\sqrt{(\mu')(\varepsilon' - j\sigma/\omega)} \text{ and} \tag{2.3}$$

$$\alpha = \omega\sqrt{\frac{\mu'\varepsilon'}{2}\left(\sqrt{1+\left(\sigma/\varepsilon'\omega\right)^2} - 1\right)}. \tag{2.4}$$

The attenuation due to the polarization loss of magnetic dipoles is assumed to be zero since biological materials are weakly magnetic. The depth of penetration is defined as the distance the wave travels before its magnitude drops to 1/e = 0.37 times its original value. It is given by the reciprocal value of the attenuation constant,

$$\delta = \frac{1}{\alpha} \text{ and} \tag{2.5}$$

$$\delta = \frac{1}{\omega\sqrt{\frac{\mu'\varepsilon'}{2}\left(\sqrt{1+\left(\sigma/\varepsilon'\omega\right)^2}-1\right)}}. \tag{2.6}$$

The depth of penetration of the electromagnetic wave decreases as the frequency increases as shown in Figure 2-4. Hence at very high frequencies, the interaction occurs at the surface of the material.

The velocity of propagation of the wave in free space is given by $c = 1/\sqrt{\mu_o \varepsilon_o} = 3\times10^8$ (m/s), which is the velocity of light in vacuum. In a lossy biological medium, the velocity of propagation and wavelength is lower than in free space due to the electrical properties and loss associated with the medium as show in Figure 2-5.

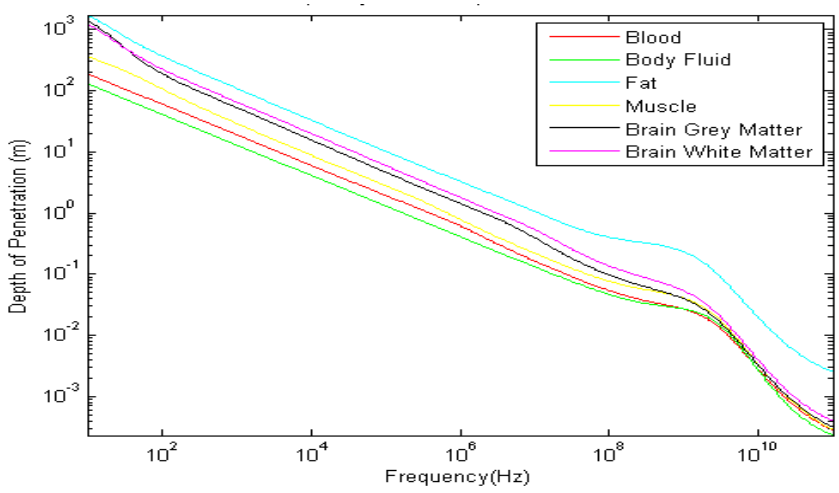

Figure 2-4 Comparison of depth of penetration (DOP) as a function of frequency of several biological materials.

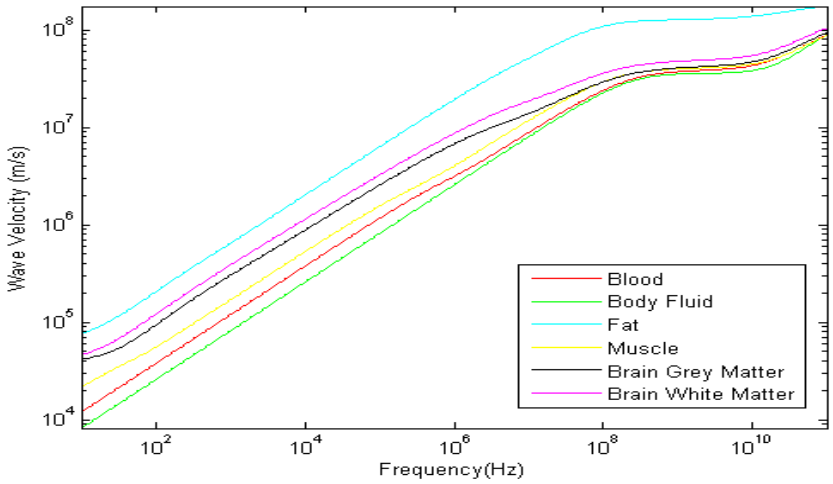

Figure 2-5 Comparison of wave velocity as a function of frequency of several biological materials

Taking into account the properties of the medium the wavelength and propagation velocity can be described as

$$v = \omega/\beta \,[\text{m/s}] \text{ and} \tag{2.7}$$

$$\lambda = v/f = 2\pi/\beta \,[\text{m}]. \tag{2.8}$$

2.1.4 Endogenous Electric Field and Magnetic Fields

To fully understand the interaction of the external electromagnetic wave with the biological material it is necessary to take into account the endogenous electric field generated on the cell membrane. As an example, magnetite in organisms and presence in human beings was studied as a special cases of endogenous magnetic field. Endogenous fields are inherently present in the human body at a cellular level. As example of naturally occurring biological electric and magnetic fields are described subsequently.

2.1.4a Endogenous Electric Field

One of the main sources of endogenous electric field is the cell membrane [32]. The selectively permeable Phospholipid bilayer forms the defining boundary of every cell. The transporter proteins in the cell membrane act as carriers moving molecules inside and

outside the cell. One such transporter protein Na+/K+ ATPase maintains the Na+/K+ ion concentration i.e., high K+ concentration and low Na+ ion concentration internal to the cell. As shown in Figure 2-6, during the Na+/K+ ATPase three Na+ is pumped out for two K+ pumped into the cell giving rise to the negative potential of the membrane.

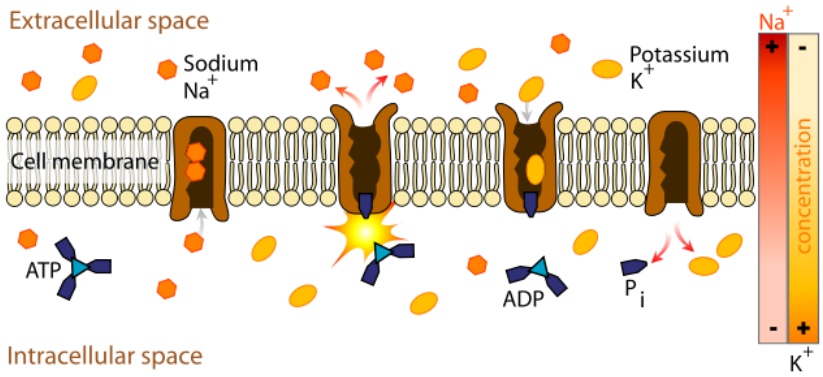

Figure 2-6 Representation of the Na+/K+ ATPase in the plasma membrane

In most cells, the membrane potential is around -70mV i.e., the intracellular potential is -70mV and the extracellular potential is 0V. This potential is referred to as the resting potential and the membrane is said to be polarized. When the potential increases (-60 mV) it is said to be depolarized i.e., positive ions flow into the cell or negative ions flow out of the cell.

The plasma membrane potential influences the transport of a vast array of nutrients in the cell. It is also essential in the signaling processes associated with coordinated movements of cells and organisms and is the basis of cognitive processes. In contrast, ionic disturbances are associated with cell apoptosis [32]. A recent review, [33]discusses the direct impact of the external electric field on the membrane potential and consequently its effect on the biological functions.

2.1.4b Endogenous Magnetic Field

Magnetite is a ferromagnetic iron oxide which is found in many organisms. A well-known example is the magnetotatic bacteria. The single domain biogenic magnetite is used by the bacteria to sense the earth's magnetic field and use it for navigation. Figure 2-9 shows magnetotatic bacteria containing the nano-sized single crystal magnetite [34].

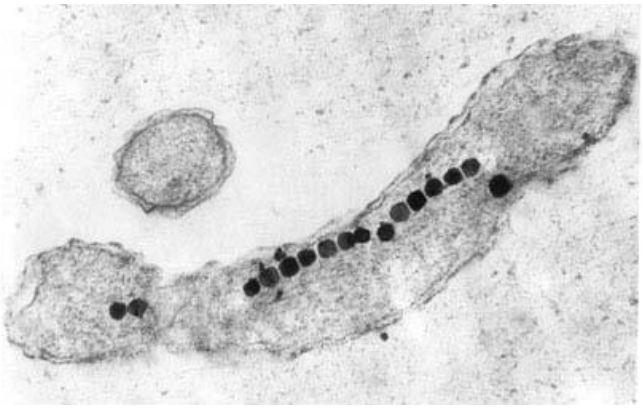

Figure 2-7 Transmission electron micrograph of the magnetotactic bacteria

In general, the human body is considered to be non-magnetic and the permeability is considered to be close to air. However, the presence of magnetite in the human brain was discovered in 1992 [35]. Several recent studies have been pursued to understand the potential role of the magnetite crystals in the neurophysiologic process. In the presence of an external magnetic field these ferromagnetic single crystals in cells can influence a number of ion channel processes [32].

2.2 Interaction Mechanism of Electric and Magnetic fields with Biological Materials

Maxwell's equations describe the source and behavior of the electric and magnetic fields. Electric fields are produced from a time varying magnetic field and/or charge density as shown in the Faraday's and Gauss equations. The strength of the time varying

magnetic field depends on the frequency of the fields. Thus, a higher frequency magnetic field produces a stronger electric field which is also time varying. Similarly, Ampere's law shows that both current density and time varying electric fields produce time varying magnetic fields. The dependence of magnetic field strength on frequency is different in the two cases where it stems from current density and time varying electric field [31].

Faraday's Law is

$$\nabla \times \vec{E} = -\partial \vec{B} / \partial t . \tag{2.9}$$

Ampere's Law is

$$\nabla \times \vec{H} = \vec{J} + \varepsilon \partial \vec{E} / \partial t . \tag{2.10}$$

Gauss Law is

$$\nabla . \vec{E} = \rho / \varepsilon \quad \text{and} \quad \nabla . \vec{B} = 0 . \tag{2.11}$$

2.2.1 Force Exerted by Electric and Magnetic Fields

The fundamental interaction of applied electric and magnetic fields is to exert force on the charges present in the material. The force exerted by the fields is given by Coulomb's and Lorentz law as $\vec{F} = q\vec{E} + q(\vec{v} \times \vec{B})$ [28, 31]. The charges in the material in turn act as a secondary source of electric and magnetic fields inside the material. Thus, a net internal field is set up due to the applied and the induced fields. Response of the applied electric field and magnetic field on a material is given by $\vec{D} = \varepsilon \vec{E}$ where $\vec{D}$ is the electric displacement vector (C/m^2) and $\vec{B} = \mu \vec{H}$ where, $\vec{B}$ is magnetic flux density (T).

2.2.2 Interaction of Electric Field with Non-Magnetic Material

The interaction of electric fields with non-magnetic materials can be broadly classified by the following three mechanisms [7],

- Polarization of bound charges – When an external electric field is applied, the positive nucleus and the electron cloud of the atom in the molecule move in opposite direction resulting in an electric dipole. Figure 2-8a shows the induced polarization caused by an external electric field.
- Orientation of permanent dipoles – Materials that contain an abundance of polar molecules have electric dipoles present even in the absence of an electric field. When an external field is applied, the randomly oriented dipoles align themselves along the direction of the external field. Figure 2-8b shows the alignment of a permanent electric dipole caused by an external electric field.
- Drift of conduction charge – In response to an external electric field loosely bound electrons or ions in a material can move between molecules. The motion of the charge is randomized due to the thermal agitation of the material. The net direction of the charges is along the applied electric field as shown in Figure 2-8c.

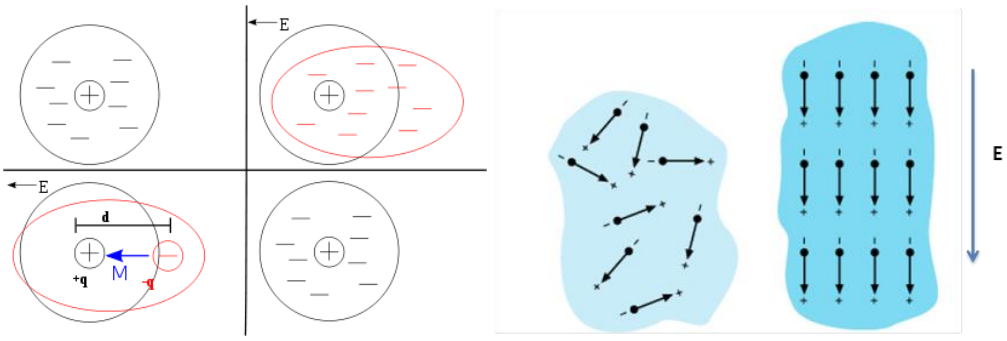

(a) (b)

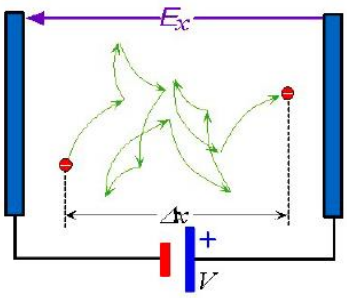

(c)

Figure 2-8 Interaction mechanism of electric field with non-magnetic material (a) Polarization of bound charges (b) Orientation of permanent dipole (c) Drift of conduction charges.

2.2.3 Energy Absorption and SAR

A fundamental aspect of interaction of electromagnetic fields with material is the transfer of energy. From the previously defined equation $\vec{F} = q\vec{E} + q(\vec{v} \times \vec{B})$ it can be seen that electric fields exerts a force on charges i.e., transfer of energy to charges while magnetic field acts in a direction normal to the electric charge changing its direction of motion. Thus, for a sinusoidal steady state electromagnetic field the power in watts transferred to an infinitesimal volume element Δv of the material is given as [31]

$$P = \sigma E_{rms}{}^2 \Delta v \,. \tag{2.17}$$

SAR is defined as the power absorbed by a tissue of mass density ρ in terms of watts per kilogram is given as [31]

$$SAR = \frac{\sigma E_{rms}{}^2}{\rho} \,. \tag{2.18}$$

2.2.4 Radiation and Coupling of Electromagnetic Fields

An important factor governing the energy deposited on the biological material is the radiating efficiency of the electromagnetic wave source. Radiation of EM waves from the source exhibits a frequency dependent behavior. The phenomenon of radiation is most

efficient when the size of the radiating structure is comparable to its wavelength. The wavelength in free space is given as $\lambda=c/f$, hence as the frequency decreases the source size becomes small in comparison to the wavelength and the structure does not radiate efficiently. The electromagnetic spectrum as shown in Figure 2-9 spans over an extremely broad range of frequencies.

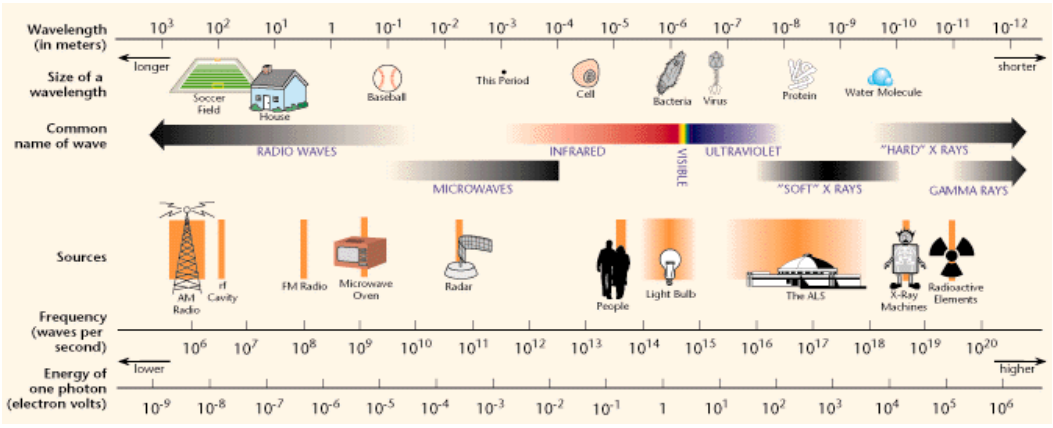

Figure 2-9 Electromagnetic Spectrum

Though Maxwell's equations are valid throughout the electromagnetic spectrum, the solution can take a quasi-static or time-varying approach depending on the wavelength in comparison to the object size. In time varying Maxwell's equations, a time varying electric field creates a time varying magnetic field and vice versa. Thus the electric and magnetic fields are said to be coupled with each other. When the size of the object is comparable to the wavelength the electric and magnetic fields do not vary with time and are said to be uncoupled. In such a case, the electric and magnetic fields can be treated separately since they do not act as sources of each other. This simplified approximation is termed a "quasi-static" approach. Accordingly, they can be classified as follows:

$\lambda>>L$: When the wavelength is greater than the largest dimension 'L' of the object it is incident upon the spatial distribution of the wave is the same as static fields though the

field varies with time. Hence, the electric and magnetic fields are said to be uncoupled as the electric and magnetic fields do not act as sources for each other. The propagation effects of the wave are also negligible due to the uncoupled behavior. Quasi-static EM theory and circuit theory approaches are used as solution methods.

λ=L: In this case the wavelength is comparable to the size of the object and the fields vary with time. Due to the time varying field the electric and magnetic fields act as sources for each other and are therefore said to be coupled. In this range, the electric and magnetic fields are strongly coupled as propagation effects dominate. Maxwell's equations have to be solved without any approximations as in the previous case.

λ<<L: When the size of the object is very large in comparison with the wavelength, the frequency can be usually considered in the upper region of the EM spectrum. Approximate solution methods like the ray theory can be used when the frequency lie in the optical range. The propagation effects of the strongly coupled electric and magnetic fields dominate.

2.2.5 Ionization Energy

The upper part of the electromagnetic spectrum is called ionizing radiation range since the energy of the photons is high enough to cause ionization of atoms. The ionization energy is given as

$$E = hf \text{ [J]}. \tag{2.19}$$

where, h is the Plank's constant of value $6.626\times10^{-34}\,Js$. The energy of the wave increases as the frequency increases. Thus the electromagnetic wave at a very high frequency above the optical frequency has an energy great enough to break molecular bonds. The main components of the body at an atomic level and their chemical bond strength are shown in Table 2-1 [36].

Table 2-1 Chemical bond strength of the main components of the body at an atomic level

Bond Type	eV/bond
N, triple covalent bond	9.5
O, double covalent bond	5.1
C, single covalent bond	3.6
Hydrogen bond	0.1
ATP hydrolysis	0.3

The minimum energy required to ionize a molecule is 1eV, while the ionization energy at 1 GHz is 4μeV, $2x10^{-5}$ smaller than 1eV. Thus for frequencies below 300 Ghz, the energy is too low to cause damage at a molecular level.

2.3 Thermal and Non-Thermal Effects of Electromagnetic fields

The fundamental effect of tissue exposed to high powered electromagnetic field is the increase in temperature. The exposure limit of electromagnetic power deposited in tissue is measured in terms of SAR. However, the heat transport phenomenon in tissues has to be taken into account using the bio-heat equation to obtain a realistic temperature increase. The general formulation of the BHE is given as [31, 32, 37, 38]

$$\nabla \cdot (K \nabla T) + A_o + Q_v - R_L - B(T - T_B) = C\rho \frac{\partial T}{\partial t} \text{ [W/m}^3\text{]}. \qquad (2.20)$$

The terms on the left hand side of the equation give the heat induced, accumulated and lost thus depicting the temperature change given by the right hand side term. The two main mechanisms of heat flow are through conduction and convection. The heat flow through conduction is governed by the Fourier law of heat conduction given as

$$\vec{q} = -KA(T_2 - T_1)\frac{\Delta t}{\Delta L}\,[\mathrm{W/m^2}]. \qquad (2.21)$$

The above equation gives the heat flow through a region of cross sectional area A and length L over a time period Δt where T_2- T_1 is the temperature gradient of the tissue region and K is its thermal conductivity. For heat flow per unit area per unit time in an infinitesimally small volume the equation reduces to

$$\vec{q} = -K\Delta T\,[\mathrm{W/m^2}]. \qquad (2.21)$$

The term $\nabla \cdot (K\nabla T)$ represents the divergence of the heat flux through internal conduction where K is the tissue thermal conductivity [J/sm°C]. Convection loss is described by $B(T - T_B)$ where B is the heat loss due to the blood perfusion [J/sm^3°C] and $T - T_B$ represents the temperature difference between tissue (T) and blood (T_B). $C\rho\frac{\partial T}{\partial t}$ is the thermal heat capacitance where C is the tissue specific heat and ρ is the tissue density. The heat produced by metabolic reactions is given by A_o [J/sm^3]. Q_v is the electromagnetic power absorbed by the tissue which is given by SARρ [J/sm^3] . The BHE along with the thermal boundary condition between the tissue and the external environment describe the temperature distribution inside the body. Numerical methods such as Finite Difference or Finite Element methods are usually used to solve the BHE and the convective boundary conditions.

In the United States the FCC (Federal Communications Commission) requires cellular telephones to have a SAR level at or lower than 1.6 watts per kilogram (1.6 W/kg) for a volume containing a mass of 1g of tissue. The ANSI/IEEE safety guidelines restrict the SAR of 1g of tissue to 1.6W/kg. The ICNIRP safety guideline requires the SAR to be equal to 2W/kg for 10 g of tissue. Increase in temperature adversely affects various body

functions e.g., 4.5℃ increase for 15 minutes produces neurological damage, 10℃ increase causes skin damage [39]while 8℃ is the threshold for muscle tissues [40].

2.3.1 Thermal Effects

Over the recent years, studies have been aimed at understanding the SAR, temperature distribution and their potential risk of causing brain tumors. The proliferation of wireless communication devices has increased the urgency to access the risks involved. To that end, several studies have been conducted by research groups across varied disciplines. An electromagnetic approach to the problem involves assessment of induced field, SAR and temperature increase using numerical methods such as finite element or finite difference methods. Highly heterogeneous models of the human body have been developed with high resolution to closely mimic the human anatomy [41]. The human head model is developed from MRI scans of the human head using high resolution (around 2mm) voxels (volumetric pixels). The high resolution allows for the accurate anatomical modeling by assigning tissue properties (permittivity and conductivity) to the voxels. Several heterogeneous human body models have been developed by various research groups to study induced field and temperature distribution using numerical methods. Figure 2-10 shows results of one such studies [42] where the SAR and temperature increase for a cellular phone (900MHz, 600mW) on a human head model is simulated using FDTD method for 50 minute exposure time. The BHE is also included for a more accurate depiction of the temperature distribution in the human head. It can be observed that the highest value of SAR occurs in the region in contact with the cell phone. Significant absorption can also be seen in the regions of brain that are close to the cell phone.

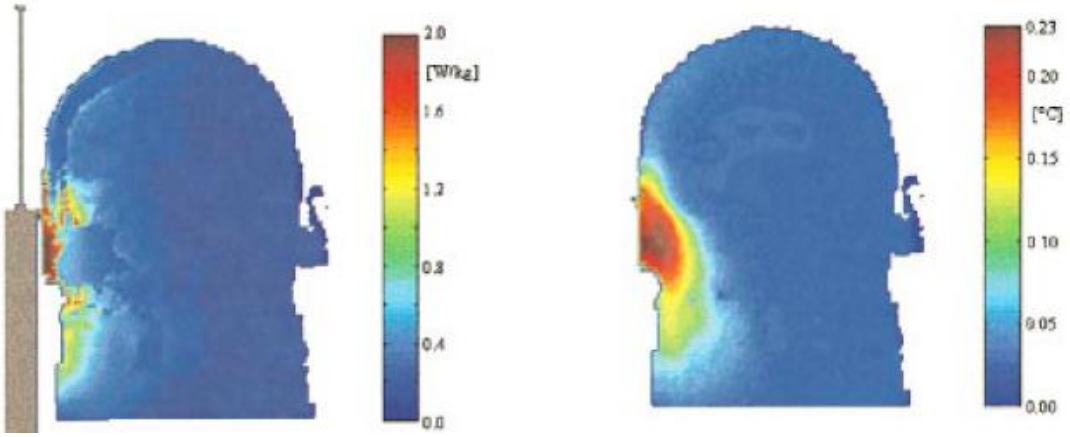

(a) (b)

Figure 2-10 Frontal section of human head model (a) SAR distribution (b) Temperature distribution

An alternate approach of studying the increase in temperature due to cell phone usage through infrared camera as shown in Figure 2-11 [43]. In this study the secondary contributions of temperature increase are also taken into account.

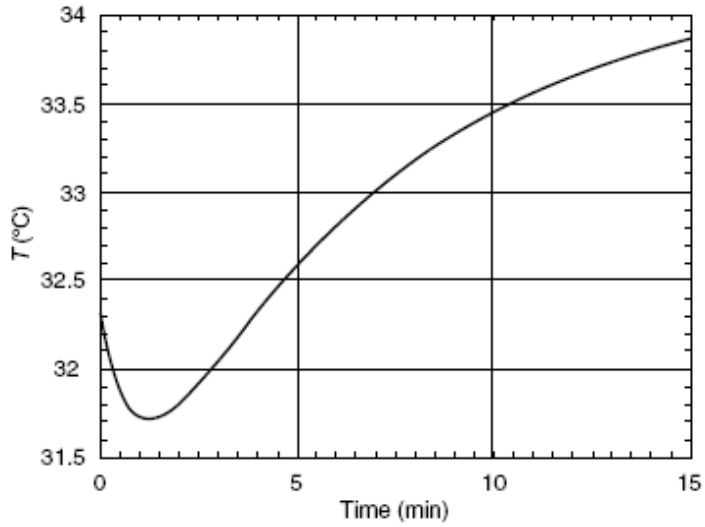

Figure 2-11 Time evolution of temperature at a point on the ear in direct contact with a non-radiating phone.

An initial decrease in temperature can be observed since the phone which is at room temperature (25℃) acts as a sink when placed against the ear. However the temperature

then steadily increases due to the blocked convection loss from the skin in contact with the phone. Figure 2-12 shows the temperature increase in the ear of the test subject for 30 minute exposure to cellular phone (900MHz, 0.21 W).

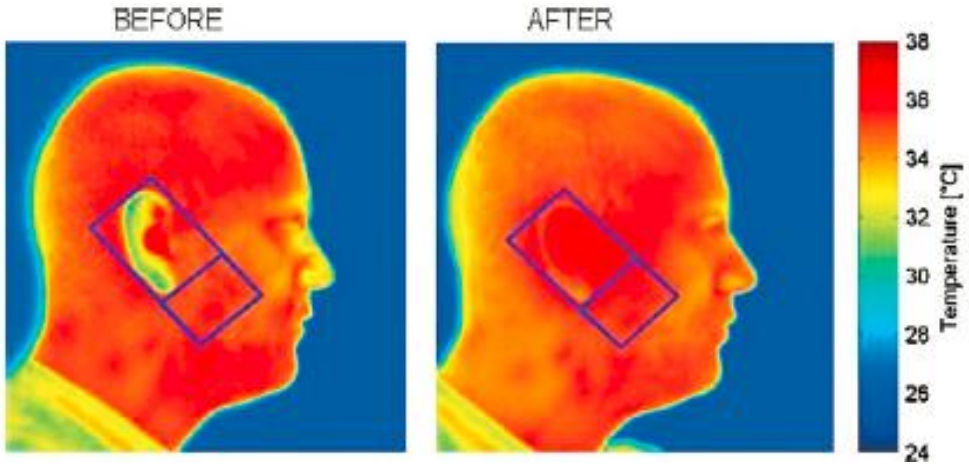

Figure 2-12 IR picture before (left) and after (right) 30 minutes of exposure.

Measured SAR of the instrument was 0.70 W/kg averaged for 1gram of tissue corresponding to the ear region which is well below the guideline value. Significant contact heating effect occurs in the ear and consecutively in the lower part of the brain as observed from Figure 2-12 [43]. Several medical research groups aim at finding plausible correlation between cell phone usage and risk of brain cancer through epidemiologic methods. In a statistical study to link brain cancer to cell phone usage [44], a group of 469 men and women with brain cancer were interviewed and their cell phone usage was compared with a control group of 422 people without cancer. No significant difference in usage was observed and the study does not associate usage of cellular phones to an increased risk of brain cancer. Similar epidemiologic study was conducted [45] by examining the cellular phone usage of a group of 782 patients with brain cancer. The study showed no evidence of a link between increased usage and a higher cancer risk. A classic epidemiologic study

[46] in Sweden studied cellular phone usage of 819 patients and 956 people of the control group. The main difference of this study was the inclusion of the long term effect of cellular phone usage since cellular phones were introduced in 1980s in Sweden. The study showed no evidence of a link between long term usage and a higher cancer risk.

The thermal effect, SAR and potential cancer risks of MRI scan exposure of alternating magnetic fields on human body have been well studied in literature [47-49]. Table 2-2 shows the ratio of local to whole-head average SAR calculated via FEM for a human head model at various frequencies [50]. The local SAR is calculated for 1g or 10 g tissue denoted by SAR_{1g} and SAR_{10g} respectively. The study further compares the SAR values to the permissible limits determined by Food and Drug Administration (FDA) and International Electro-technical Commission (IEC) [50].

Table 2-2 SAR ratio of human head model

Frequency (MHz)	SAR_{1g}/SAR_{w}	SAR_{10g}/SAR_{w}
64	6.1	3.4
128	5.2	3.2
300	6.7	5
FDA	2.7	-
IEC	-	3.12

Several studies have been conducted to study the thermal effects of MRI and the subsequent temperature increase of various tissues. MRI exposure of volunteers show a temperature rise of 2.1˚C and 1.8 ˚C in the scrotal and corneal tissues [51, 52]. The studies show SAR and thermal effects of MRI exposure which is dependent on the thermal, electric

and magnetic properties of each tissue do not reach critical threshold to cause any thermal damage [53].

2.3.2 Non-Thermal Effects

Several groups have studied the effects of high frequency electromagnetic fields i.e., cell phone frequency/usage on the cognitive performance through measurable changes in cerebral blood flow and brain glucose metabolism. A recent study on the change in cerebral blood flow [54]examined a group of 14 healthy individuals through positron emission topography (PET) for cellular phone usage (902 MHz, 0.25W, SAR_{10g} 0.993 W/Kg). The study showed a weak link between exposure (45 minutes) to cellular phones and decreased cerebral blood flow. However, it is contradictory to a similar previous study by Huber et al where exposure (30 minutes) was linked with increase in cerebral blood flow. Another group [55] explored the exposure effect on brain glucose metabolism which serves as a marker of brain activity. The study examined a group of 47 healthy individuals for an exposure time of 50 minutes (for on and off states) using PET analysis. Figure 2-13 shows the increase in glucose metabolism rate for the on state as compared to the off state of the cellular phone (837.8 MHz, SAR 0.91 W/Kg).

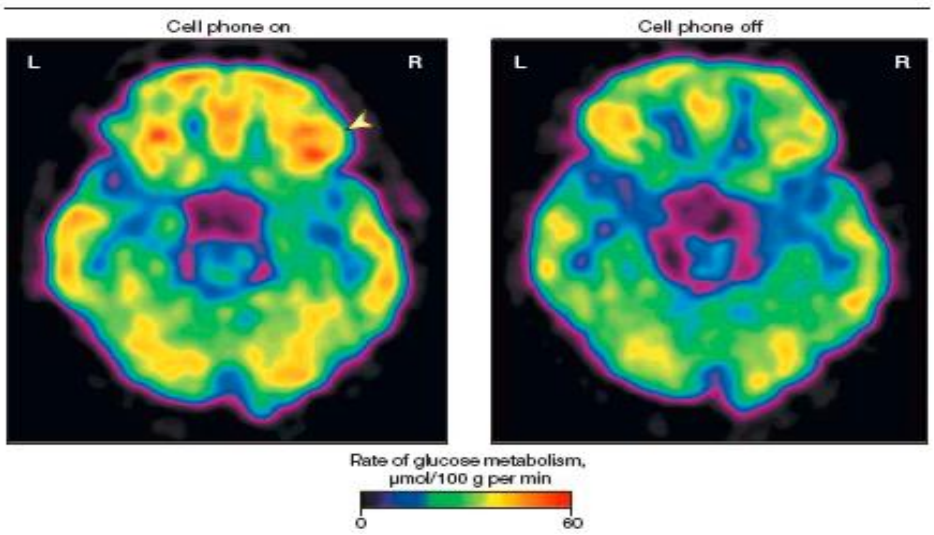

Figure 2-13 Increased glucose metabolism is observed in the right bitofrontal cortex

Though the direct implication of increased brain metabolism is unknown, the study hypothesizes it could affect neuronal activity. The effect of exposure (33 minutes) of 902.4 MHz on cerebral glucose metabolism was examined [56] on a group of 13 healthy male subjects using positron emission topography (PET). The study also shows numerical analysis of a human head model [57] for calculation of SAR from cellular phone exposure. Very slight increase in temperature (<0.25℃) was observed when the subject was monitored continuously by 5 temperature probes thus ruling out the possibility of damage by thermal effects. Figure 2-14 shows decreased cerebral metabolic rate of glucose - CMRglu (which is a better marker of cerebral blood flow).

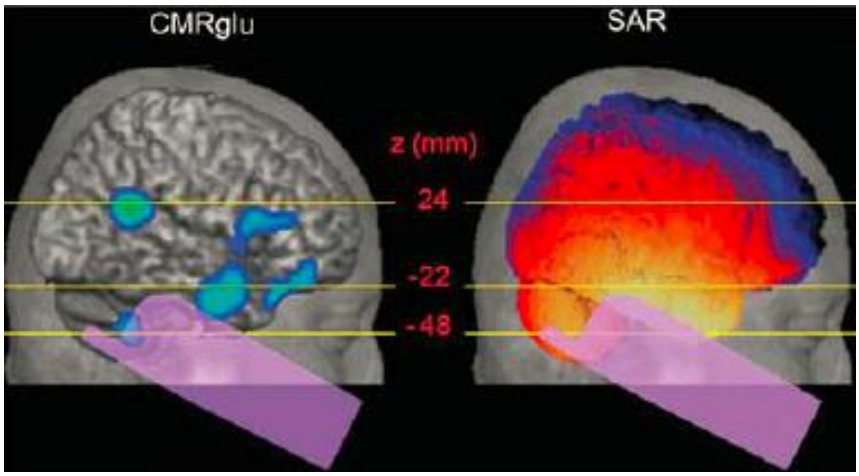

Figure 2-14 Cerebral metabolic rate of glucose (CMRglu) and SAR

It is of significant interest to explore the possibility of non-ionizing electromagnetic fields from the cellular phone to cause damage to neurons, DNA, cell membrane etc. The effect of GSM cellular phone exposure of varying strengths on four groups of 8 rats was examined [58]. The study exposed each group to an average whole body SAR of 2 mW/kg, 20 mW/kg, and 200mW/kg while the fourth group was used as a control with zero

exposure. Figure 15 shows comparison of the central part of the rat brain stained for albumin in the exposed (2mW/kg) and unexposed rat. The study claims that the presence of 'dark neurons' identified by neuropathologists is the consequence of damage of the neurons by non-thermal EMF exposure. The formation of 'dark neurons' have been linked to neuronal damage though they have also been thought of as artifacts produced by post-mortem trauma [59]. The study suggests that the abnormal albumin uptake shown in the Figure 2-15b indicates neuronal change which could be the result of apoptotic cell death.

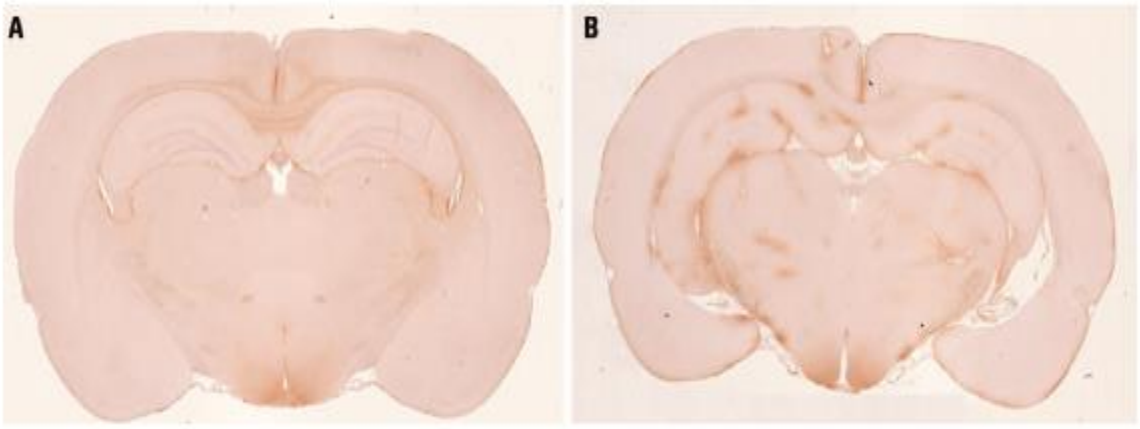

Figure 2-15 Cross-section of central part of brain (a) unexposed rat (b) exposure to SAR of 2 mW/kg for 2 hours

High frequency electromagnetic fields such as cellular frequency have a simultaneous thermal effect and non-thermal effect. In such case, the non-thermal effect can stem from the thermal influence as an additional effect. However, in lower frequencies and static electromagnetic fields the effects as well as the electric/magnetic fields are de-coupled. Exposure of human lymphocytes for 1 hour to simultaneous static magnetic fields of 4.75T and pulsed magnetic field of 0.7mT at 500 MHz have shown to increase the Ca^{2+} influx [60]. On the other hand the same study on Jurkat cells decreased the Ca^{2+} influx, thus showing the effect is dependent on the cell type [61].

Several studies indicate mechanical stress on the cell microenvironment caused by magnetic field gradients leads to internal biochemical reactions [22-24]. Further, under strong magnetic field gradient addition of magnetic nanoparticle can trigger cell physiological changes linked to membrane stress response thereby causing apoptosis [25, 27, 62]. In one such study[63], magnetic field gradient of 41.7 T/m was shows to increase c-Jun protein expression which is linked to cancer proliferation and angiogenesis [64].

2.4 Therapeutic Applications of Electromagnetic fields

The use of electromagnetics for medical applications dates as far back to 46 A.D, where the electric ray was used to alleviate headaches and arthritis. It is the first documented use of harvesting bioelectricity for therapeutics [65]. Through the centuries there have been many breakthroughs in bio-electricity, bio-magnetism and applying them therapeutically [32]. Currently in the medical field, there are numerous applications of electromagnetics in bio-impedance, wound-healing, bone healing and various imaging techniques (MRI, microwave thermography, NMR etc.) [66, 67]. Here we focus on specifically on how electromagnetic fields are used for cancer therapy. Figure 2-16 describes how cancer cells differ from normal healthy cells [68]. Depending on the temperature elevations achieved thermal cancer therapy can be classified into two regimes, (i) Hyperthermia and (ii) Ablation.

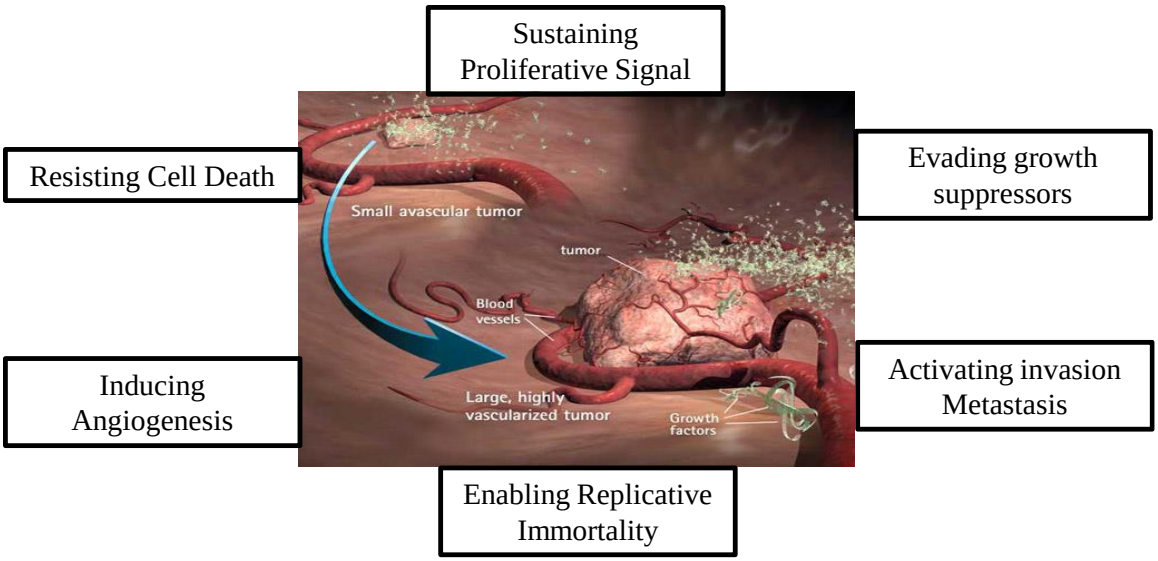

Figure 2-16 Hallmarks of Cancer

2.4.1 Hyperthermia

Hyperthermia defined as elevated body temperature has been used in cancer treatment for several decades. In this thermal therapy the whole body or a specific region is exposed to temperatures in the range of 45˚C - 45˚C. Since cancer cells are more susceptible to heat due to improper vasculature, hyperthermia is employed with minimum damage to healthy tissues [69]. One of the key characteristics of a solid tumor is angiogenesis, i.e., actively recruiting vasculature to feed the growing tumor mass. This phenomenon is exploited in thermal therapy of cancer. Due to angiogenesis in the tumor site which is vital for tumor growth beyond the critical size, the vasculature is irregular, torturous and chaotic leading to regions of hypoxia and low pH levels [70, 71]. The microenvironment of the tumor blood vessels is known to be more permeable and leaky thus lacking the normal cell response to heat i.e., dilation and increased blood flow of vessels for cooling [72]. Inefficient heat dissipation due to the chaotic vasculature renders

the tumor cell more susceptible to hyperthermia in addition to the tumor selectivity due to hypoxia and low pH conditions [73].

2.4.2 Ablation techniques

Target specific tumor ablation procedures such as *rf* ablation (RFA), microwave ablation (MWA) etc. procedures are well recognized methods for thermal treatment of malignant tumor [10]. At temperatures higher than 45˚C irreversible cellular damage occurs leading to death by necrosis. In ablation techniques, the temperature is elevated in the range of 50˚C to 100˚C leading to protein denaturation causing irreversible damage. Irreversible electroporation (IRE) is a non-thermal approach based on membrane permiabilization [74].

2.4.2a Radio frequency ablation

In RFA, the *rf* generator connected to the probe operates at 500 kHz frequency at a power of 200W. In this minimally invasive procedure, the probe is continuously impedance matched with the tissue to ensure maximum power transfer [9]. Figure 2-17 shows the various RFA probe designs available currently.

(a) 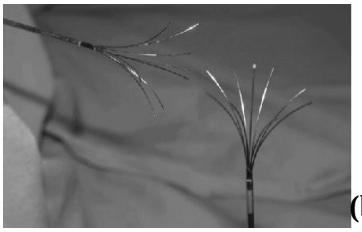 **(b)** 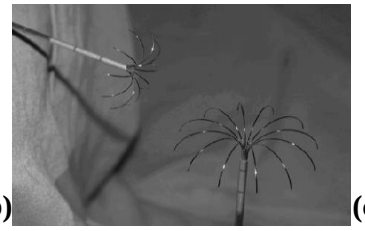 **(c)** 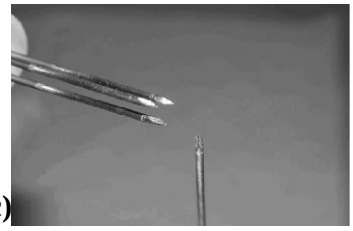

Figure 2-17 Various RFA probe designs from (a) Agiodynamics™, (b) Boston Scientific™, and (c) Radionics™.

Imaging techniques are used to guide the probe to the tumor site. Tumor ablation occurs through Joule heating i.e., high frequency alternating current passing through resistive

medium causes frictional heat. Proper grounding is ensured by grounding pads placed on the patient's thigh.

Improving the specificity of targeting the tumor site continues to be one the most important areas in cancer research. However these invasive methods lack selectivity to cancer tissue and cause thermal necrosis in surrounding healthy tissue. Further in the ablation procedures due to high frequency and high power, local temperatures range from 50˚C to 100˚C leading to tissue bubbling and charring. This in turn causes an impedance mismatch for the ablation probe. Another disadvantage of RFA is the small ablation zone due to the probe size which lead to incomplete ablation of larger tumors [75]. Also, blood vessels at a close proximity to the tumor act as a heat sink thus reducing efficiency of the ablation. The step by step RFA procedure is shown in Figure 2-18 [34].

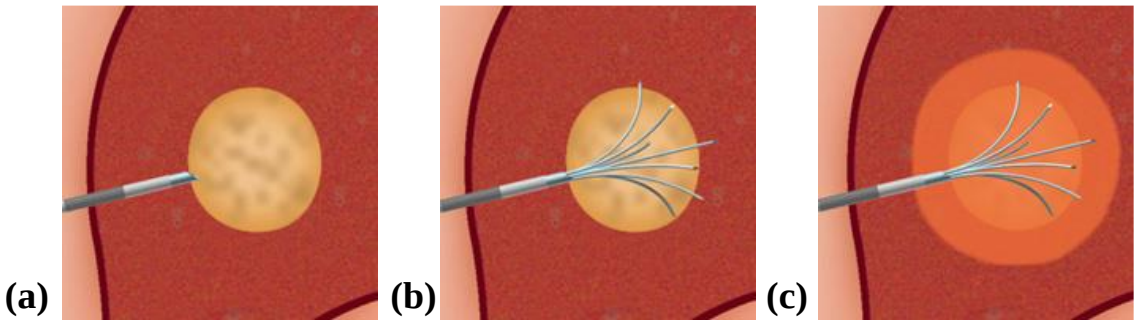

Figure 2-18 RFA procedure (a) probe insertion into solid tumor, (b) extension of prongs, and (c) joule heating.

2.4.2b Microwave ablation

MWA procedure was largely developed in Japan which aims at offsetting certain disadvantage of RFA procedure. MWA procedure operates at the much higher microwave frequency range of 2450 MHz at 60W power [76]. In MWA heat is generated by the polar water molecule oscillation in response to the high frequency alternating current [77]. It is also a minimally invasive procedure done with the guidance of imaging techniques. Some

of the advantage of MWA are greater ablation temperatures, faster ablation, no grounding pads, and larger tumor ablation volumes [78].

2.4.2c Irreversible electroporation

IRE is a non-thermal approach to cancer therapy wherein, a direct current electric field pulse of 50A and 3000V is delivered to the tumor for a time period of 20-100μs [76]. Similar to RFA and MWA, this procedure is minimally invasive and is guided by computed tomography (CT) or ultrasound. The process of IRE as shown in Figure 2-19 occurs once the electrode is inserted into the solid tumor mass applying the pulsing high dc electric field [34]. This strong electric field pulse affects the trans-membrane potential leading to irreversible damage to the lipid bilayer of the cell. As a consequence the electrical fields cause permanent permeabilization and consequent loss of cell homeostasis for those tissues in the treatment zone [79].

(a) 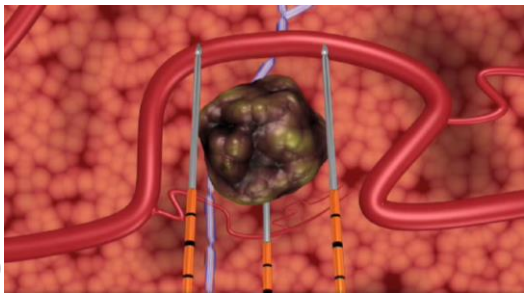 **(b)** 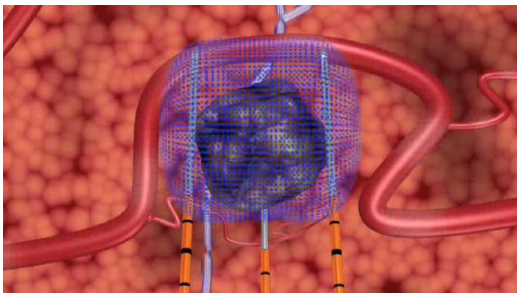

Figure 2-19 Non-thermal IRE showing (a) placement of multiple electrodes (b) application of dc electric pulses.

The cellular mechanics behind cell death and tumour ablation (non-thermal) is linked to the membrane pore caused by the high electric pulse. Schematic view of the process is shown in Figure 2-20 [80]. Once the membrane is permeabilized through the dc electric pulse, it undergoes electroporation i.e., small pores appear on the cell membrane. These pores allow influx of calcium and sodium, and efflux of potassium and also possibly

also of ATP. Usually the production of ATP, influx of calcium, sodium and efflux of potassium is tightly controlled by the Na+/K0+-ATPase i.e., sodium potassium ion pump. These changes in intracellular ion concentrations has a threefold effect (i) it lead to high ATP consumption by the ion pumps, (ii) the increase in calcium may induce mitochondrial permeability transition pore thus greatly reducing ATP production and (iii) activation of lipases and proteases, and generation of reductive oxygen species. This results in severe ATP depletion in the cell causing necrotic cell death.

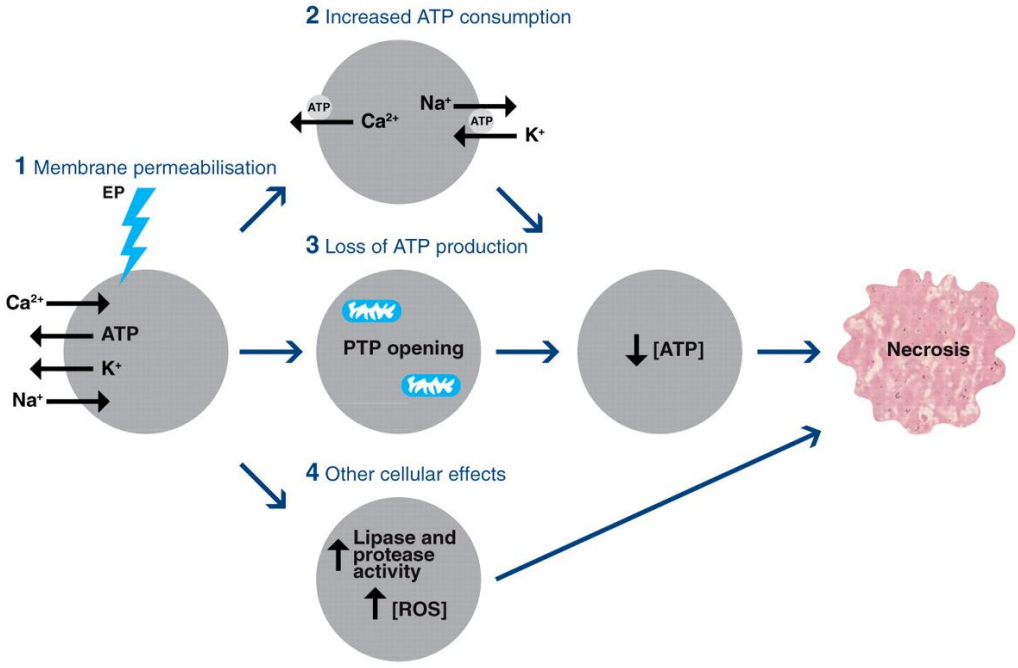

Figure 2-20 Bio mechanism of IRE.

These existing methods such as RFA, MWA and IRE currently used in clinical trials have the inherent disadvantage of being invasive and non-selective. Further, these methods achieve cell death through necrosis marked with cell swelling, release of cytoplasmic contents and inflammatory response [81, 82].

Chapter 3 Background – Nanomedicine

3.1 Nanotechnology

The original concept of nanoscience was envisioned by Dr. Richard Feyman in his famous talk "There's plenty of room at the bottom" [83]. Here he described future scientific ability to work at nanoscale level, controlling individual molecules and atoms. Nanotechnology refers to the interdisciplinary science of manipulating materials at a nanoscale level. The onset of nanotechnology really began with the scanning and tunneling electron microscopes which enabled scientists to see at a nanoscale [84]. Figure 3-1 shows a comparative scale of nanometers in reference to commonplace objects. Nanotechnology has made a huge impact in different disciplines not only due to scaling but rather the ability to utilize the naturally occurring properties of the materials at nanoscale. This brings the entire scientific community closer to nature, since the mechanics in biology, chemistry and physics occur at a nanoscale level. When we consider nanomedicine - the science of applying nanotechnology in medicine, working at nanoscale which is the same scale cellular functions occur, gives scientist and doctors a better chance to fight cancer and other diseases. Interdisciplinary researchers in nanomedicine, utilizing the natural nanoscale of biology are developing therapeutic and diagnostic tools that can detect, target and treat diseases in a more effective and timely fashion as compared to conventional therapies. Nanoparticles in combination with bio-conjugates have been used for the treatment and diagnosis of various physiological abnormalities and disorders like Parkinson's and Alzheimer's diseases, tuberculosis and other lung diseases etc. [85, 86].

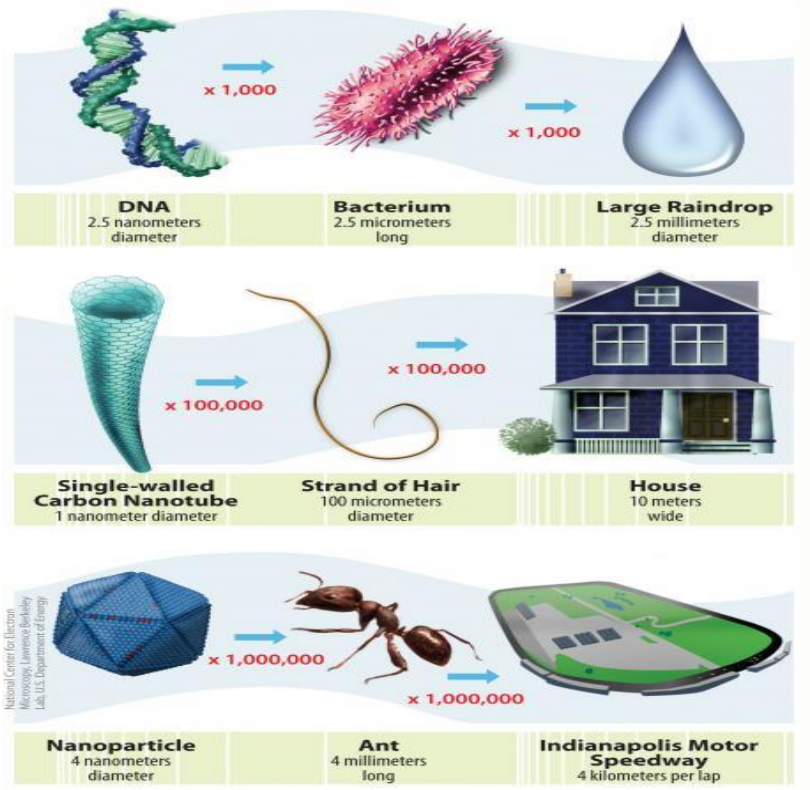

Figure 3-1 Comparative size scale of nanoparticles

3.2 Role of nanoparticles in cancer therapy

In cancer therapy, nanomedicine has received a lot of interest as therapeutic drug carriers, local heat enhancers for hyperthermia, local force enhancers for membrane rupture all aimed at a better targeted cancer treatment [18, 87, 88]. For this purpose the bioconjugated nanoparticles are engineered with controlled material parameters, shapes, sizes, and drug load capacity. Conceptually they are designed to overcome biological barriers while en route to the target tumor and for biocompatibility [89, 90]. Figure 3-2 shows the various possible nanoparticle functionalization for efficient tumor targeting, as contrast agent in imaging, gene therapy, drug delivery etc. [91].

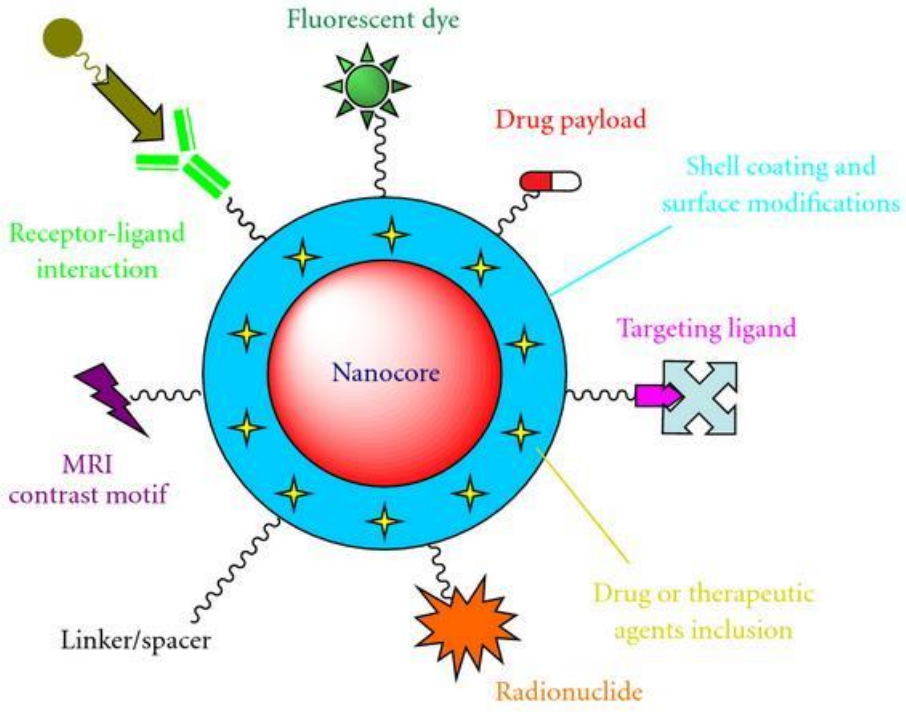

Figure 3-2 Nanoparticle Functionalization

In our work we focus on the actuation phenomenon i.e., the idea of using magnetic fields or electric fields to trigger nanoparticles for either drug delivery, heat enhancement or force enhancement in cancer therapy. In thermal therapy, magnetic nanoparticles functionalized with tumor targeting antibodies for magnetic fluid hyperthermia application have shown promising initial success [19, 92-94]. It has been demonstrated that using an external *rf* source, hyperthermia can be non-invasive and tumor selective [93]. This is due to the excellent tissue penetration of *rf* electromagnetic fields combined with nanoparticles (NPs) working as heat enhancers. The efficient conversion of electromagnetic energy to thermal energy is dependent on properties such as (i) nanoparticle material – dielectric, metallic or magnetic, (ii) electric or magnetic field and, (iii) frequency and strength of the electromagnetic fields. Heating efficacy of several different kinds of nanoparticles such as silica, gold, carbon nanotubes, iron oxide nanoparticles, etc have been studied in both

electric and magnetic field [15, 95, 96]. Understanding the interaction mechanism between the nanoparticle bioconjugate and the electromagnetic fields is vital in designing the nanoparticle and/or the hyperthermia system to ensure maximum heating efficiency. Literature data shows disparity in the reported data for heating efficiency of several nanoparticles [97]. This could possibly arise from the changing microenvironment of the nanoparticle e.g., suspension medium, tumor tissue or healthy tissue. The surface of nanoparticles is electrically charged to achieve monodispersion in a colloidal suspension [98]. Further, nanoparticle surface conjugation of proteins/antibodies for either targeting or drug delivery along with the counter ions adsorbed onto the surface to compensate for the surface charge leads to an Electrical/Electrochemical Double Layer (EDL) [99, 100]. The following sub-sections detail the magnetic nanoparticles and their primary heating mechanisms based on their magnetic and electric field interaction.

3.2.1 Magnetic Nanoparticles:

Over the past decade, magnetic nanoparticles of various sizes have been successfully synthesized and their magnetic properties at nanoscale have been studied [101-103]. Macroscopic magnetic properties are a consequence of magnetic moments of individual electrons. Two factors contribute to the magnetic moment of the electrons (i) orbital motions around the nucleus, (ii) spin around axis either in up or down direction. In the case of an atom, the magnetic field generation is threefold (i) nuclear spin, (ii) electron spin, and (iii) Electron orbital motion [104]. Based on the electronic configuration of each element the magnetic property of the material can be classified as either diamagnetic, paramagnetic or ferromagnetic. In a diamagnetic material all electrons are spin paired hence there is no net magnetic moment. However, in the presence of an external magnetic

field, the spins align in the opposite direction. Paramagnetic material on the other hand exhibit a random spin orientation in the absence of an external magnetic field. With external magnetic field, the spins align along the external field. Materials classified as ferromagnets and their variants have unpaired electron spins with strong atomic interactions leading to magnetization even in the absence of an external magnetic field. In our experiments we focus on iron oxide nanoparticle such as Fe_3O_4 (magnetite) and γ-Fe_2O_4 (hematite) which have generated a lot interest in the nanomedicine community due to their biocompatibility [6]. Taking closer look at these magnetic nanoparticle, from Figure 3-3 we observe how the nanoparticle size affects their magnetic behavior [7]. "MD" refers to a mutidomain particle, where presence of domain walls are the energetically favorable state for the material. As the size decreases, the particle can no longer support a wall and it becomes a single domain "SD" particle. From the Figure 3-3 the difference in coercively of these SD and MD particles can be distinctly observed [104]. Here "PSD" refers to pseudo-single domain particles wherein MD particle exhibit a mixture of SD and MD properties.

MD particles have low coercivity since their magnetization can be easily changed by translating the domain walls which can be done in low field conditions, hence MD's are termed to be magnetically soft. A SD particle on the other hand has high coercivity since the only way to change its magnetization is to rotate the whole particle which is an energetically a difficult process. As the particle size decrease further than SD, at a critical size d_s both its remenance and coercivity go to zero. This particular state is referred to a superparamagnetic "SPM", since the particle starts to exhibit paramagnetic. However, the susceptibility is much higher than a paramagnetic material.

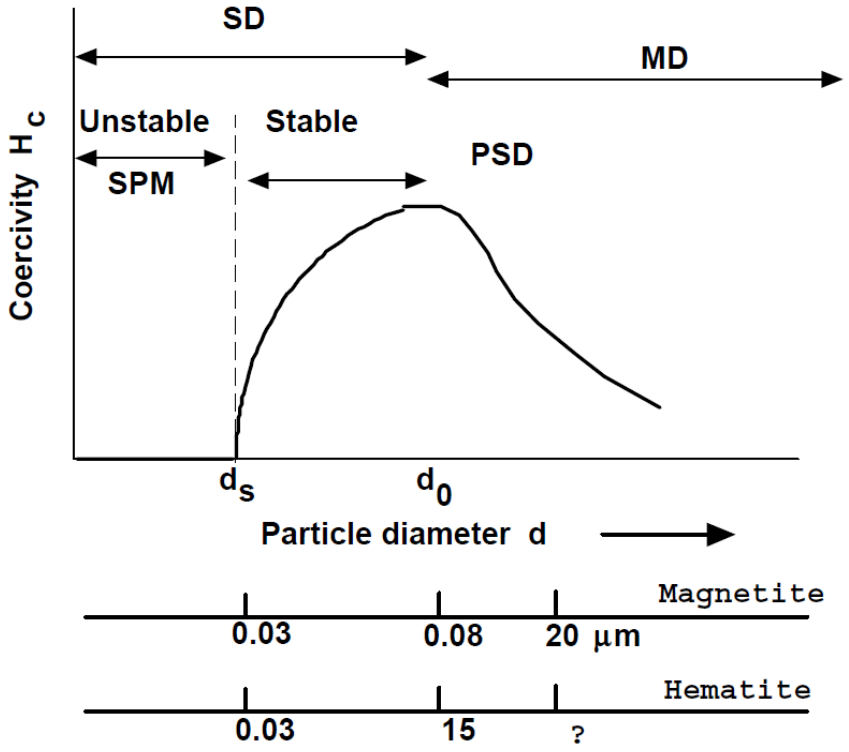

Figure 3-3 Effect of nanoparticle size on magnetic properties of hematite and magnetite.

3.2.2 Heating Mechanism in MNP

In an alternating magnetic field, there are different mechanisms by which magnetic nanoparticles generate heat, (i) eddy currents, (ii) hysteresis loss, (iii) relaxation loss and, (iv) frictional loss is viscous suspensions [6]. In a superparamagnetic iron oxide (SPIO) only the relaxation loss - Neel and Brownian relaxation are predominant, since the particle size is too small to cause any eddy or hysteresis loss. In Neel relaxation process, the magnetic moment rotates in the direction of the external magnetic field generating heat by internal frictional loss. While in Brown relaxation the entire nanoparticle rotates and aligns in response to the external field thereby creating heat by frictional loss due to the viscous drag of the surrounding medium. *Rf* loss will also depend on NPs' size and magnetic properties. In smaller NPs the loss is dominated by Neel relaxation while in larger NPs

Brownian relaxation is the prevailing mechanism [105]. For monodispersed SPIO NPs, assuming no interaction among them, the power loss can be expressed in terms of the NPs' complex susceptibility $\chi=\chi'+i\chi''$, where both components are frequency dependent and the out-of-phase χ'' is directly related to the *rf* loss. Figure 3-4 shows the heat dissipation/SAR for the two relaxation processes as a function of magnetic particle size [106].

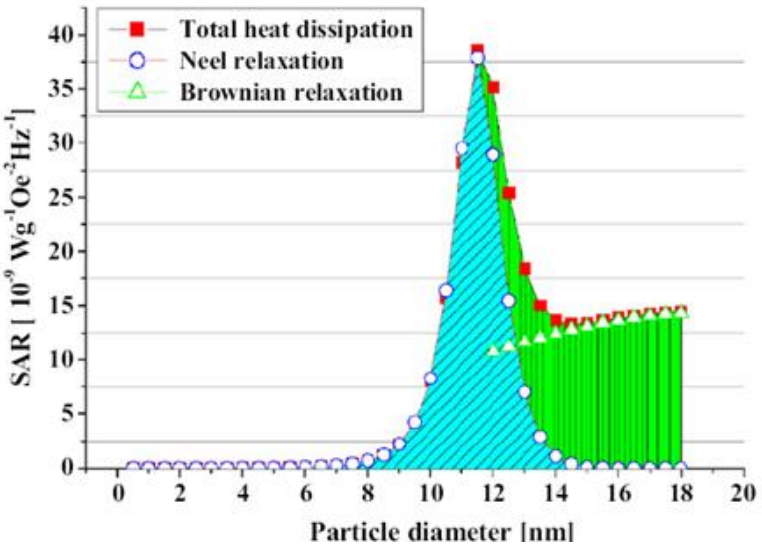

Figure 3-4 Effect of magnetic nanoparticle size on SAR.

Total energy dissipated/heat loss of the MNP in an alternating magnetic field is given as

$$P = p\mu_0 c\Phi H_0^2 f, \tag{3.1}$$

where, H_0 is the magnetic field, f is the frequency, μ_0 is the relative permeability,χ" is the out of phase component of the complex susceptibility $\chi= \chi+j\ \chi$" and is defined as

$$c = \frac{c_0}{1 + j2pft}. \tag{3.2}$$

The real,χ' and out of phase component χ" can be written as

$$\chi' = \frac{\chi_0}{1 + j\left(2\pi f\tau\right)^2} \tag{3.3}$$

and

$$\chi'' = \frac{\chi_0(2\pi f\tau)}{1+j\left(2\pi f\tau\right)^2}. \tag{3.4}$$

Re-writing the power dissipation,

$$P = p\mu_0 c_0 H_0^2 f \frac{2pft}{1+\left(2pft\right)}. \tag{3.5}$$

Here, χ_0 is the equilibrium susceptibility and τ in the effective relaxation time constant,

$$\frac{1}{t} = \frac{1}{t_N} + \frac{1}{t_B}, \tag{3.6}$$

where, τ_N and τ_B are the Néel and Brownian relaxation time constants and are written as

$$\tau_N = \frac{\sqrt{\pi}}{2}\tau_0 \frac{\exp(T)}{\sqrt{\Gamma}} \text{ and} \tag{3.7}$$

$$\tau_B = \frac{3\eta V_H}{k_B T}, \tag{3.8}$$

where, τ_0 is the relation time in response to the thermal fluctuation, T is the temperature, $\Gamma = KV_m/kT$, K is the anisotropy constant, k_B is the Boltzmann's constant, and V_M and V_H are the magnetic and hydrodynamic volumes of the MNP and can be written as

$$V_M = \frac{4\pi R^3}{3} \text{ and} \tag{3.9}$$

$$V_H = \left(\frac{1+\delta}{R}\right)^2 V_M. \tag{3.10}$$

Here, R is the radius of the MNP and δ is the thickness of the bioconjugate/hydrodynamic layer. Further, the equilibrium susceptibility χ_0 is estimated from the Langevin equation as

$$\chi_0 = \chi_i \frac{3}{\xi}\left(coth\,\xi - \frac{1}{\xi} \right), \tag{3.11}$$

where, $\xi = \mu_0 M_d H V_M / kT$ and $M_s = \phi M_d$ in which M_d and M_s are the domain magnetization and the saturation magnetization of MNP respectively, and ϕ is the volume fraction of the magnetization.

Chapter 4 Thermal Cancer Therapy: Nanoparticle Enhanced *Rf* Hyperthermia

In the previous chapters, a brief background on thermal therapies: hyperthermia, ablations probes and role of nanoparticles (NPs) was presented. Nanoparticles (NPs) enhanced *rf* hyperthermia overcomes drawbacks of conventional hyperthermia by combining the excellent tissue penetration of *rf* electromagnetic (EM) waves along with target specific functionalized NPs working as heat enhancers. Here, we discuss in detail *rf* hyperthermia using nanoparticles as heat enhancers.

4.1 Introduction

Several research papers show application of high frequency electromagnetic fields result is significant heating of colloidal nanoparticles [15, 69, 93]. The heating efficiency of the nanoparticles has a twofold dependency, the electromagnetic field generator and the material properties of the nanoparticle. Several biocompatible magnetic and metallic nanoparticles such as gold and superparamagnetic iron oxide (SPIO) have been shown to have significant heating efficiency [92]. Nanovectors engineered using these nanoparticles in a multi-stage fashion combined with antibodies, DNAs and other targeting moieties have been shown to demonstrate capabilities to target cancerous sites [107, 108].

The electromagnetic field generator in the *rf* range is either alternating electric field or magnetic field or a combination of the two. From the device point of view, the heating efficiency is dependent on the frequency, input power and the field strength [6]. Our goal in this chapter is to maximize the SAR of the NPs with reasonable input power and field strength to minimize any non-specific heating. To this end, we built a resonant LCR system capable of producing both electric (capacitive heating) and magnetic field (inductive

heating). This high frequency LCR resonator was designed to study the sample in both electric and magnetic fields ranging up to 100 kV/m and 50 kA/m respectively operating in a frequency range of 12-50 MHz. Further, the design goal priority was to achieve high Q-factor (500-600) such that high *rf* fields can be generated by relatively low input power.

4.2 Design of Electromagnetic Field Generator: RF Hyperthermia Setup

4.2.1 LCR Resonator

The electromagnetic field generator was designed using the principle of a LCR series resonant circuit. A circuit is said to be in resonance when the average stored magnetic energy in the inductors and electric energies in the capacitors of the circuit are equal, i.e., $X_L = X_C$. The basic LCR series resonant circuit is shown in Figure 4-1. At resonance, the impedance of the circuit is minimum, i.e., $Z = \sqrt{R^2 + (X_L - X_C)^2} = R$. The frequency at which resonance occurs is termed as resonant frequency and is defined as $\omega_r = 1/\sqrt{LC}$.

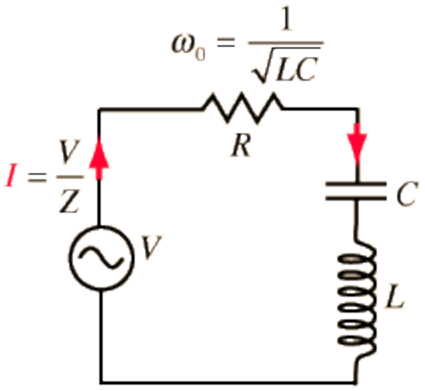

Figure 4-1 Circuit diagram of RLC resonator.

The quality factor (Q-factor) describes the selectivity of the circuit i.e., narrowband frequency response. Mathematically, it is given as the ratio between energy stored to

energy dissipated per cycle in the resonant circuit and higher Q-factor refers to lower loss. At resonance, quality factor can be expressed as $Q = \frac{\omega_r L}{R} = \frac{\omega_r}{RC}$. Thus Q increases with increasing inductance and decreasing resistance and capacitance. The design goal of the applicator was to achieve as high as possible electric/magnetic fields. Critical matching of the applicator to the power supply and high Q-factor helped achieve such goal.

4.2.2 RF hyperthermia system description

The high frequency LCR resonator was designed to study the sample in both electric and magnetic fields ranging up to 100 kV/m and 50 kA/m respectively, in 12-50 MHz frequency range at low input power. This high Q (500-600) resonator can generate high *rf* fields and requires relatively low input power, because at the resonance *rf* fields are amplified by Q-factor. In such configuration *rf* energy is dissipated mainly in the resonator and not in the whole system which simplifies temperature stabilization of the setup. A block diagram of the experimental set up is represented in Figure 4-2. The resonator's capacitor was constructed with two copper plates separated by 12 mm thick single crystal sapphire (ε_r=11, tanδ=10^{-5}). The resonator's solenoid was made of six turns of copper tube wound into a coil of diameter 40 mm and distance per turn of 0.1 mm. A sapphire block of dimension, l = 22 mm (along x axis),w = 12 mm (along y-axis), h = 45 mm (along z-axis) was used as the dielectric inside the inductor which funtions as a constant temperature heat sink. To achieve a high quality factor (Q), oxygen free copper metal was used to build the capacitive plates and the inductive coils. High dielectric constant and low loss of the sapphire further increases the Q-factor. The design of the resonator enabled the sample to be held in a quartz tube positioned in cylindrical cavities drilled in the capacitor's and solenoid's sapphire. NPs samples are placed a quartz tube of inner and outer diameter of

approximately 2.8 mm and 3.9 mm respectively. The parallel plate capacitor consists of copper plates of area 3 mm^2 thickness each seperated by a sapphire dielectric ($\varepsilon_r = 10$) of thickness 12 mm.

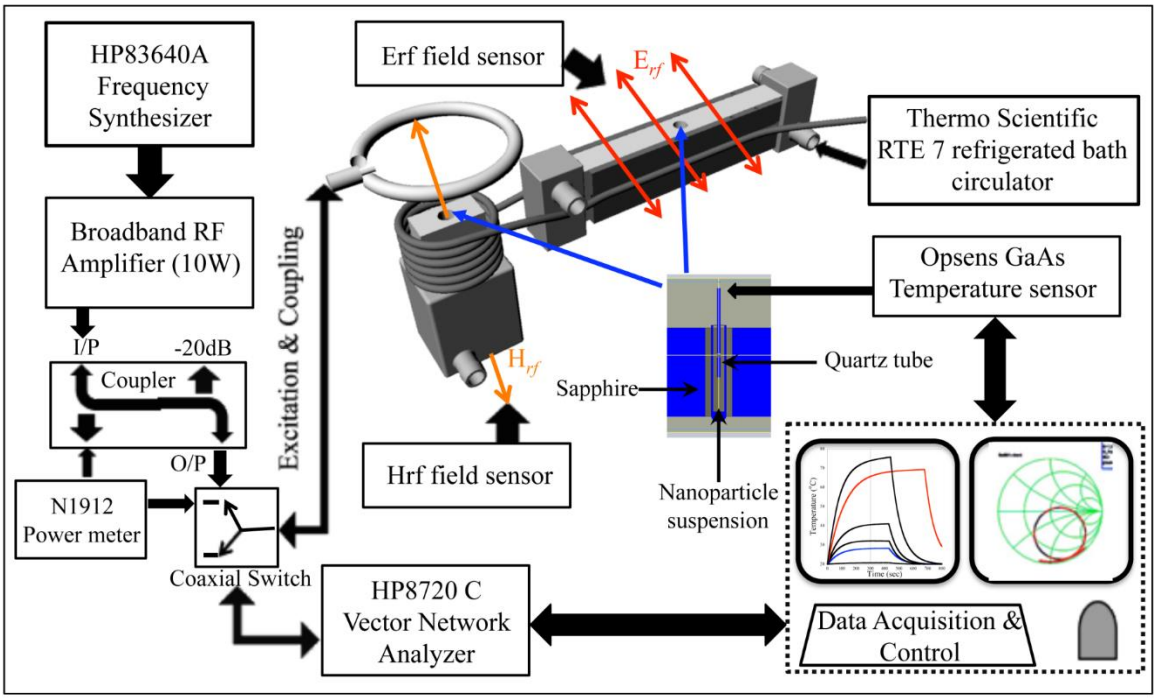

Figure 4-2 *Rf* heating measurement set-up with water-cooled LCR resonator consisting of a parallel plate capacitor and solenoid.

Capacitance of the parallel plate capacitor is given as

$$C = \frac{\varepsilon_o \varepsilon_r A}{d}. \tag{4.1}$$

The capacitor was conncted via copper leads to the solenoid coil of six turns with a pitch 3.5 mm, and diameter 40 mm. Inductance of the solenoid is given as

$$L = \frac{\mu N^2 A}{l}. \tag{4.2}$$

4.2.3 Electric and magnetic field measurements

The LCR resonator was inductively coupled using a single turn coupling loop whose position could be adjusted for critical coupling. Frequency synthesizer (HP 83640A)

and 10 W (1-500 MHz) *rf* amplifier were used to drive the resonator *via* an inductive coupling loop. Resonant frequency of the system was measured using the network analyzer connected to the coupling loop. The network analyzer was controlled by a Labview program which is calibrated for cable losses to give information about the coupling and the Q-factor. The sample size introduced in the capacitor and inductor was small enough not to alter the original field distribution. There is however a small shift is resonant which was measured and corrected. The coupling loop was then connected to a frequency synthesizer to excite the LCR resonator. The experimental setup of the LCR resonator with the sample placed in the solenoid is shown in Figure 4-3.

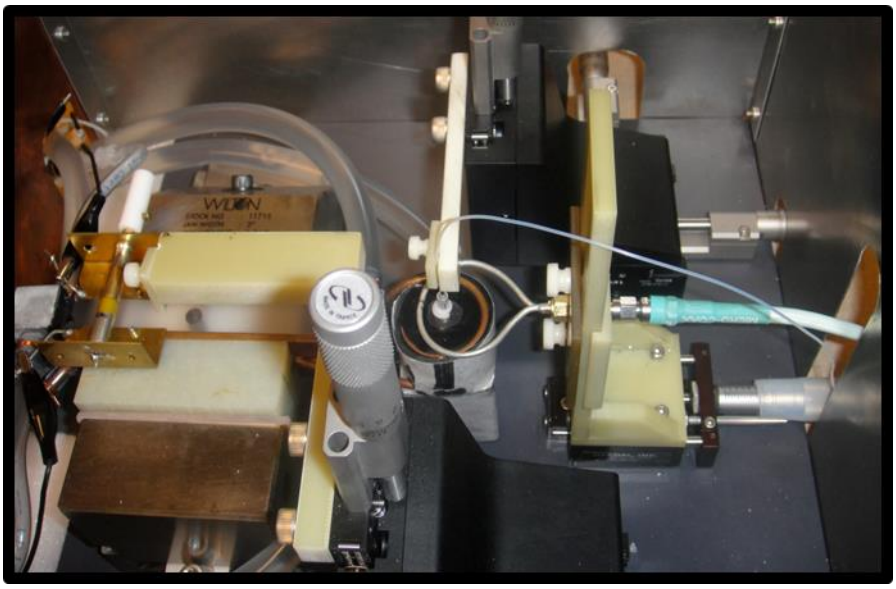

Figure 4-3 Experimental LCR resonator.

The electric and magnetic field in the capacitor and inductor respectively were measured through an oscilloscope. Voltage across the capacitor plates was directly measured in the oscilloscope through a limiting capacitance of 1pF and probe capacitance of 12 pf as seen in Figure 4-4. Voltage across the parallel plates taking into account the limiting capacitance and the parallel plate capacitance,

$$V_{cap} = V_{osc}\left(\frac{C_{probe} + C_{lim}}{C_{lim}}\right). \tag{4.3}$$

From the measured voltage across the parallel plate capacitor the electric field can be determined as

$$E_d = \left(\frac{V_{cap1} - V_{cap2}}{d}\right) = \frac{DV_{cap}}{d}. \tag{4.4}$$

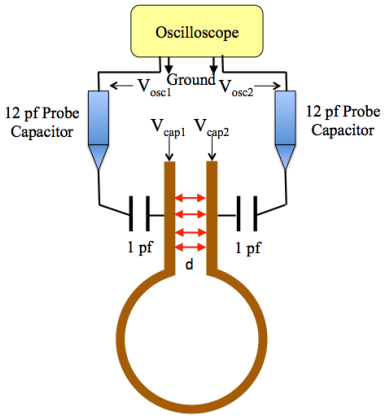

Figure 4-4 Circuit to measure electric field between the capacitor plates.

The magnetic field in the sample region of the solenoid was measured using a small "sniffing loop" or "search coil". The so-called loop was introduced such that the surface area of the "sniffing" loop is parallel to the solenoid coil winding as shown in Figure 4-5. A voltage induced by the axial magnetic field on the loop was measured using an oscilloscope. Peak to peak B-field was determined as follows from the induced voltage,

$$B_{pp} = V_{pp} / \omega NA, \tag{4.5}$$

where ω is the resonant frequency, N is number of loops and A is the area of "sniffing loop".

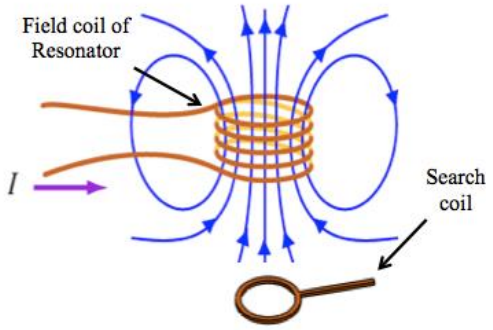

Figure 4-5 Measurement of magnetic field using search coil.

4.2.4 Temperature stabilization and measurement of sample temperature

The sapphire crystals, copper plates and windings were all water-cooled by a refrigerated bath circulator (Thermo Scientific) to maintain a constant sink temperature of 20°C. Sapphire's high thermal conductivity also made it a good sink for heat dissipation. Care was taken to ensure that the extraneous heating of the LCR resonant system does not affect/contribute to the NPs heating. To ensure the NPs sample was heated entirely by the electric/magnetic field, a constant temperature water cooler was used to render a constant sink temperature of 20°C. As shown in Figure 4-6, water was circulated through the capacitor plates, the solenoid coil and through cooling pockets at the ends of the sapphire dielectric.

Temperature versus time was recorded by a GaAs (Opsens) sensor controlled by a micro-meter modulated stage translation. The GaAs (Opsens) temperature sensor has a fiber optic probe with a Gallium Arsenide (GaAs) semiconductor crystal at the probe tip. GaAs band gap is temperature dependent and experiences a shift of 0.4nm/Kelvin. The bandgap shift is translated to temperature via an in-built spectrometer and fed into a computer program where we observe temperature increase as a function of time. Any extraneous heat was removed through the water circulation bath around the sample region,

capacitor and solenoid thus minimizing the systemic error in heating efficiency measurements of NPs. The system stability is reflected in the ability of the NPs temperature to reach saturation or equilibrium wherein *rf* temperature increase and convective cooling reach an equilibrium. The initial sample heating, subsequent cooling, equilibrium during *rf* "on" and eventual cooling during *rf* "off" are described in Figure 4-7.

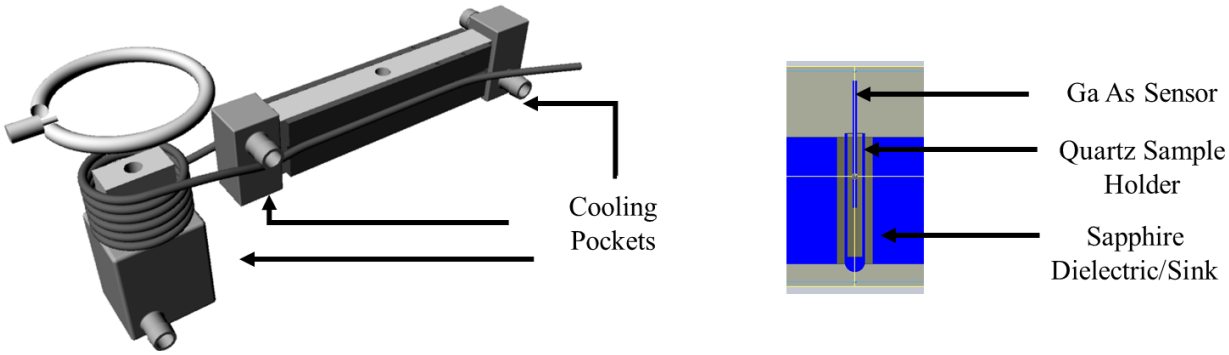

Figure 4-6 LCR resonator and sample cooling.

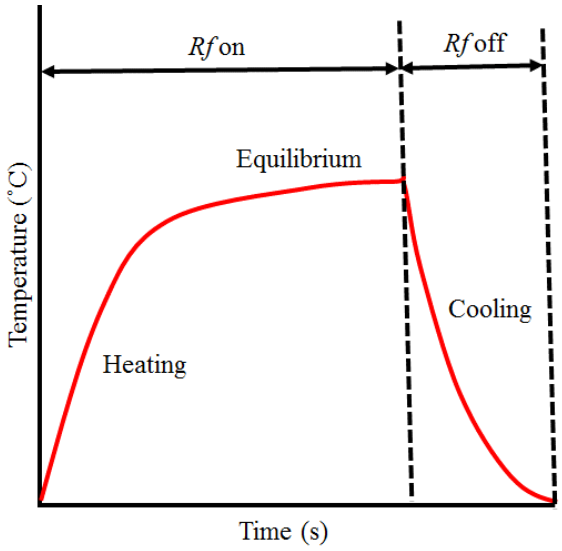

Figure 4-7 Temperature versus time.

4.3 EM Modeling of RF Hyperthermia Setup

Modeling and numerical analysis of the LCR resonator, the electric/magnetic field distribution is important to understand and analyze the different field components and its interaction with the sample. For numerical analysis of the LCR resonator, many EM simulators are available. Some of the important criteria in choosing the correct simulator are (i) frequency range, (ii) computation time and (iii) Method (FEM, MoM, FDTD). Based on these criteria's, for the 30 MHz LCR resonator a Finite Element Method (FEM) simulator HFSS was used.

4.3.1 Ansoft High Frequency Structure Simulator (HFSS)

HFSS is a FEM based 3D full wave simulator [109]. It is primarily used for antenna design solving for S parameters, radiation pattern, efficiency, gain etc. However, areas of application of HFSS ranges from signal integrity, EMC, resonators, radars etc. In the FEM, the structure is discretized into a finite number of volume and surface elements. The basic mesh element is a tetrahedron – a four sided pyramid. The electric or magnetic field inside each tetrahedron is solved by interpolating the nodal values. Accurate representation of the discretized space depend on the choice of the interpolation schemes referred to as a basis functions. While building the geometry, the discretization process which is user controlled is known as meshing. For accuracy of simulation, the geometry representation should be as close as possible to the actual physical structure. However, this can very quickly escalate to an electromagnetically complex problem in terms of both time and CPU resources. Care should be take while modeling edges, complex curvature and thin elements as they always require a fine mesh - smaller mesh size and large number of elements for accuracy.

4.3.2 Setting up solution environment

HFSS offers two solutions modules, driven mode and eigen mode. The driven mode utilizes an input source either current, voltage or wave ports to determine the S parameters and the field values. Eigen mode solver on the other hand has no external source and was used to determine the resonances of the structure, its frequency, Q-factor and the fields. In case of a driven mode approach, HFSS offers multiple variations to determine the solution – single frequency solution, discrete frequency sweep, interpolating frequency sweep and fast frequency sweep. An adaptive iteration of mesh refinement is usually employed in all the solutions types. Here the starting point which is the user defined mesh, is further refined to reduce the error is critical regions (edges, thin elements and curves). In the single frequency solution, only one user defined frequency point is solved for the field distribution. The user defines a range of frequency, usually a rough estimate of where the resonance lies for all the other solution types. In this the step size is also defined either as incremental frequency step or number of frequency points. While probing to check where the resonant frequency lies for the case of an LCR resonator which is a very narrow band response, a small step size is appropriate to capture the response. In discrete frequency sweep, each frequency point is individually solved. Interpolating sweep on the other hand solves for center frequency and uses interpolation for determine the S parameters for the entire frequency range. In this case, the field distribution by default is available only for the center frequency. Similarly, the fast sweep also extrapolates the center frequency solution using Adaptive Lanczos-Pade Sweep (ALPS) solver to fit the entire frequency range. Both Fast and interpolating sweep are most accurate at the center frequency and best when used for a small frequency range.

4.3.3 Geometry, meshing and resonance verification

The LCR resonator was drawn in the HFSS CAD interface to mimic the experimental setup as closely as possible. Similar to the physical system a coupling loop was used to inductively couple with the resonator. Material parameters were appropriately chosen to define the inductor capacitot and the coupling loop as copper. Similarly the dielectric material in the parellel plate capacior and inductor were defined as sapphire. Samples of different permittivity and conductivity were modelled in a quartz tube (ε_r = 3.78) with an inner diameter of 2.5mm and outer diameter of 3 mm positioned at the center of the inductor and capacitor (see Figure 4-6).

The structure was finely meshed in the sample/quartz tube/ air interface regions and at the solenoid for an accurate solution. Care was taken while modeling and meshing the solenoid coil due to the small radius of the copper wire disctritizing such thin curved region results in high aspect ratio elemts known as “skinny” elements which gives rise to erronous results. Modeling the coil exactly as the physical setup by using a cylindrical coil would affect the accuracy of the solution. Hence in our case, the solenoid coil was modeled as a rectangular coil without affecting the field or the resonant frequency.

A rectangular region filled with air was defined around the structure since HFSS by default assumes the background to a perfect conductor. No absorbing boundary conditions were assigned to the air box since the structure is non-radiating. The LCR resonator was excited through a wave port defined at the coupling loop and the air box interface. In HFSS, a waveport simulates the coupling of the structure to the external power source of 1W magnitude. Shown in Figure 4-8 is the geometry of the LCR resonator drawn in HFSS, also included are the coupling loop and the waveport.

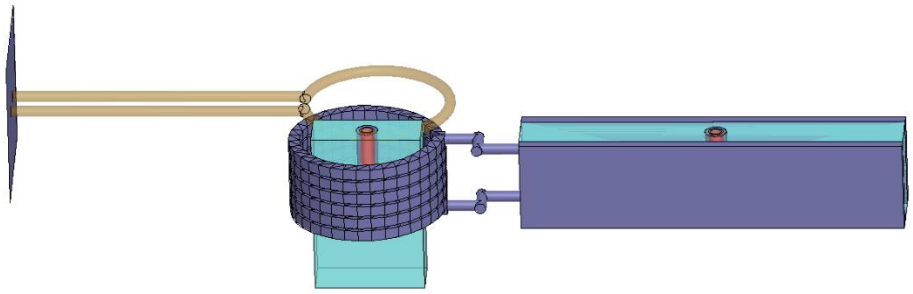

Figure 4-8 Geometry of RLC Resonator in HFSS.

We picked the driven mode to identify the resonance frequency of our structure. Here we ran the interpolated sweep from 10 MHz to 50 MHz to determine the resonant frequency of the LCR resonator. In Figure 4-9, the S11 plot shows a resonant frequency of 30.8 MHz which is the same as the experimental resonant frequency.

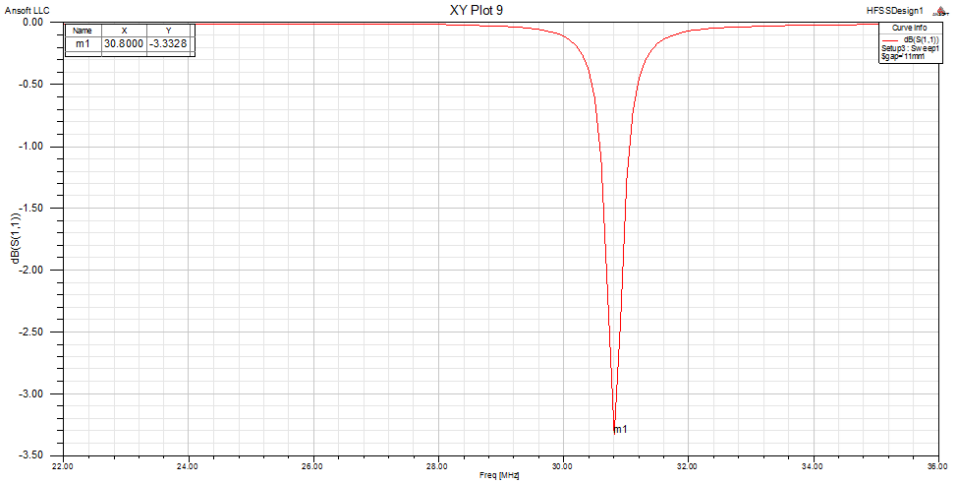

Figure 4-9 Simulated resonant frequency of LCR resonator, f_r = 30.8 MHz.

4.3.4 Visualization of Electric and Magnetic Fields

Once we obtained the correct resonance frequency, the field values at the resonance frequency were extracted. Figure 4-10a shows the electric field in the parallel plate capaciotor. The vector fields show the electric field predominantly in the y-axis which is perpendicular to the two parallel plates. Electric field vector field distribution in the solenoid is shown in Figure 4-10b. The magnetic field distribution along the sample region

(quartz tube) in the solenoid is uniform and field vector H_z is along the length of the quartz tube in the z direction.

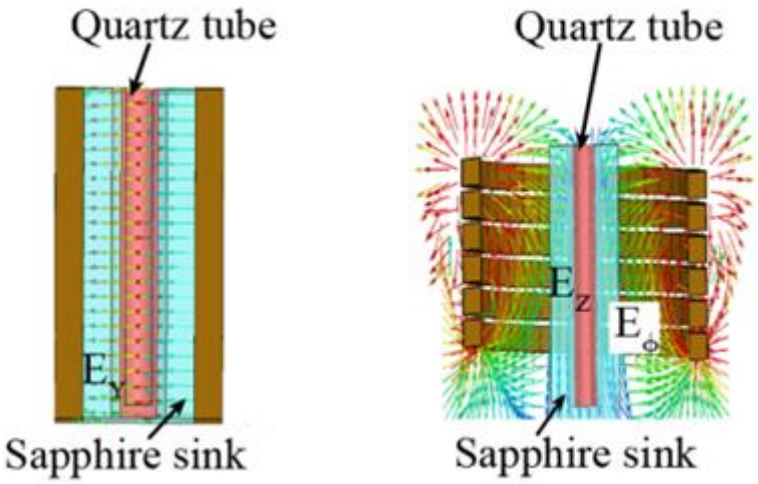

Figure 4-10 Field Measurement Comparison of Electric Field (Ey) in Capacitor and Magnetic Field (H_z) in Solenoid.

While the electric field distribution of the sample region (quartz region) is perpendicular to the electric field, E_y which is along the y-axis. The polarization effect in the capacitor due to the air gap and the quartz tube affects the electric field in the sample region as seen in Figure 4-11. To compensate for this polarization effect, the measured electric field had to be corrected by a factor of $\beta = 0.11$, which is the ratio of the electric field in the sample region to the electric field in the dielectric. Figure 4-12a depicts the magnitude of the axial magnetic field in the solenoid Hz and the electric field in the capacitor Ey when the sample region was assigned material properties of air to mimic an empty quartz tube. In Figure 4-12b the sample region was assigned material properties of saline. We observe that the magnetic field is unaffected by the sample conductivity while the electric field shows marked ionic polarization and screening of the electric field.

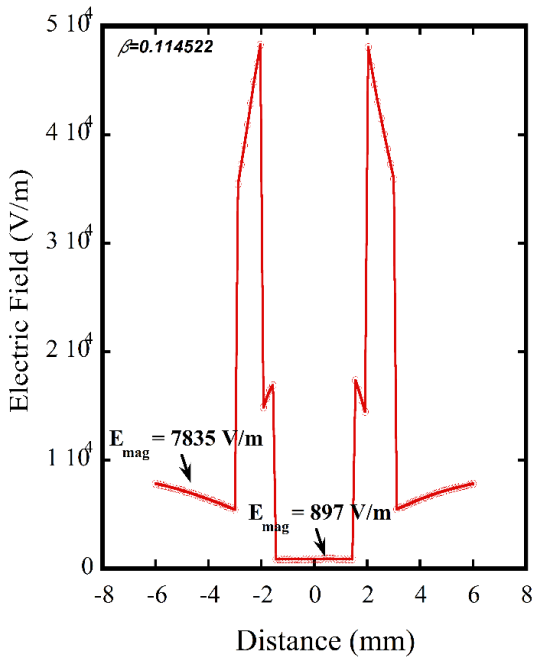

Figure 4-11 Polarization effect of the air gap and quartz tube on the electric field in the capacitor.

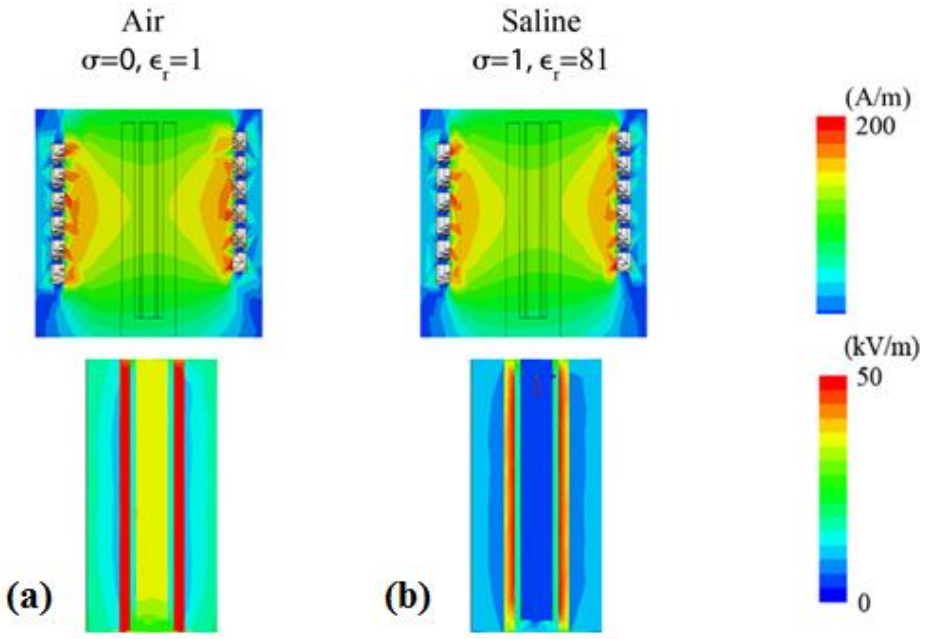

Figure 4-12 Magnetic field and electric field distribution in solenoid and capacitor for (a) air and, (b) Saline.

4.4 Experimental results: electric and magnetic field heating efficiency

Preliminary measurements of NPs heating efficiency were carried out in the LCR resonator in both the electric and magnetic fields. These measurements apart from measuring the heating efficiency of the NPs also help us to understand the various field/NPs interactions that lead to heat dissipation. As a first step, we measured Distilled water (DI water) of resistance 18kΩ in the electric and magnetic field. Temperature as a function of time was recorded for a given input power at 30 MHz frequency. DI Water was measured for electric field strength E_{rf} = 45 kV/m and magnetic field strength H_{rf} = 8 kA/m. The temperature versus time for is shown in Figure 4-15.

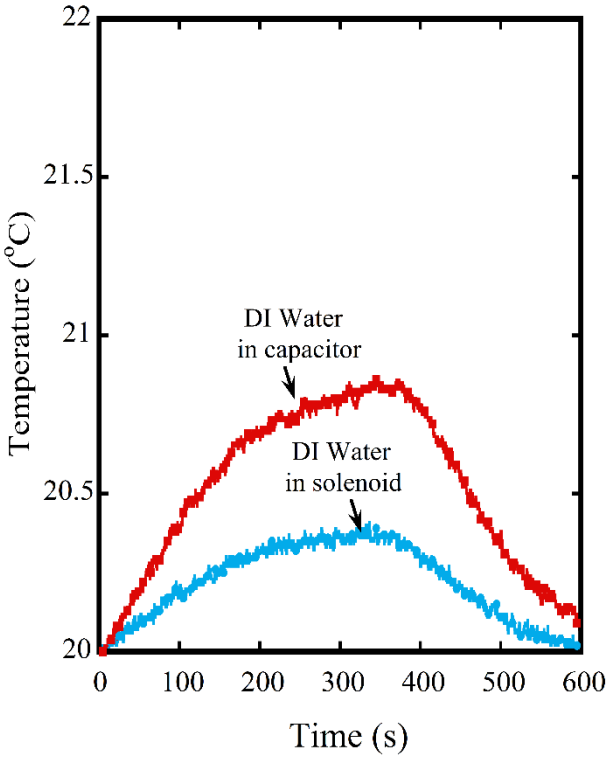

Figure 4-13 Temperature as a function of time for DI Water in the solenoid (blue) and capacitor (red).

The *rf* supply was "on" for the first 400s which represents the sample heating. Once the sample heating starts, with some lag the cooling process also occurs, leading to an

equilibrium plateau. Once the plateau is reached, the *rf* supply was turned "off" and the distinct cooling curve can be observed from 400s to 600s. At 600s we observe the cooling process has completed as the temperature reaches the initial baseline of 20.5˚C.

Next, we measured NaCL of 2.5 mM which is the physiological concentration to observe how the surrounding medium in tissue would respond to *rf* heating at 30 MHz. NaCl was also measured for the same field strength as DI water i.e., electric field strength E_{rf} = 45 kV/m and magnetic field strength H_{rf} = 8 kA/m. Figure 4-16 shows the temperature versus time in capacitor and solenoid. The inset gives the first 20s T vs t from which the slope can be obtained.

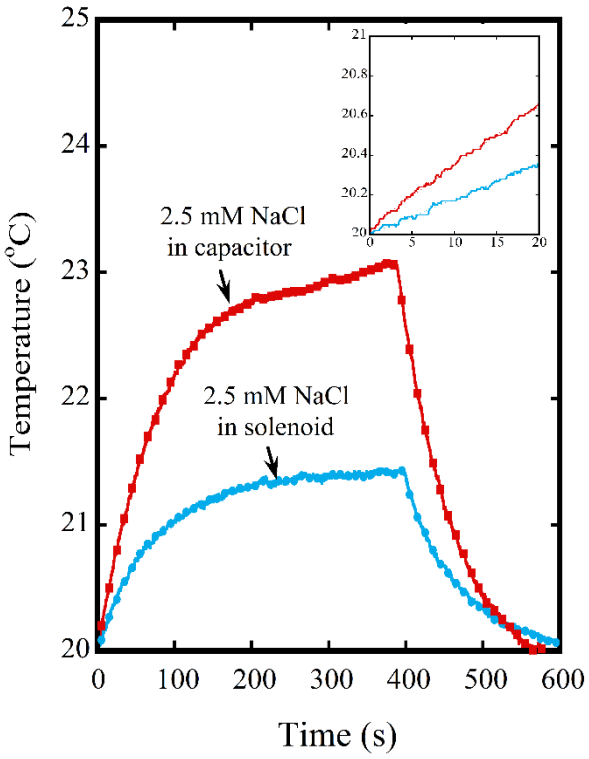

Figure 4-14 Temperature as a function of time for 2.5mM NaCl in the solenoid (blue) and capacitor (red).

Finally, we measured the MNPs response in botht the capacitor and solenoid. For this, we used SPIO NPs samples Sienna+®, purchased from Endomagnetics Ltd. First these

SPIO NPs were characterized for their average diameter, size distribution as well as zeta potential using Malvern Zetasizer. The measurements were carried out in triplicates and the average diameter of dextran surrounded 5 nm iron-oxide cores was found to be ~31.7 nm. These dimensions were also confirmed by scanning electron microscopy analysis. The zeta potential measurements show that the particles have a negative zeta potential (-24.6 mV) which allows them to be in a monodispersed colloidal form. Temperature vs time of two concentrations of SPIO NPs sample (28 mg/mL and 1 mg/mL) was measured for each sample placed in the capacitor and the solenoid as shown in Figure 4-15.

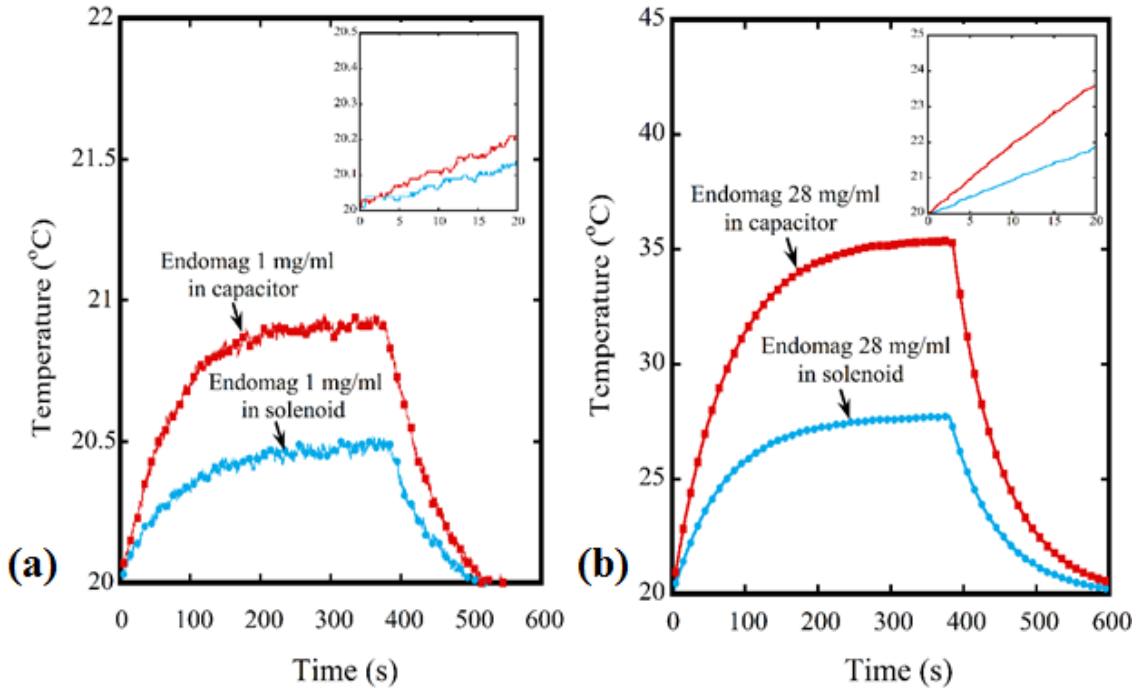

Figure 4-15 Temperature as a function of time for (a) 1 mg/ml Endomag, (b) 28 mg/ml Endomag in the solenoid (blue) and capacitor (red). Inset shows temperature slope in the first 20s.

The heating slopes (q=dT/dt) of the sample was calculated using the first 20s of the temperature vs. time measurements. The slopes are recorded in Table 4-1, where, qc, and qs0 indicate the slopes of the sample measured in capacitor, and solenoid respectively.

Only the first 20s of the heating slope was used to capture the heat dissipation of the sample before the convective/radiative cooling set in.

Table 4-1 Slope values (q=dT/dt) of NaCl and SPIO in the capacitor and solenoid.

Sample	Slope qc	Slope qs
NaCl 2.5mM	0.02557	0.01408
Endomag (28 mg/mL)	0.1832	0.093635
Endomag (1 mg/mL)	0.009255	0.005501

The electric field component across the capacitor plates (corresponding cartesian coordinate, E_y) was measured via an oscilloscope as peak to peak voltage, $V_{p\text{-}p}$. A sniffing loop of radius 2.07mm was used to obtain the axial magnetic field (along z-axis, Hz) component in the sample location of the solenoid.

4.5 *Rf* Power Loss of NPs Samples

Heat loss per unit volume P (W/m^3) of the sample placed in either the capacitor/solenoid can be calorimetrically expressed as

$$P = C_{ps}\rho_s q^m . \tag{4.6}$$

Here, C_{ps} is constant pressure specific heat (J/ (kgK)), ρ_s is the mass density (kg/m^3), q is the slope dT/dt. SAR (P/ρ_s) can also be calorimetrically expressed as $C_{ps}dT/dt$ (W/kg). Electromagnetically the heat loss per unit volume of the sample P (W/m^3) can be expressed in terms of E_{rf} and H_{rf} components as

$$P = \frac{1}{2}\sigma_{sus}\left[\gamma^m\left(\sigma_{sol}\right)\left|E_L^m\right|^2\right] + \pi\mu_0 f \chi^{''}\left|H\right|^2 v_f , \tag{4.7}$$

where, σ represents electric conductivity of the sample, γ(σ) is the depolarization factor due to the free ion charges in the sample, v_f is the volume fraction of NPs in the suspension, E_L is the local electric field in the sample region, f is the resonant frequency, χ" is the magnetic susceptibility of the sample and H is the magnetic field in the solenoid. The superscript *m* refers to the two cases of the sample being placed in the capacitor *c*, solenoid *s0*. Hence, in solenoid $E_L^{s0} = E_s$, and in the capacitor $E_L^c = \beta E_y$ where β = 0.11 is the dielectric polarization screening factor. The depolarization factor $\gamma^m(\sigma)$ for the solenoid is $\gamma^{ss}(\sigma)\equiv 1$ while for the capacitor it can be expressed as a Debye factor since the sample is perpendicular to E_L given as

$$\gamma(\sigma) = \left| \frac{1}{1 + j\left(\frac{\omega_p(\sigma)}{\omega}\right)} \right|^2 = \frac{1}{1 + \left(\frac{\omega_p(\sigma)}{\omega}\right)^2}. \tag{4.8}$$

Here, $\omega_p(\sigma)=\sigma L/\pi a \varepsilon_0 \varepsilon_s$, with sample tube length L=15 mm and inner radius a=1.4 mm. $\varepsilon_0\varepsilon_s$ is the permittivity of the sample and ω is the resonant frequency of the resonator.

The role of MNPs as heat enhancers was studied in this chapter using a LCR resonant. Using EM simulations the fields in the resonator, both the solenoid and the capacitor were analyzed in detail. Further, the heating efficiency of SPIO NPs was confirmed experimentally.

Chapter 5 Additional Influence of Axial Electric Field Component in Solenoid Magnetic Field Generator

5.1 Introduction

It has been demonstrated that *rf* thermal procedures can be non-invasive and cell-selective when an external source of *rf* is combined with either directly or systemically injected functionalized NPs, acting as *rf* absorption enhancers instead of the invasive ablation probe [15, 94, 110]. To quantify heat enhancement due to the presence of the NPs in colloidal and/or physiological liquids their SAR values have to be determined [111]. However, the different field components in a magnetic field generator and their interaction with the nanoparticle suspension have not yet been fully characterized and could lead to discrepancies in SAR values [95, 112, 113]. While the *rf* heating of colloidal suspensions as a whole is well documented [19, 114-116], contribution of medium and EDL heating to overall heating of the NP suspension has generally been neglected [97]. At low frequencies (kHz) the contribution of the dispersion medium to the overall heat loss is negligible. However, this assumption is invalid at higher frequencies (MHz) where the conductive behavior of solution is dominant and hence has an influence on the heating.

In the presence of alternating magnetic (H_{rf}) field, ferromagnetic particle's *rf* loss depends on frequency and area of a hysteresis loop. However, the *rf* loss for single domain ferromagnetic or super-paramagnetic nanoparticles (SPIO NPs) suspended in colloidal fluid is due to the two parallel relaxation processes, Brownian and Neel [117, 118]. In Brownian relaxation, the NPs physically rotates to align with the field while in Neel the magnetic moment rotates internally within the NP. *Rf* loss will also depend on NP's size

and magnetic properties. In smaller NPs the loss is dominated by Neel relaxation while in larger NPs Brownian relaxation is the dominant mechanism [105].

Our goal in this chapter was to accurately quantify the magnetic SAR of SPIO NPs. We experimentally and numerically analyzed the different field components in a solenoid which is the most commonly used applicator to study SAR of MNPs. Once the electric/magnetic field components were identified the *rf* losses due to their interaction with the SPIO NPs was quantified.

5.2 Identification of field components Ez, Eφ, Hz in solenoid

From Faraday's law of induction, the time varying magnetic field H_z for a solenoid configuration shown in Figure 5-1a produces a time-varying electric field referred to as magnetically-induced electric field E_ϕ oriented in the circumferential ϕ-direction. Additionally, an axial electric field E_z also exists due to the scalar electric potential of the coil winding, where ρ, ϕ, z are the cylindrical coordinates [119]. So far, for SAR measurements, only E_ϕ (responsible for eddy currents losses) and H_z (responsible for spin related losses) were considered, whereas existence of the conservative electric field E_z was surprisingly disregarded [14, 15]. However, E_z component shown in Figure 5-1b, in most solenoid configurations is at least in the order of E_ϕ magnitude, and significantly contributes to the total *rf* electric field $E_s=E_\phi+E_z$ and can affect the sample heating [120]. The neglected heating due to interaction of E_z with the EDL of the NPs may lead to an overestimation of SAR. It is thus desirable to identify and delineate the heating of the magnetic NP suspension based on the origin of the electric and magnetic field loss. The effect of E_z in the solenoid is suppressed by imposing perfect-electric-conductor (PEC) boundary condition, where the electric field is normal while the magnetic field is tangential

to the surface. This boundary condition is incorporated by using a cylindrical copper shield with longitudinal single gap or multi gaps (to prevent eddy currents) inserted in the solenoid described in Figure 5-1c.

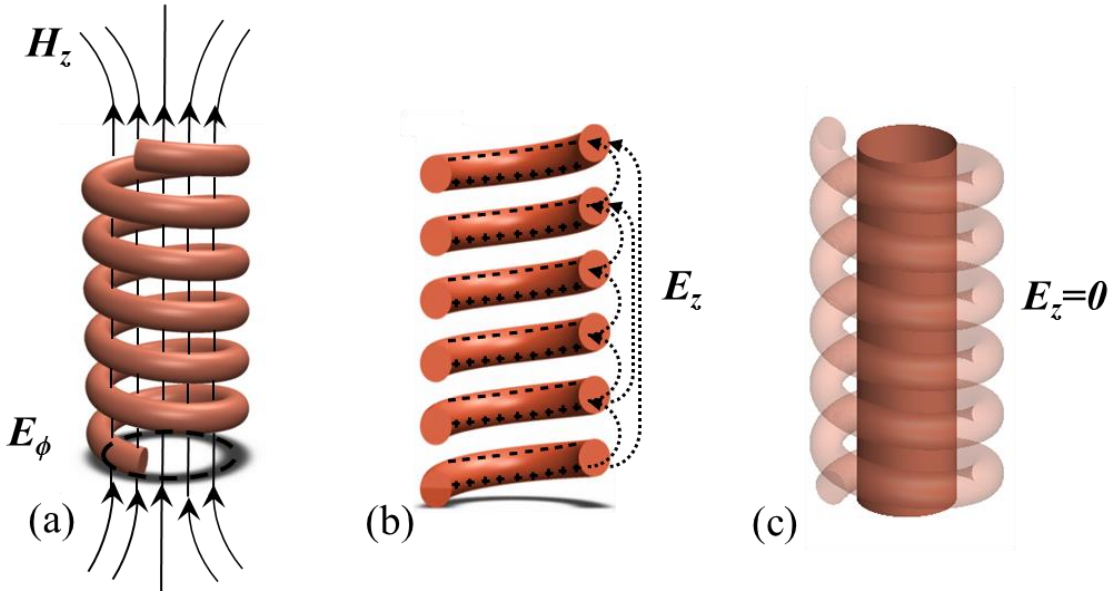

Figure 5-1 Solenoid field components, the well-known (a) axial magnetic field H_z and circumferential E_ϕ electric field (b) the lesser known axial electric field E_z and (c) suppressed E_z field by PEC boundary condition.

5.2.1 Interaction of solenoid fields with colloidal suspension

The conservative electric field component E_z is assumed to affect the EDL interface i.e., the NP/bio-conjugate/solution interface. The conductive ions present in the suspension interact with the circumferential electric field, E_ϕ to produce heat through eddy current loss. In principle, both electric components, E_z and E_ϕ interact with the EDL and the solution. However, the major EDL interaction is from E_z since eddy currents i.e., E_ϕ is minimum at the sample region due to design criteria [17]. This interaction heating has a two-fold dependence on magnitude of E_z and on the EDL. E_z in-turn is dependent on the (i) solenoid geometry, (ii) resonant frequency, and (iii) input power. EDL is dependent on

the (i) NPs surface charge, (ii) protein conjugate and (iii) counter-ions contributing to the significantly larger hydrodynamic radius of the NPs. The magnetic field component H_z interacts with the Brownian and Néel relaxation processes *rf* loss for single domain ferromagnetic or super-paramagnetic nanoparticles [121, 122]. In Brownian relaxation, the NP physically rotates to align with the field while in Néel relaxation the magnetic moment rotates internally within the NP. In smaller NPs the loss is dominated by Neel relaxation while in larger NPs Brownian relaxation is the prevailing mechanism [105]. The three different field components and their interaction with the SPIO NPs suspension is described in Figure 5-2.

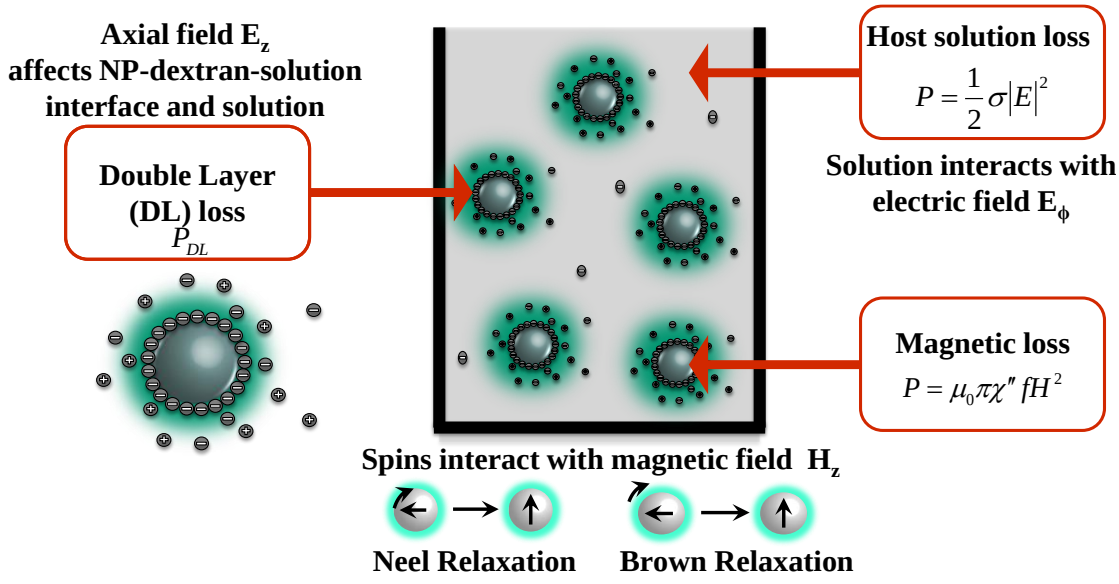

Figure 5-2 Interaction of fields in the solenoid with a nanoparticle suspension describing heating mechanism of nanoparticles in magnetic field.

5.2.2 Analytical calculation of field components

Formulations [119] to calculate the field components in a solenoid are based on the assumption that radius of the coil $a \ll \lambda$, height of the coil $H \ll \lambda$. In our case, at an operating frequency of 30 MHz the wavelength is $\lambda = 10$m. Hence, both the criteria are fully satisfied

for a = 0.0015 m, and H = 0.021 m. The E_ϕ component was calculated at the edge of the coil where it is maximum. Eq. 5.1 describes the analytical form of the axial magnetic field H_z,

$$H_z = \frac{I\cos(\omega t)}{d}. \tag{5.1}$$

Here I is the input current fed into the solenoid, ω is the radial frequency of the solenoid coil and d defines the spacing between the turns of the solenoid combined with the diameter of the coil. Strength of the conservative electric field as seen from Eq. 5.2 is directly proportional to the square of the coil radius,

$$E_z = \left(\frac{\omega\mu_0 aI\cot\psi}{2d}\right)\sin(\omega t). \tag{5.2}$$

Pitch angle is defined through $\cot\psi = \left(\frac{2\pi a}{d}\right)$. At the surface of the coil, to satisfy the PEC boundary condition the total electric field tangential to the coil goes to zero, $E_\phi\cos\psi + E_z\sin\psi = 0$. Thus at the edge of the solenoid, the circumferential electric field E_ϕ is given as

$$E_\phi = \frac{-E_z}{\cot\psi}. \tag{5.3}$$

From Eq. 5.2 and Eq. 5.3 the conservative electric field E_z and the circumferential electric field E_ϕ are plotted in Figure 5-3 and Figure 5-4 for increasing pitch angle. The pitch is varied from 0.1 mm to 5mm for four different frequencies, 30 Mhz (blue), 300 kHz (orange), 100 kHz (gray) and 1 kHz (yellow). Dimensions of the solenoid used for the calculations are D = 40 mm and a = 1.5 mm. Calculations shown are for an input current of 10 A. From the calculations, we see the maximum E_z component value for minimum

pitch i.e., a tightly wound solenoid. This is in accordance with the origin of the E_z component, surface charge accumulation which has a capacitive effect. E_ϕ tendencies shown in Figure 5-1 are at the edge of coil, where it is maximum. We see a similar trend here due to the E_z E_ϕ relation, but with almost an order of magnitude difference.

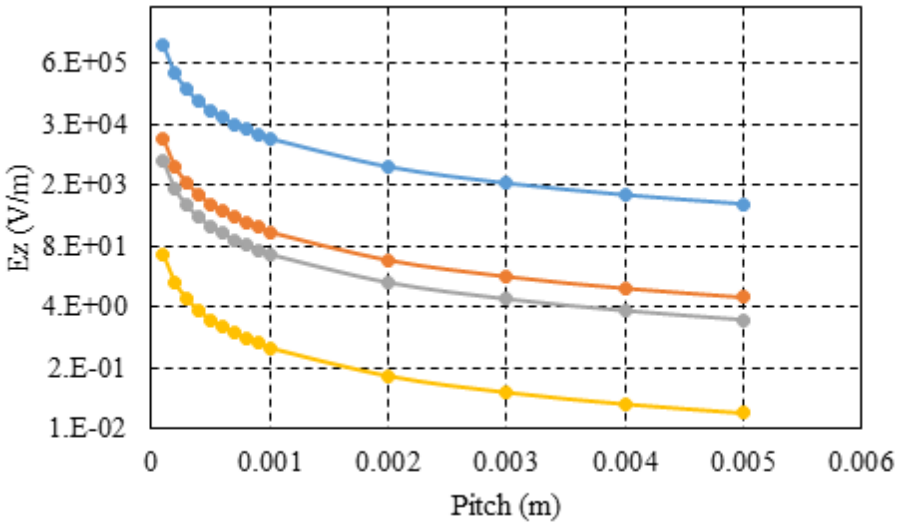

Figure 5-3 Dependence of conservative electric field component E_z on increasing pitch.

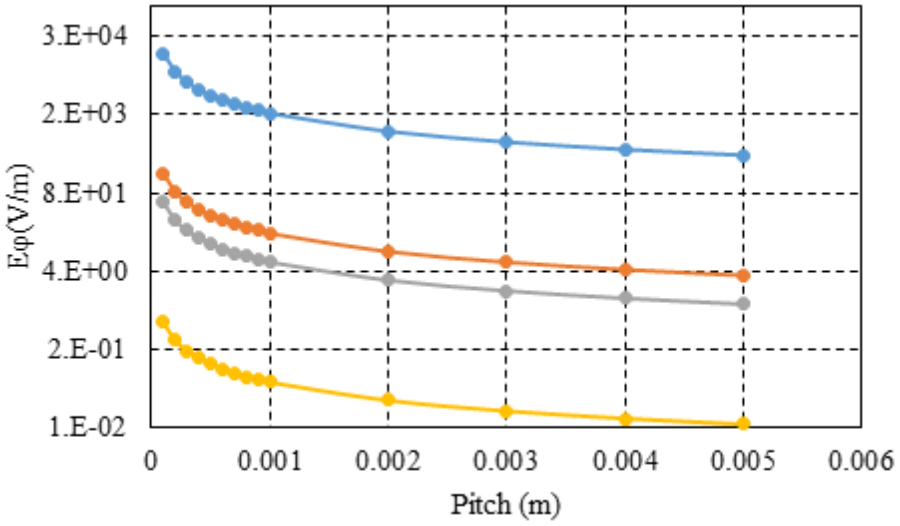

Figure 5-4 Dependence of conservative electric field component E_ϕ on increasing pitch.

From the calculations, we draw a comparison of the two electric field component, E_z and E_ϕ for the solenoid geometry specifically at 30 MHz resonant frequency. Electric field dependencies are shown as a function of increasing pitch angle in Figure 5-5.

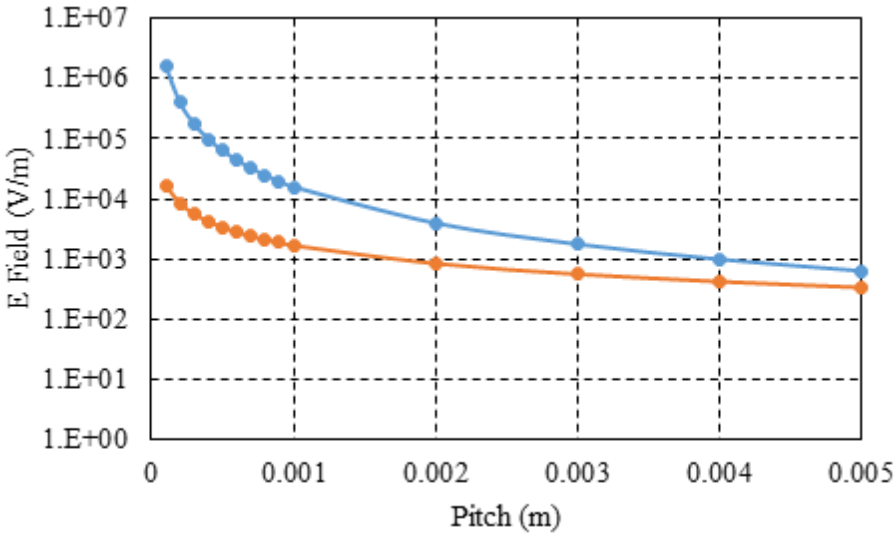

Figure 5-5 Comparison of the electric field components E_z (blue) and E_ϕ (orange) dependency on pitch variation.

The magnetic field H_z is shown as a function of the pitch for 30 MHz resonant frequency in Figure 5-6. It shows a typical decrease in magnetic field as the pitch increases, which a well observed trend in solenoids. For the given frequency, we observe the E_z (blue) component is almost an order of magnitude larger than E_ϕ (orange). The difference is more marked at lower pitch.

To understand the trends and dependencies better, we plot the electric fields as a function of increasing frequencies from 10 kHz to 1 GHz. This was calculated for five increasing pitch, 0.1 mm(blue), 0.2 mm(orange), 0.7 mm(yellow), 2 mm(green), 4 mm (dark blue) as shown in Figure 5-7, Figure 5-8. Frequency axis is in logarithmic scale and all pitch units here are in mm. We clearly observe the increase in E_z field component as the frequency increases.

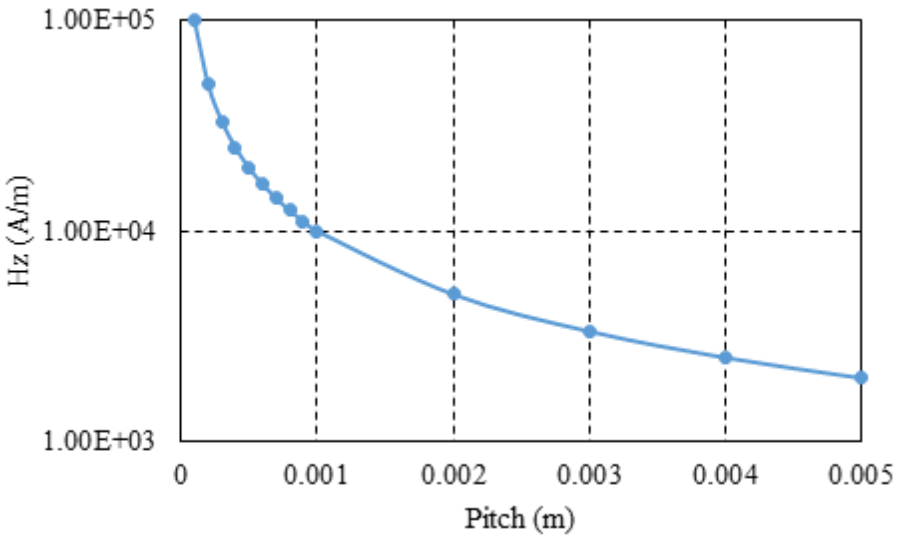

Figure 5-6 Plot showing dependency of magnetic field component H_z on pitch variation at 30 Mhz frequency.

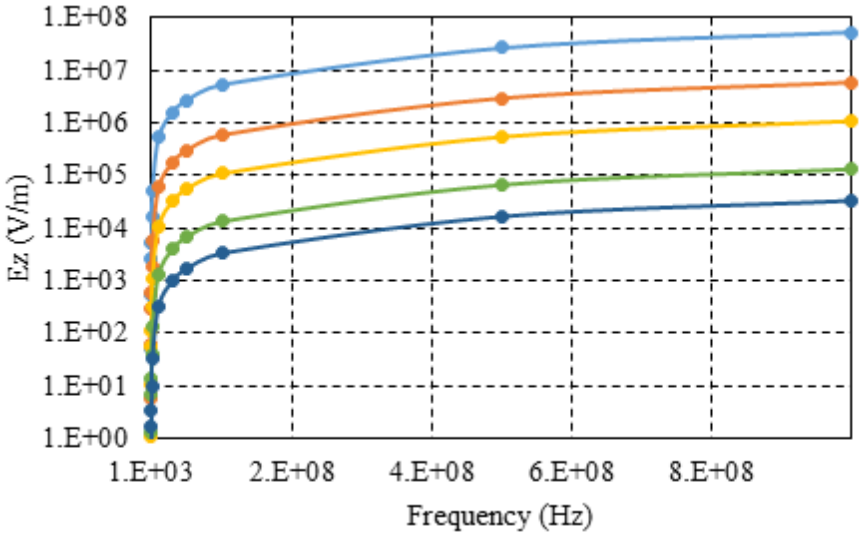

Figure 5-7 Electric field component E_z as a function of frequency variation.

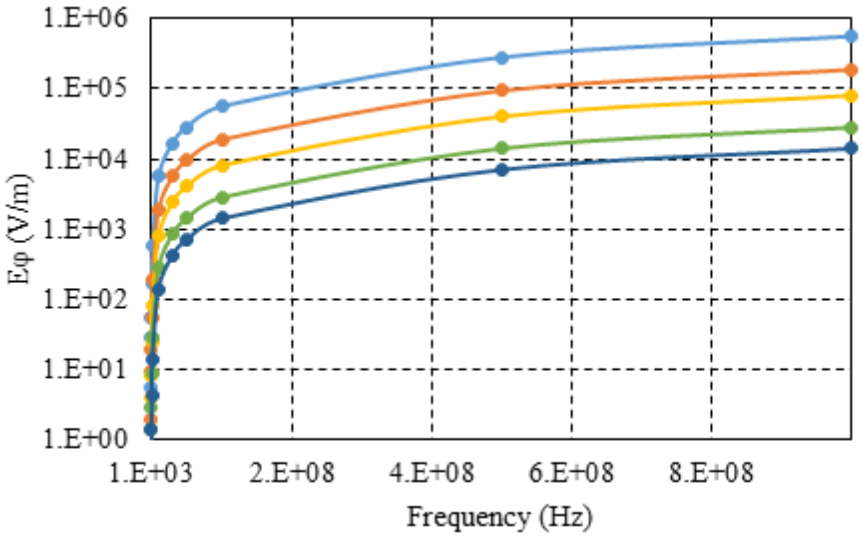

Figure 5-8 Electric field component E_ϕ as a function of frequency

It can be observed from Figure 5-9, at every given frequency point the conservative electric field E_z is an order of magnitude higher than E_ϕ. The electric field shows a linear increase to frequency. The E_z is negligible at lower frequencies, however it has a significant presence at higher frequencies in the MHz regime.

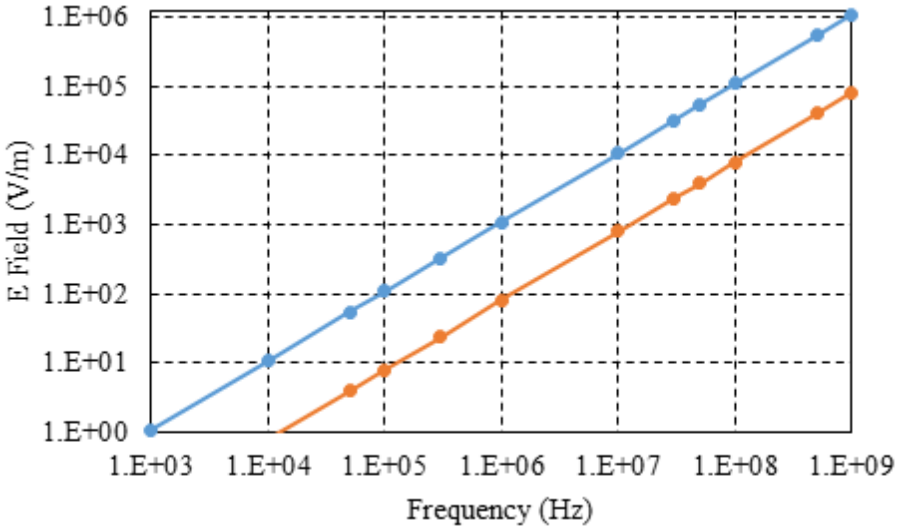

Figure 5-9 Comparison of the electric field components E_z (blue) and E_ϕ (orange) dependency on frequency variation.

5.3 EM Modeling of Field Components using Ansoft HFSS

Ansoft HFSS FEM based simulator tool described in chapter 4 was used to simulate and visualize the field components in the solenoid and capacitor [109]. The geometry design used in the simulator follows closely the experimental setup. The simulator was set up similar as in chapter 4. In addition to the LCR geometry drawn in HFSS in chapter 4, in these set of simulations we introduced a gapped copper shield between the solenoid and the sapphire. The LCR resonator was simulated using driven mode and interpolated sweep to check for resonance frequency. Next, the structure was simulated for the field distribution. We then use the HFSS field calculator to delineate the electric field components and plot them individually.

5.3.1 Visualization of E_z, E_φ, H_z Field Components in Solenoid

To be able to better visualize the various field components we plotted their vector field distributions. Vector field distribution of the electric field in the capacitor E_y, is observed from Figure 5-10a. The electric field distribution is typical to a parallel plate capacitor, with no other significant field components. Total electric field vector distribution in the solenoid shown in Figure 5-10b clearly indicates a fairly strong axial E_z component at the sample region and while presence of E_ϕ is non-significant at the sample region due to the large diameter of the coil [17].

To separate the electric field components and to study their individual effects, we removed E_z field since E_ϕ cannot be varied without affecting the *rf* source. Hence, the effect of H_z on the sample was analyzed while suppressing E_z by imposing perfect-electric-conductor (PEC) boundary condition (BC). On placing the copper shield in the solenoid, the electric fields tangential to the shield surface go to zero, i.e., $E_{\tan} = 0 \xrightarrow{PEC} E_z = 0$.

This BC forces the conservative electric field E_z which is tangential to the PEC (copper) cylinder to go to zero.

The BC was incorporated in HFSS by drawing a cylindrical copper shield with longitudinal single gap or multi gaps (to prevent eddy currents) inserted between the solenoid coil and the sapphire dielectric. This copper shield was introduced between the solenoid coil and the sapphire dielectric similar to the experiment. Figure 5-10 shows the axial cross section of solenoid with copper shield. We observe a marked difference in the electric field components between Figure 5-10b and Figure 5-10c. After the copper shield introduction in Figure 5-10b the screening of E_z can be clearly observed and we are left with only the E_ϕ field component.

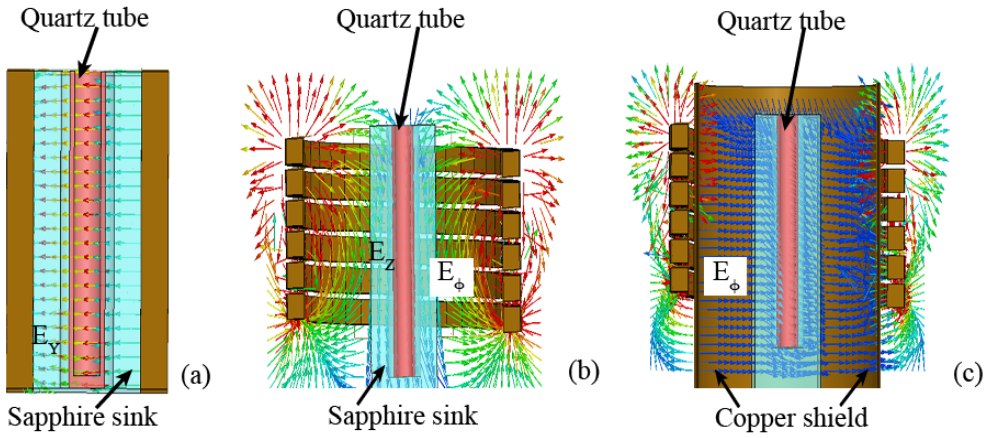

Figure 5-10 Vector Field Distribution of (a) Electric Field (E_y) in Capacitor, (b) Conservative and Circumferential Electric Field (E_z, E_ϕ) in Solenoid, and (c) Circumferential Electric Field in Solenoid with Shield (E_ϕ).

5.3.2 Verification of Axial Conservative Electric Field Component E_z

Further, to verify the presence of the E_z, we extracted all the electric and magnetic field components, E_z, E_ϕ, H_z using the HFSS field calculator. The various magnitude plots were studied to understand the E_z presence and significance in our 30 MHz LCR system.

Fields in the solenoid were simulated for samples with different permittivity and conductivity, a) empty (air) quartz tube ε_r=1, σ=0 S/m and b) quartz tube filled with saline solution ε_r=81, σ=1 S/m.

The first column in Figure 5-11 pertaining to the air sample shows the magnitude of E_z, E_ϕ, H_z, the trend of the fields show a significant presence of the conservative field E_z, very weak circumferential field E_ϕ and a moderately homogenous magnetic field distribution H_z. We observe a similar trend in the second column which contains a saline solution. However, we do observe lower E_z in the sample region which can be attributed to the high conductivity of the solution. In the third column, we utilized the air sample similar to the first column and additionally introduced the copper shield. Simulated effect of the copper shield on the E_ϕ, E_z and H_z field components in the solenoid clearly demonstrate strong suppression of the E_z with only slight reduction of E_ϕ and H_z components. Additionally, the copper shield as observed from Figure 5-11 also makes the H_z component more uniform and homogenous.

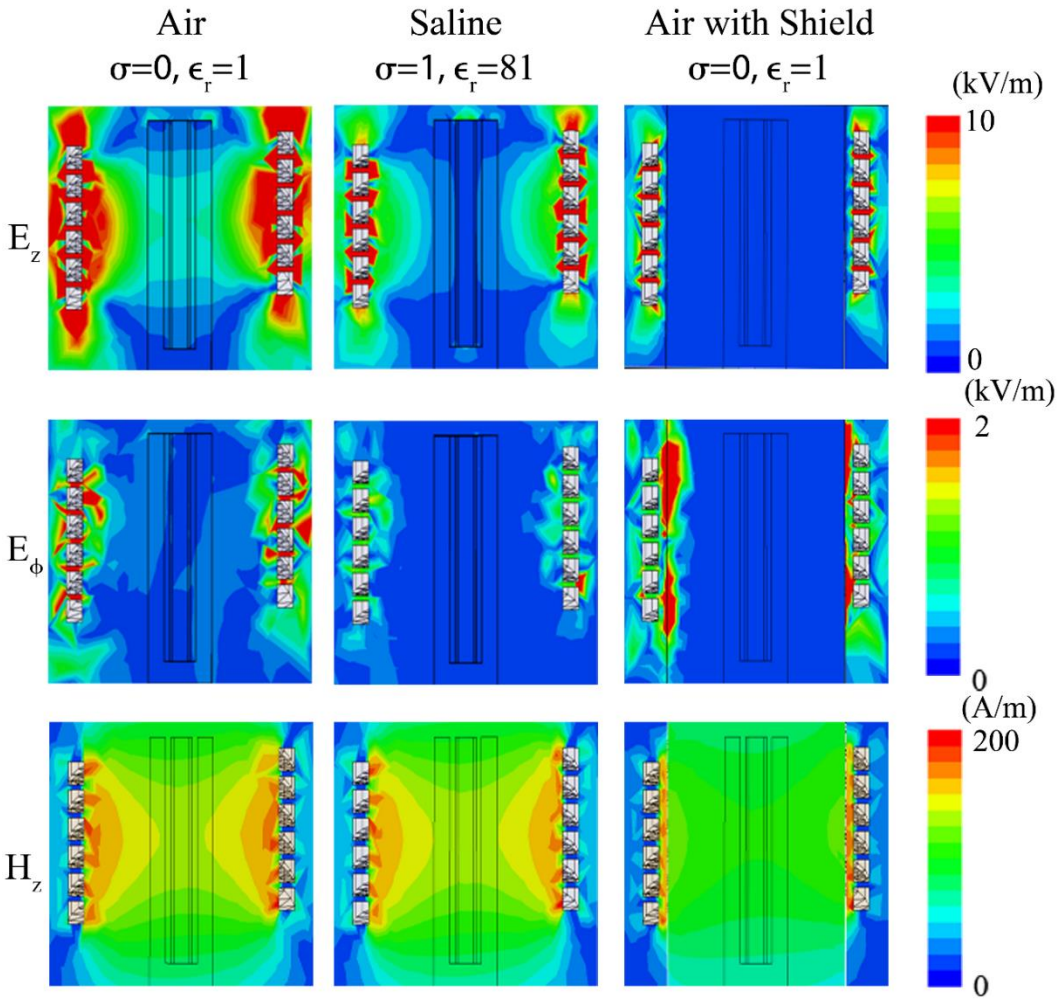

Figure 5-11 Magnitude of conservative electric field E_z, magnetically-induced electric field E_φ and magnetic field H_z are shown for solenoid with quartz tube.

5.4 Experimental SAR measurement and calculation of overestimation

We designed an experiment to determine the influence of the E_z component on the MNP sample heating and to investigate the heating losses associated with each field component. To that end, we measured the sample in three different *rf* field configurations: (i) capacitor, (ii) solenoid and (iii) solenoid with shield. In addition to the capacitor (E_y) and solenoid ($E_s=E_\phi+E_z$) measurements described in chapter 4, we also measured the heating efficiency of the samples placed inside the solenoid with a gapped copper shield

which screens out the conservative electric field E_z, and only the H_z field and its induced E_ϕ field remain. The BC was incorporated experimentally by using a copper sheet on G-10 to create the cylinder with longitudinal single gap or multi gaps (to prevent eddy currents) which was placed close to the inner edge of the solenoid. This way were are able to separate the fields and obtain heat slope versus time information of each field components interacting with the sample.

5.4.1 Calculation of SAR

Heat loss per unit volume P (W/m^3) of the sample placed in either the capacitor/solenoid/solenoid with shied can be calorimetrically expressed as

$$P = C_{ps}\rho_s q^m . \tag{5.4}$$

Here, C_{ps} is constant pressure specific heat (J/ (kgK)), ρ_s is the mass density (kg/m^3), q is the slope dT/dt. The Specific Absorption Rate, SAR (W/kg) which is the loss per unit mass of the sample can be obtained calorimetrically from Eq. (1) as P/ρ_s, $SAR_m^{sample} = \frac{P}{\rho_s} = C_{ps} q^m .$

The superscript *m* refers to the three cases of the sample being placed in either the capacitor *c*, solenoid *s0* or solenoid with shield *ss*. Electromagnetically the heat loss per unit volume of the sample P (W/m^3) can be expressed in terms of E_{rf} and H_{rf} components as

$$P = \frac{1}{2}\sigma_{sus}\left[\gamma^m(\sigma_{sol})\left|E_L^m\right|^2\right] + \pi\mu_0 f \chi^{"} \left|H\right|^2 v_f , \tag{5.5}$$

where, σ represents electric conductivity of the sample, $\gamma(\sigma)$ is the depolarization factor due to the free ion charges in the sample, v_f is the volume fraction of NPs in the suspension, E_L is the local electric field in the sample region, f is the resonant frequency, χ" is the magnetic susceptibility of the sample and H is the magnetic field in the solenoid. Local electric field in each of the configuration can be re-written as, (i) $E_L^{s0} = E_s$ in

solenoid, (ii) $E_L^{ss} = E_\phi$ in solenoid with the shield and (iii) $E_L^c = \beta E_y$ in the capacitor where $\beta = 0.11$ is the dielectric polarization screening factor. Here the power loss in the sample originates from two major components, (i) conservative electric field, E_z and, (ii) magnetic field, H_z.

5.4.2 Depolarization factor

The depolarization factor $\gamma^m(\sigma)$ for the solenoid and the solenoid with shield are $\gamma^{ss}(\sigma)\equiv 1$ and $\gamma^{ss}(\sigma)\cong 1$ respectively since the sample is oriented parallel to the fields except E_ϕ. However, E_ϕ at the center of the sample is almost zero due to the solenoid geometry [17]. For the capacitor factor since the sample is perpendicular to electric field, de-polarization factor is expressed as

$$\gamma(\sigma) = \left| \frac{1}{1 + j\left(\frac{\omega_p(\sigma)}{\omega}\right)} \right|^2 = \frac{1}{1 + \left(\frac{\omega_p(\sigma)}{\omega}\right)^2}. \tag{5.6}$$

Here, $\omega_p(\sigma)=\sigma L/\pi a\varepsilon_0\varepsilon_s$, with sample tube length L=15 mm and inner radius a=1.4 mm. $\varepsilon_0\varepsilon_s$ is the permittivity of the NP solution and ω is the resonant frequency of the resonator.

5.4.3 Measurement of NaCl for calculation of fields E_φ, E_z and E_s

As a first step, a solution of known conductivity was measured in the three *rf* configurations to calculate the individual fields in the system, E_φ, E_z and E_s. Here we used the physiological concentration of NaCl (2.5 mM) with a known conductivity of σ_{salt}=0.0314 S/m. The Temperature versus time for 2.5mM NaCl for the three configuration is shown in Figure 5-12. The depolarization factor $\gamma^m(\sigma)$ for NaCl in the capacitor was determined from Eq. 4.3 to obtain a value of γ^c=0.57. For NaCl which is non-magnetic, the

magnetic susceptibility is zero (χ”=0). Using this in Eq. 4.2 and re-arranging we obtained the expression for the local field,

$$\left|E_L^m\right|^2 = \frac{2C_{ps}\rho_s q^m}{\sigma_{sus}\gamma^c\left(\sigma_{sol}\right)}. \tag{5.7}$$

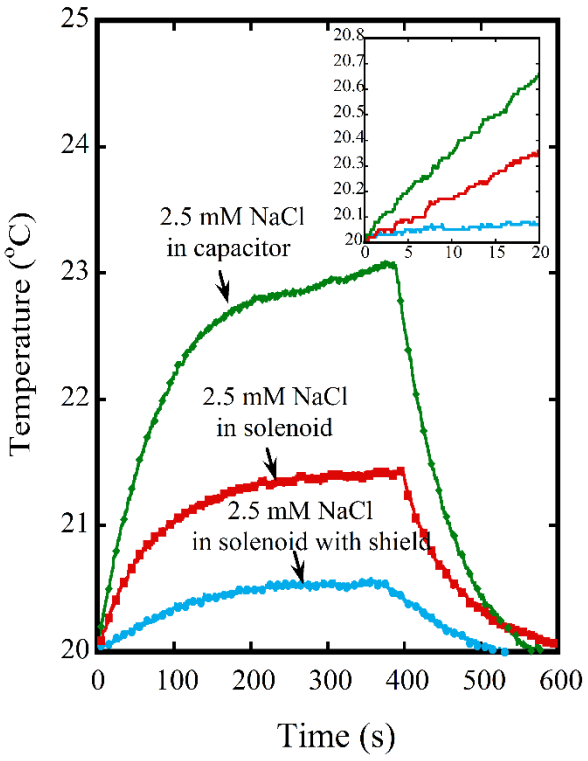

Figure 5-12 Temperature as a function of time for 2.5mM NaCl in the solenoid (blue) and capacitor (red). Inset shows temperature slope in the first 20s.

The corresponding specific heat capacity C_{ps} and density values ρ_s, conductivity σ_{salt} along with the respective de-polarization $\gamma^m(\sigma)$ and slope value q^m for each configuration were substituted in Eq. 5.7 to determine each local electric field. Local field for each of the configurations can be written as follows, (i) In capacitor $\left|E_L^c\right|^2 = \frac{2C_{ps}\rho_s q^c}{\sigma_{sus}\gamma^c\left(\sigma_{sol}\right)}$, (ii) in solenoid $\left|E_L^{s0}\right|^2 = \frac{2C_{ps}\rho_s q^{s0}}{\sigma_{sus}}$, and (iii) in solenoid with shield

$\left|E_L^{ss}\right|^2 = \frac{2C_{ps}\rho_s q^{ss}}{\sigma_{sus}}$. Heat slope from the measurements and the calculated corresponding local field are recorded in Table 5-1.

Table 5-1 Slope (q=dT/dt) values of NaCl and calculated local fields values for the three configurations.

Configuration	Slope q_{salt}	Local electric field E_L (kV/m)	H_z (kA/m)
Capacitor 'c'	0.02557	3.46 (βE_φ)	0
Solenoid 's0'	0.01408	1.936 (E_s)	8.2
Solenoid with shield 'ss'	0.00227	0.776 (E_φ)	7.1

From the calculat local electric field in capacitance ($E_L^c = \beta E_y$) the field across the capacitor E_y was determined to be 31.4 kV/m. The conservative electric field component and the magnetic field were estimated to be 1.77 kV/m and 7.1 kA/m.

5.4.4 Measurement of SPIO NPs

The SPIO NPs samples of two concentrations, 28 mg/ml and 1mg/ml measured in Chapter 3 are again utilized in this chapter. Here, each of the SPIO NPs was measured in the capacitor, solenoid and solenoid with shield. The two concentrations of SPIO NPs 28 mg/mL and 1 mg/mL studied here have volume fractions $\nu_{f1}=5.4\text{x}10^{-3}$ and $\nu_{f2}=1.96\text{x}10^{-4}$ respectively. Temperature versus time of the two SPIO NPs, along with their slope are shown in Figure 5-13. For 28 mg/ml SPIO NPs we observed a distinct drop in sample heating when the copper shield was introduced. Similar trend can be observed for the SPIO NP of lower concentration 1mg/ml as well. This reduction can be better observed from the

slope values of the SPIO NPs. Heat (T vs t) slopes for first 20s of the two SPIO NPs placed in three different configurations are summarized in Table 5-2.

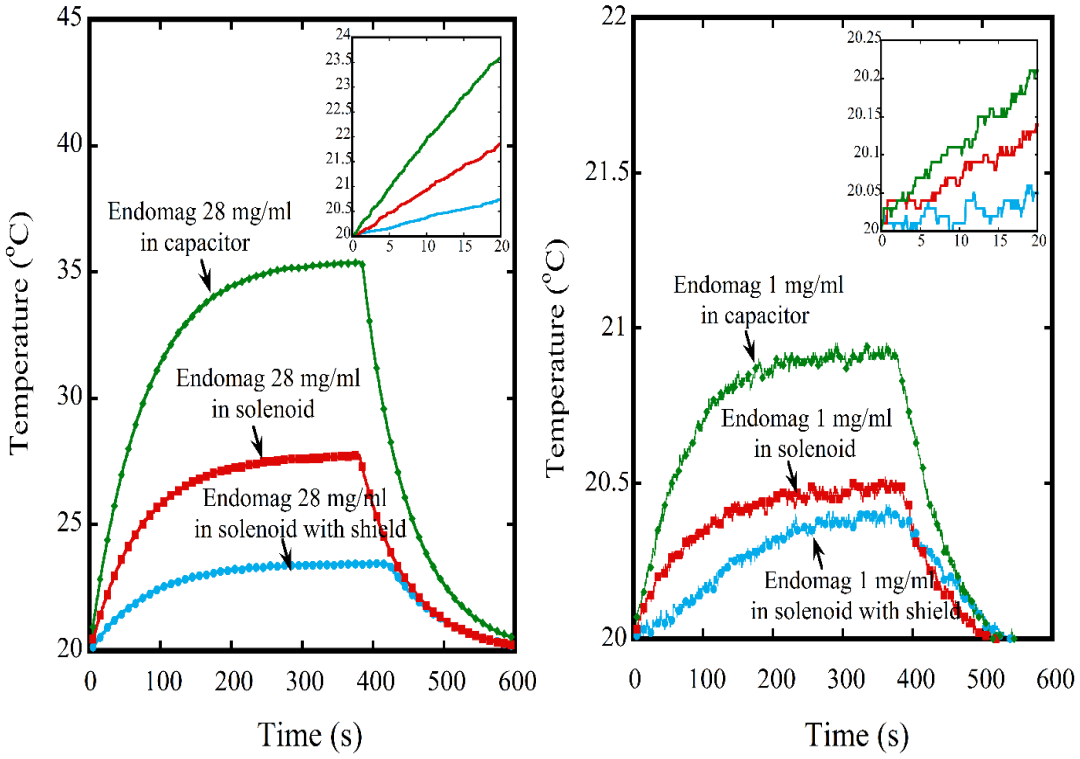

Figure 5-13 Temperature as a function of time for 28 mg/ml and 1 mg/ml Endomag in the solenoid (blue) and capacitor (red). Inset shows temperature slope in the first 20 s.

Table 5-2 Slope values (q=dT/dt) of SPIO for the three configurations.

Configuration	**Slope q^m_{spio} (28 mg/mL)**	**Slope q^m_{spio} 1 mg/mL**
Capacitor "c"	0.1832	0.009255
Solenoid "s0"	0.093635	0.005501
Solenoid with shield"ss"	0.0364	0.001868

5.4.5 Extraction of magnetic susceptibility from measurements

Since there is no magnetic loss involved in the capacitor ($H_{rf} = 0$) in Eq. 4.2 and substituting capacitor slope q^c for the two SPIO NPs samples we calculated the conductivity of the NPs suspensions as σ_{sus1}=0.13 S/m and σ_{sus2}=0.0038 S/m. Effective conductivity of a colloidal suspension that contain a specific volume fraction of NPs, ν_{f1} can be written as a combination of the conductivity of the NPs and solution,

$$\sigma_{sus} = \sigma_{NP}\nu_f + \sigma_{sol}(1-\nu_f). \tag{5.8}$$

Two volume fractions give rise to a set of simultaneous equations, solving which we obtained the equation to determine the conductivity of the NP and solution,

$$\sigma_{NP} = \frac{\sigma_{sus1}(1-vf_2) - \sigma_{sus2}(1-vf_1)}{vf_1 - vf_2} \text{ and} \tag{5.9}$$

$$\sigma_{sol} = \frac{\sigma_{sus2}vf_1 - \sigma_{sus1}vf_2}{vf_1 - vf_2}. \tag{5.10}$$

Substituting the volume fractions ν_{f1} and ν_{f2} and the calculated effective conductivities σ_{sus1} and σ_{sus2} of the two samples in Eq. 5.9 and Eq. 5.10 the conductivity of SPIO-dextran NP, σ_{NP} and conductivity of the dispersion medium, σ_{sol} were estimated as σ_{NP}=23.16 S/m and σ_{sol}=0.002 S/m respectively.

In order to determine the magnetic loss of the SPIO NPs, the calorimetric equations for the sample in solenoid with shield was developed from Eq. 5.5,

$$2C_{ps}\rho_s q_{sus}^{ss} = \sigma_{sus}\left|E_\phi\right|^2 + 2\pi\mu_0 f \chi''\left|H_z\right|^2 \nu_f, \tag{5.11}$$

from which susceptibility was extracted as

$$\chi'' = \left(\frac{2C_{ps}\rho_s q_{sus}^{ss} - \sigma_{sus}\left|E_\phi\right|^2}{2\pi\mu_0 f \left|H_z\right|^2 \nu_f}\right). \tag{5.12}$$

Substituting fields and slopes from Table 5-1 and 5-2 we obtained $\chi"_1$=0.0038 for 28 mg/mL SPIO, and $\chi"_2$=0.0055 for 1 mg/mL SPIO NPs suspensions. The SAR of the NPs in the capacitor and solenoid is expressed as SAR_E and SAR_M respectively,

$$SAR_E^{sample} = \frac{\sigma_{sample}}{2\rho_{NP}} \left|E_L\right|^2 . \tag{5.13}$$

From the mass density of SPIO ρ_{NP}=5.17x10^3 kg/m^3 and that of the solution $\rho_{sol}=\rho_{water}$=10^3 kg/m^3, we calculated SAR of the NPs and solution for electric field βE_y=3.46 kV/m in the capacitor as 27 kW/kg and 2 W/kg, respectively. The magnetic SAR of the SPIO NPs is expressed as

$$SAR_M = \frac{\pi\mu_0\chi"}{\rho_{NP}} f \left|H_z\right|^2 . \tag{5.14}$$

The magnetic SAR of the SPIO NPs was calculated by substituting the susceptibilities of the two concentration in Eq. 5.14. Table 5-3 gives the susceptibility, magnetic loss SAR and the normalize SAR of the SPIO NPs calculated for in the solenoid with shield i.e., no E_z component.

Table 5-3 SAR values for respective SPIO concentrations.

Concentration (mg/mL)	**$\chi"$**	**SAR_M (W/kg)**	**SAR_M/fH^2 (Wsm^2/kgA^2)**
28	0.0038	4.1x10^3	2.9 x 10^{-12}
1	0.0054	5.86x10^3	4.16 x 10^{-12}

Magnetic and non-magnetic NPs power loss is proportional to $fH^2\chi"(f)$ and $\sigma(f)E^2$, respectively. Since $\chi"$ and σ has no frequency dependence in the frequency range 10^5-10^6

Hz, normalizations are done with fH^2 and E^2 factors for magnetic and electric SARs, respectively.

5.4.6 Overestimation of SAR when neglecting to Conservative Electric Field E_z

Current approaches of magnetic SAR calculation in literature ignore the presence and effect of any electric field component in the solenoid. In this case, the power loss from Eq. 5.5 neglecting any electric field in the solenoid can be written as

$$P = C_{ps}\rho_s q = \frac{1}{2}\left(2\pi\mu_o f \chi^{"} |H_z|^2 v_f\right). \tag{5.15}$$

Similar to Eq. 5.12 susceptibility was extracted as

$$\chi'' = \left(\frac{2C_{ps}\rho_s q_{sus}^{s0}}{2\pi\mu_0 f |H_z|^2 v_f}\right). \tag{5.16}$$

Susceptibility in this traditional approach was calculated from the slope of the NPs in the solenoid (without shield), q^{s0} which includes the effect of total electric field $E_s=E_\phi+E_z$ and the magnetic field H_z. Thus, the eddy current loss of the solution stemming from E_ϕ and the EDL loss due to E_z interacting with NP/Dextran/solution interface is wrongly attributed to magnetic heating loss, H_z. From our calculations we estimated that if the E_s electric field loss is miscalculated as magnetic loss (as typically done in literature) the magnetic SAR_M was calculated with 250% error i.e., 14 kW/kg instead 4-5 kW/kg. The origin of this EDL loss can be explained the NP-dextran-solution interface loss [123]. Since NPs are charged, counter-ion double layers are formed around the particles acting as additional source of E_{rf} induced loss. Protein bio-conjugation of the NPs further contributes to the EDL. Surface polarization of the NPs due to E_{rf} will enhance this interaction accounting for heat loss leading to such SAR value. The elucidation of the mechanisms of

NPs heating in electric/magnetic fields is very important for designing therapeutic systems for targeted hyperthermia.

In this chapter, the solenoid as a part of the LCR resonant system was developed to study the three field components present, (i) axial conservative electric field E_z, (ii) circumferential electric field E_ϕ, and (iii) axial magnetic field H_z. Using EM simulations and experiments the fields in the resonator specifically the solenoid were analyzed in detail to understand better the presence and significance of the conservative electric field E_z. The conservative electric field component E_z interacts with the EDL i.e., the NP/bio-conjugate/solution interface thus contributing significantly to the heating of the MNP in the solenoid. As observed experimentally and via simulation, the EDL/E_z interaction heating has a multi-fold dependency on the (i) solenoid geometry, (ii) resonant frequency, (iii) input power, (iv) NPs surface charge, (v) protein conjugate and (vi) counter-ions. Consequentially, when in literature the conservative electric field is neglected, the EDL/E_z interaction heating is misinterpreted as magnetic loss leading to an overestimation of magnetic SAR. In our experiments, the EDL/E_z interaction heating contributing to the SAR overestimation for the SPIONs are 250%. Thus understanding the exact origin of each loss component and its contribution to SAR is of vital importance to accurately characterize the heating efficiency of MNPs for their use in clinical trials.

Chapter 6 Thermal Trigger of Magnetic Nanoparticles using Low Frequency Magnetic Fields

In the previous chapter, we studied via simulation and experiments the presence of three different fields (E_ϕ, E_z and H_z) in the *rf* hyperthermia applicator for magnetic nanoparticles. The interaction mechanisms and the respective field component contribution to the SAR of the SPIO NPs were discussed. In this chapter, based on the conclusion from chapter 4 and 5 we focused on building a low frequency resonator for the purpose of generating H_{rf} magnetic fields. Our final goal was to develop a low frequency magnetic field applicator for hyperthermia or thermal trigger of nanoparticles.

6.1 Introduction

One of the crucial aspects of designing a hyperthermia applicator using nanoparticles as heat-enhancers is targeting and maintaining selectivity of the tumor site. To this end, the design focus was to minimize heat deposition on healthy tissue. The presence of the electric field in the solenoid, both conservative E_z and circumferential E_ϕ as observed in chapter 5 contributed to the non-magnetic heat loss i.e., non-specific heating [123, 124]. Based on our studies in the previous chapter, to remove any such extraneous heating components we needed to have a pure magnetic field generator. Another disadvantage of NPs based hyperthermia is the concentration of NPs required to achieve significant level of temperature increase at the tumor site [121, 125, 126]. Figure 6-1 shows the SAR required to achieve 15 K temperature increase as a function of tumor size for intra-tumoral concentration of 10mg/cm^3 magnetic NPs [127]. Due to difficulties in achieving such high NPs concentration at the tumor site, it is much interest to explore alternate NPs based cancer therapies to hyperthermia. Researchers have been studying the temperature

gated ion channels and triggering them through nanoparticles to overcome the problem of achieving the desired SAR for thermal ablation/hyperthermia [20].

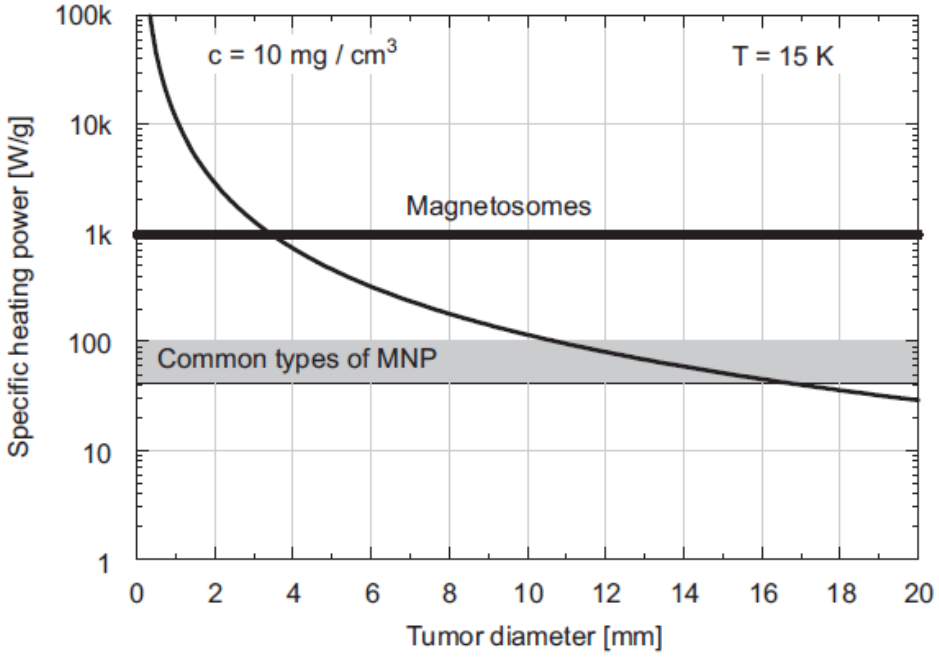

Figure 6-1 SAR/SLP requirement as a function of tumor size to achieve a temperature increase of 15K for magnetic nanoparticles.

Different temperature sensitive ion channels are presented in Figure 6-2 [128-131]. Opening and closing i.e., gating of these ion channels are temperature sensitive, for example gating of TRVP1 occurs at $T > 43^{\circ}C$. To achieve such gating which in turn causes tumor apoptosis, we would require focused magnetic field application on the MNPs and minimum heat deposition on surrounding tissue. We developed a resonant system using MNPs that has a twofold ability to be used as a hyperthermia applicator and can thermally trigger changes in ion channels. In this chapter, we discuss the design of the low frequency Inductance Capacitance Resistance (LCR) resonator which was used to generate a high magnetic field in a variable frequency range of 100 kHz to 1 MHz. A lower frequency

range was chosen since the conductive behavior of tissue is dominant at higher frequencies (MHz) which in-turn has a major influence on non-specific heating.

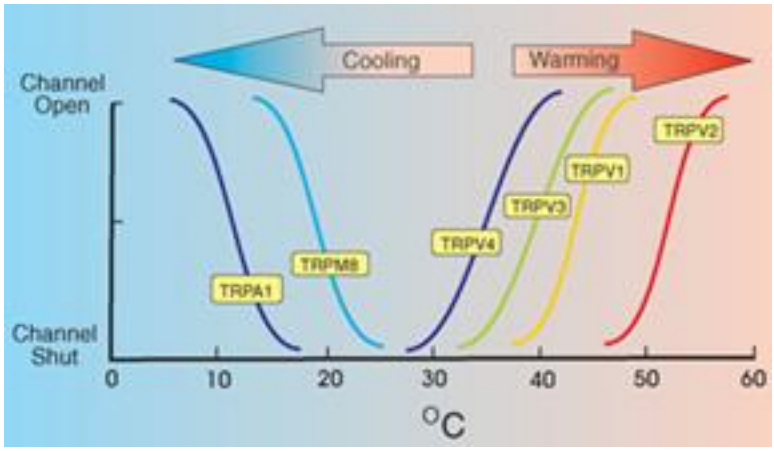

Figure 6-2 Temperature gated ion-channels.

6.2 Design of LF Magnetic Field Generator

Resonant circuit principle was utilized to design and build the low frequency magnetic field generator to produce maximum magnetic field [132]. A ferrite core solenoid was used to build the inductor. Here, the magnetic flux is concentrated in the ferrite core due to the permeability difference between the ferrite core and air medium. In case of an air gap in the ferrite core, the magnetic field is focused in the air gap due to very less dissipation of flux. The design idea was to place the sample to be investigated in an air gap in such a way to remove the presence of any electric field components that originate in a solenoid structure i.e., conservative electric field (E_z) and eddy currents (E_φ) [123, 124].

6.2.1 Ferrite core inductor

We first constructed the inductor i.e., ferrite core solenoid. The inductor was constructed from two U-cores (U 101/76/30, material N27) purchased from EPCOS. A ferrite piece of the same material was introduced between the two U-cores. This created an air gap on the other arm of the ferrite core as shown in Figure 6-3. Also shown are the

magnetic flux lines in the core and the air gap. The solenoid was constructed by winding 30 turns of 18 AWG magnetic insulated copper wire on a spool fitted into the lower arm of the UU Ferrite. A copper shield surrounds the winding to screen out any stray electric field from affecting the magnetic field in the air gap/sample region. Electrical insulation between the shield and coil was achieved by using an electrically insulating, thermally conductive paste which serves to dissipate heat as well. Entire lower arm of the ferrite was cooled through a fan, focusing specifically on the coil windings. The sample was placed in a 3D printed cooling cell of 10 mm thickness which was designed to hold a cylindrical quartz tube 3 mm outer diameter. The cooling cell shown in Figure 6-3placed in the air gap was maintained at a constant temperature of 20.5°C using a refrigerated bath circulator (Thermo Scientific). The ferrite core primarily guides the magnetic flux ensuring maximum field in the air gap/sample region. This design as shown in Figure 6-3, ensures that the sample holder is in a pure magnetic field with uniform distribution in the air gap/sample region.

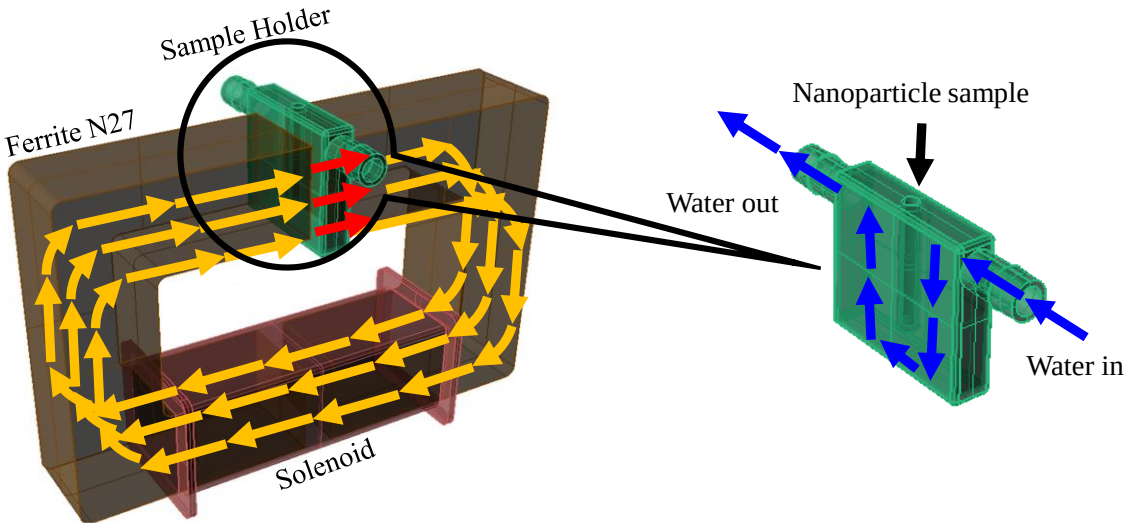

Figure 6-3 Geometry of ferrite core inductor with sample holder.

6.2.2 Capacitive tuning and matching

The LCR resonator is capacitively coupled to the *rf* power generator/amplifier. Capacitive coupling was chosen over inductive coupling to increase the operating frequency range of the resonator for a given inductance. Critical coupling i.e., impedance patch of 50+0j was achieved throughout the frequency range through the matching and tuning capacitors. Resonance was achieved through a parallel tuning and series matching capacitor connected to the ferrite core inductor as shown in Figure 6-4.

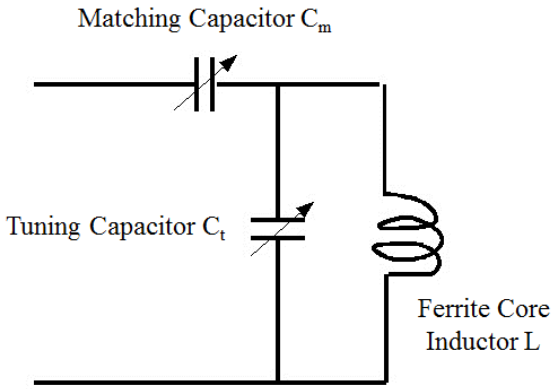

Figure 6-4 Ferrite core inductor with tuning and matching circuit.

Here we used a low frequency *rf* generator (T & C Power Conversion, Inc.) which produces a maximum of 300 W in the frequency range of 20 kHz to 40 MHz. Air gapped capacitors tunable in the range of 40-250 pf were used as the tuning and matching capacitors in the circuit because of their low loss (high Q-factor). Such configuration allowed for impedance matching that can be observed when the circuit connected to a vector network analyzer. Q-factor, coupling and the resonant frequency data are collected from the network analyzer using a lab view program. Once the circuit is matched, it was connected to the *rf* generator to observe the input, reflected and load power. A block

diagram representation of the ferrite core LCR resonator's circuit and the connection schematics are shown in Figure 6-5.

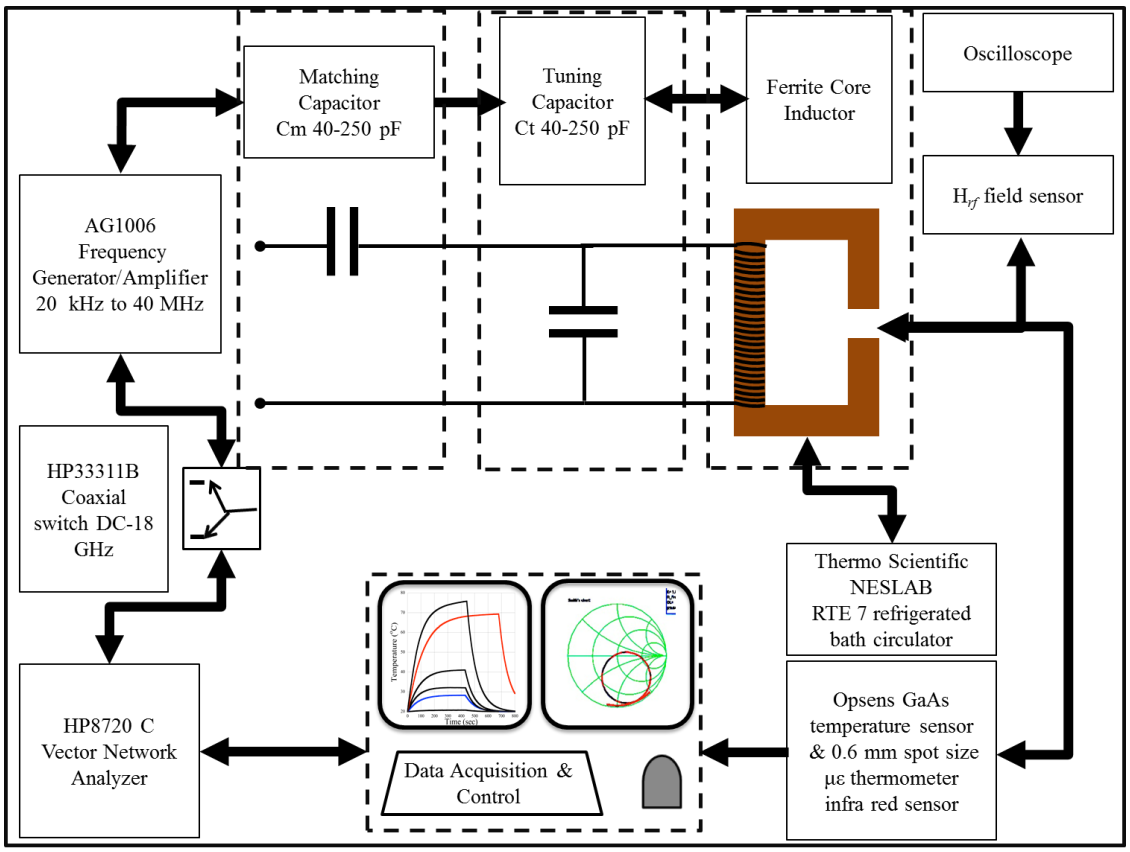

Figure 6-5 Low frequency heating measurement system with ferrite core based LCR resonator.

The magnetic field in sample holder was measured using a "sniffing loop" connected to an oscilloscope. The voltage readout was converted to the magnetic field similar to as described in chapter 3. To ensure stray fields from the coil winding do not affect the measurement a grounded copper shield was built around the solenoid. The sample was placed in a quartz tube housed inside the sample holder. Sample temperature was measured by a GaAs sensor (OPSENS) inserted in the middle of the quartz tube and is recorded versus time during the onset of the input power. Figure 6-6 shows the realization of the experimental low frequency ferrite core LCR resonator.

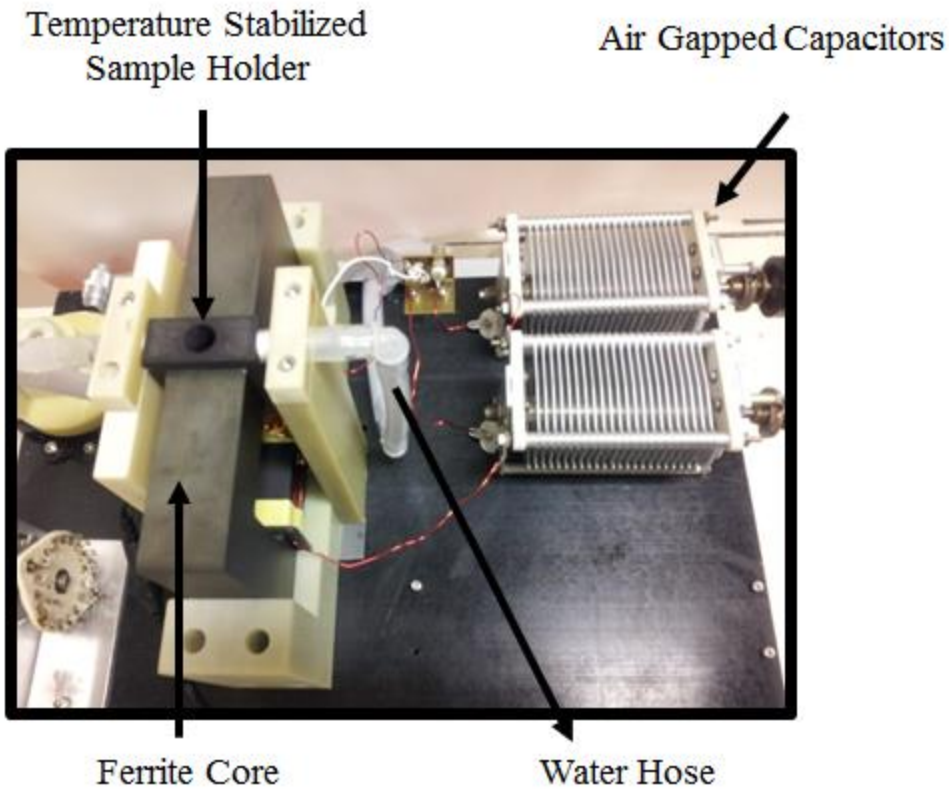

Figure 6-6 Realization of low frequency heating measurement system with ferrite core based LCR resonator.

6.3 System characterization, effect of gap and frequency on magnetic field

The system characterization for a frequency range of ~300 kHz to 500 kHz was done with 30 turns of 18 AWG magnetic insulated copper wire. Measured inductance of air core and ferrite core with different gap sizes are shown in Figure 6-7. The effect of decreased inductance as the air gap increases is crucial in designing the tuning, matching capacitors and determining the operable frequency range of the resonator. The maximum achievable field in the air gap of the ferrite resonator would depend on the air gap designed to hold the sample. Ideally the smallest gap in a closed loop ferrite core generates the maximum magnetic field due the concentration of

divergent flux lines in the air gap while larger air gaps have higher fringing dissipative fields and hence lower field.

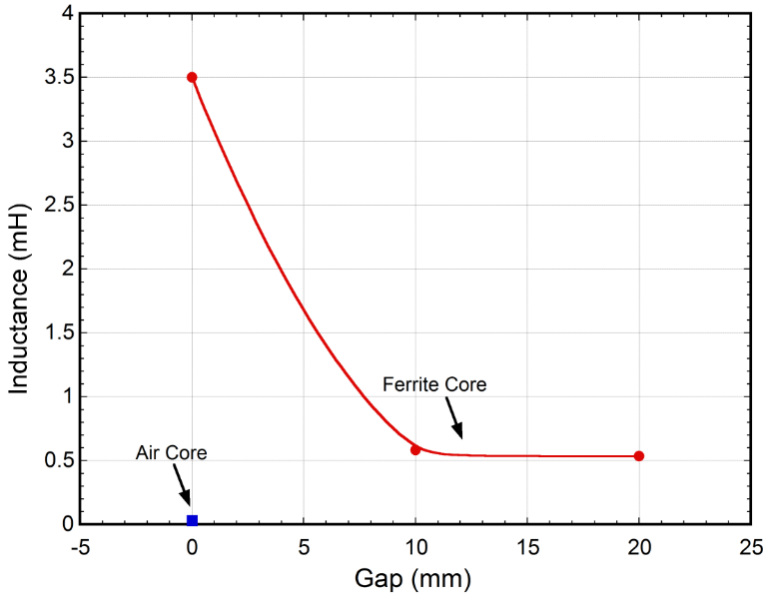

Figure 6-7 Inductance as a function of gap in the EPCOS N27 UU ferrite core. Air core inductance is shown for comparison.

The measured inductance values for the 10 mm gapped ferrite core were 29.76 μH and 585 μH for an air-core and N27 ferrite core respectively. The effective relative permeability of 10 mm gapped UU ferrite core can then be calculated from measured inductance as

$$L\_aircore = \frac{\mu_0 A N^2}{l}, \tag{6.1}$$

$$L\_ferrite10 = \frac{\mu_0 \mu_{reff} A N^2}{l}, \text{ and} \tag{6.2}$$

$$\mu_{reff} = \frac{L\_ferrite10}{L\_aircore} = \frac{585\mu H}{29.7\mu H} = 19.6. \tag{6.3}$$

Here, an air gap of 10 mm was chosen as the minimum size to accommodate the sample cooling cell which was designed to remove external systemic heating by flow of water maintained at 20.5°C. The magnetic field in the air gap was measured for increasing input

power at three different frequencies 300 kHz, 400 kHz and 500 kHz as shown in Figure 6-8. We go up to a maximum of 80 W input power at each frequency. Resonance was achieved by fixing the desired frequency in the *rf* input generator and varying the tuning and matching capacitor for the highest voltage read-out in the oscilloscope and the least measured reflected power.

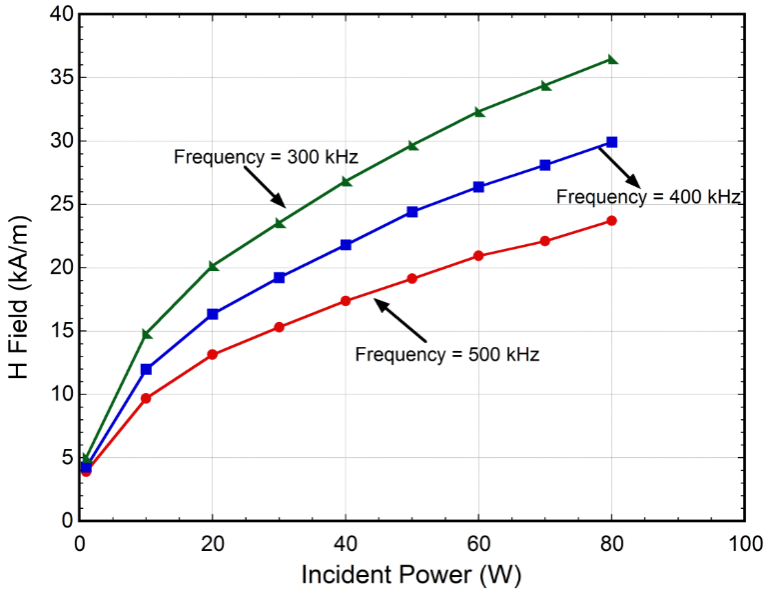

Figure 6-8 Magnetic field (A/m) as a function of incident power (W) for three different frequencies 300 kHz, 400 kHz and 500 kHz.

It can be observed from Figure 6-8 that magnetic field decreases as the frequency of operation increases. This decrease is primarily due to the ferrite material property since, ferrite core loss depends on frequency. Figure 6-9a shows the increase in core loss as the operation frequency increases. The quality factor of a resonator plays a crucial role in determining the amount of stored energy during resonance and inadvertently the maximum achievable field [2]. Hence we measured the Q-factor of the resonator to obtain a direct proof of performance degradation due to frequency dependent core loss. The decrease in Q-factor as the frequency increases can be observed for the sample space with and with

cooling. Water circulation around the sample region decreases the Q-factor due to the permittivity change/dielectric loss factor.

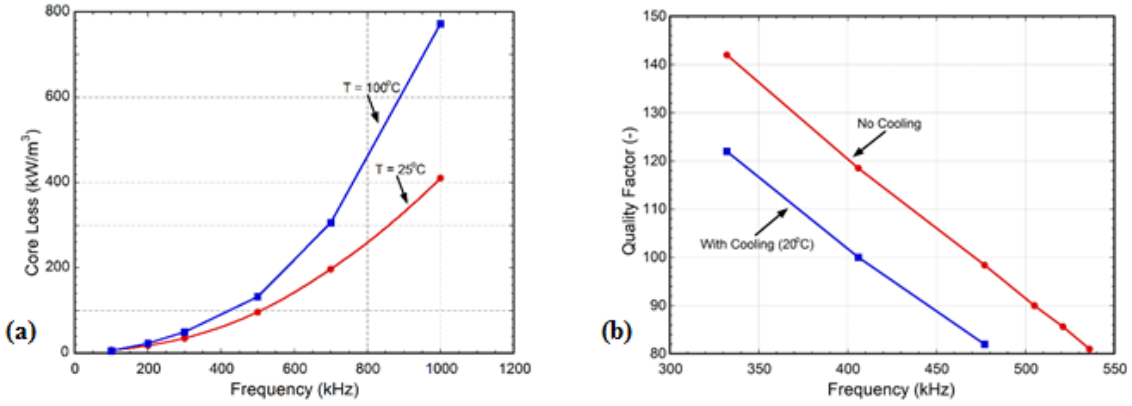

Figure 6-9 EPCOS N27 UU ferrite core (a) Core loss *vs* frequency (b) Quality factor *vs* frequency for with and without cooling.

At each of the frequencies the vector network analyzer data was extracted and plotted to observe the critical coupling. Figure 6-10 shows the reflection plot and smith chart showing critical coupling for the three given frequencies of 500 kHz, 400 kHz and 300 kHz.

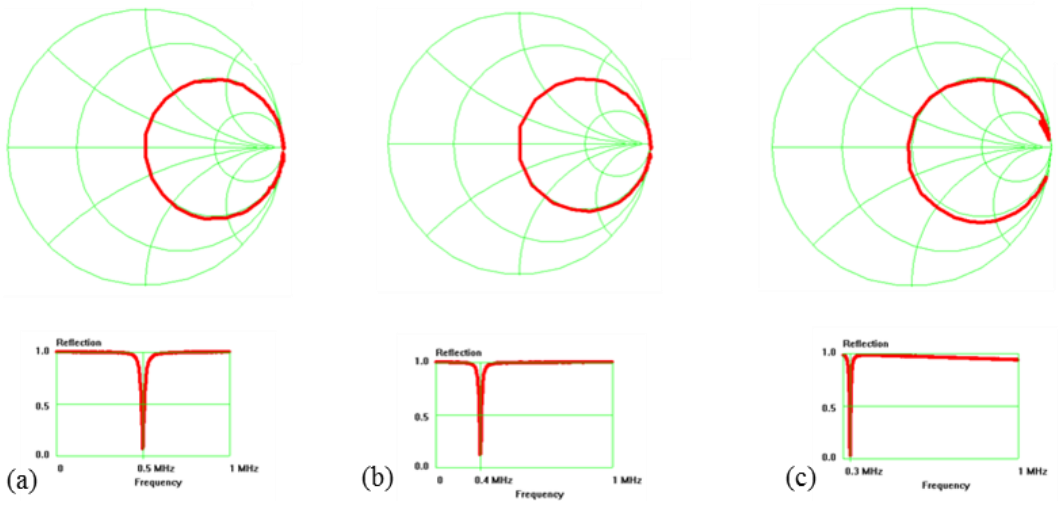

Figure 6-10 Network analyzer critical coupling shown at (a) 500 kHz (b) 400 kHz and (c) 300 kHz achieved through the tuning and matching capacitor.

6.3.1 Circuit Theory Approach to Calculate Tuning and Matching Capacitance

As a next step, we analytically obtained the values of the tuning and matching capacitor so that the LCR circuit is impedance matched to the connected to the 50 Ω load *rf* generator. Solving the LCR circuit shown in Figure 6-1 for a 50 Ω impedance match and forcing the imaginary part of impedance to go to zero we obtained the equation for the tuning and matching capacitor as

$$C_t = \frac{Q - A}{B} \text{ and} \tag{6.4}$$

$$C_m = \frac{1}{\omega Z_0 A}, \tag{6.5}$$

where, Q is the Q-factor, L is inductance, r is circuit resistance, Z_0 is the 50 Ω impedance and ω is the angular frequency. The Q-factor, constants B and A can be written as

$$Q = \frac{\omega L}{r}, \tag{6.6}$$

$$B = r(1 + Q^2), \text{ and} \tag{6.7}$$

$$A = \sqrt{\frac{B}{Z_0} - 1}. \tag{6.8}$$

From the measured inductance value of the ferrite core solenoid and the Q-factor at the given frequency, we used Eq. 6.6 to get the circuit resistance ‘r’. ‘B’ was derived by substituting Q-factor value and resistance ‘r’ in Eq. 6.7. ‘A’ was obtained from the known vale of Z_0=50Ω and the calculated ‘B’ value. Once the values of ‘r’, ‘B’ and ‘A’ were calculated for the given frequency using Eq. 6.4 and Eq. 6.5 tuning and matching capacitance value were determined. Table 6-1 summarizes the tuning and matching capacitor values for the desired frequency and the corresponding measured unloaded quality factor and inductance.

Table 6-1 Matching and tuning capacitor values (C_m, C_t) for the three frequencies.

f_r (kHz)	Q- Factor	Resistance (r)	B	A	C_m (F)	C_t (F)
316	122	9.52	141713.7	53.22	1.89E-10	2.44E-10
400	100.00	14.70	147041.24	54.22	1.46E-10	1.23E-10
500	82.00	22.41	150724.61	54.89	1.15E-10	5.72E-11

6.3.2 Verification of Measured Magnetic Field using PSPICE Circuit Model

We performed PSPICE simulations to validate the magnetic field obtained experimentally from the LCR circuit. As a proof concept, the calculations were done for one frequency and can be extended to any resonant frequency. For a resonant frequency of 316 kHz we built the PSPICE circuit from the calculated value of Cm, Ct and the measured value of L as shown in Figure 6-11. Power input to the PSIPCE circuit was supplied in the form of voltage considering an input power supply with source resistance of 50 Ω, which can be written as

$$V_{in} = \sqrt{P_{in} R}\,, \tag{6.9}$$

where, V_{in} is the input voltage, P_{in} is the input power, R is the circuit resistance. At every power level the circuit was simulated to record the voltage across the two capacitors, V_{cm} V_{ct} and the current across the inductor, I_L. The magnetic flux density can be calculated in Tesla from the current through the inductor $I_{L,}$ the number of turns per length N/L and the relative permeability of the gapped UU ferrite core as

$$B = \mu_0 \mu_{reff} I_L \frac{N}{L}\,. \tag{6.10}$$

The capacitor voltage measurements give very useful insight into how close we are to the breakdown voltage of the air gapped capacitors. We make sure to operate below the

breakdown voltage to avoid any sparking across the air gapped capacitor plates. The experimental magnetic field was measured for a power up to 80 W due to the limiting voltage of 4500V on the C_m and C_t capacitors.

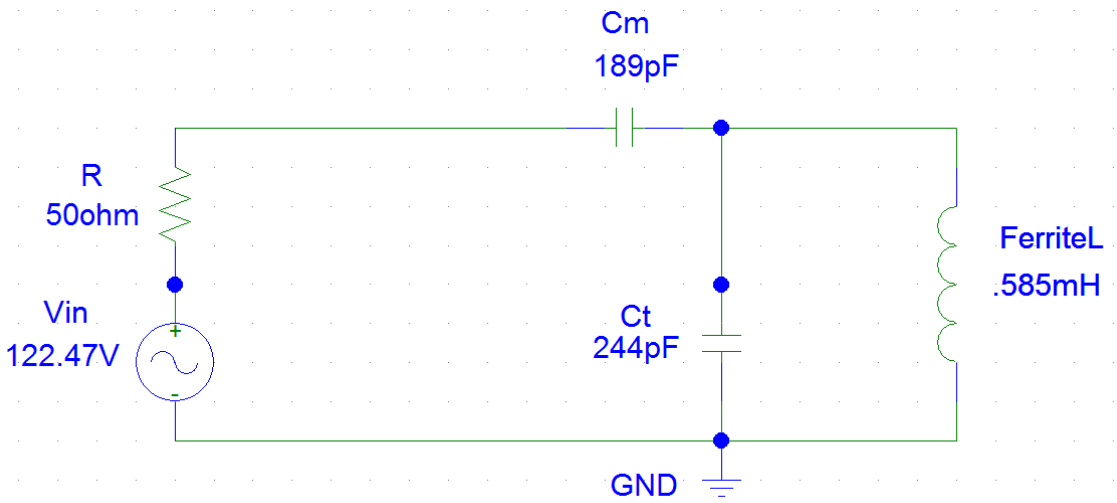

Figure 6-11 PSPICE model circuit equivalent of the experimental setup for a resonant frequency of 316 kHz and input power of 300W.

The calculated voltages at the tuning and matching capacitors, the current in the inductor and the magnetic field are summarized in the Table 6-2 for a range of increasing input power. Figure 6-12 shows the comparison of the experimental data overlaid with the calculated PSPICE magnetic field data as a function of input power. In the PSPICE calculation the input power was extrapolated to 300 W to show the magnetic field trend. Experimentally, if the ferrite core is cooled along with the sample input power of 300 W and consequentially magnetic field of H = 70 kA/m can be achieved. Higher input power can also be reached by utilized a ferrite core with less core loss at the frequency of interest.

Table 6-2 Matching and tuning capacitor values (C_m, C_t) for the three frequencies.

P_{in} (W)	V_{in} (V)	*fr* (kHz)	V_{Ct} (V)	V_{Cm} (V)	I_L (A)	B Field (mT)	H Field (A/m)
1	7.07	317	325	322	0.280	5.17	4137.85
50	50	317	2300	2270	1.98	36.52	29216.20
100	70.7	317	3250	3220	2.79	51.53	41230.76
200	100	317	4600	4550	3.95	72.96	58373.30
300	122.4	317	5640	5570	4.84	89.40	71525.77

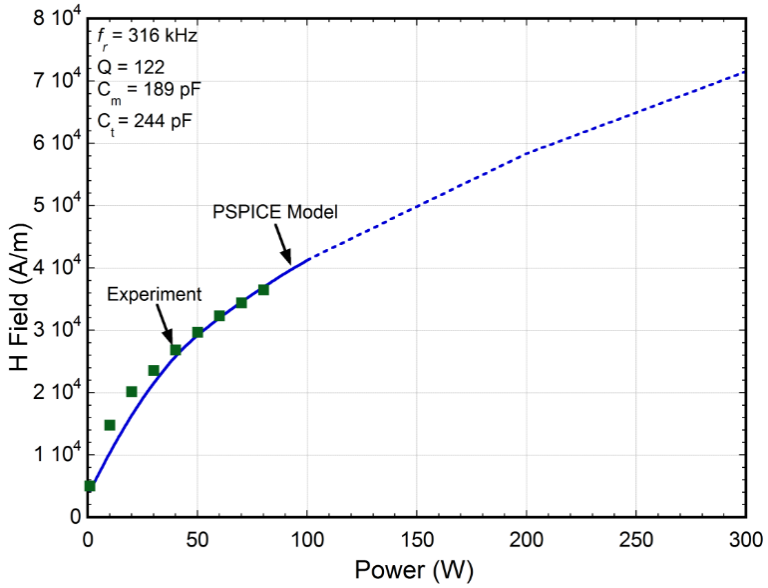

Figure 6-12 Comparison of the experimental and PSPICE model magnetic field.

6.3.3 Verification of Measured Magnetic Field using Ferrite Core Reluctance Model

To further validate the measured and calculated/simulated (PSPICE) magnetic field, we performed simple theoretical calculations based on the reluctance model as shown in Figure 6-13b. We started with basic Ampere's law to determine the net Magnetomotive Force (MMF) around a closed path which is equal to the total current passing through the

path. For a closed loop ferrite core of effective magnetic length l_e and an external current i_{ext} carried through n turns of wire as shown in Figure 6-13a, total MMF can be written as

$$MMF = \oint H \cdot dl = Hl_e = ni_{ext}. \tag{6.11}$$

Total MMF is the summation of the core and air gap,

$$MMF = MMF_{core} + MMF_{air} = ni_{ext}. \tag{6.12}$$

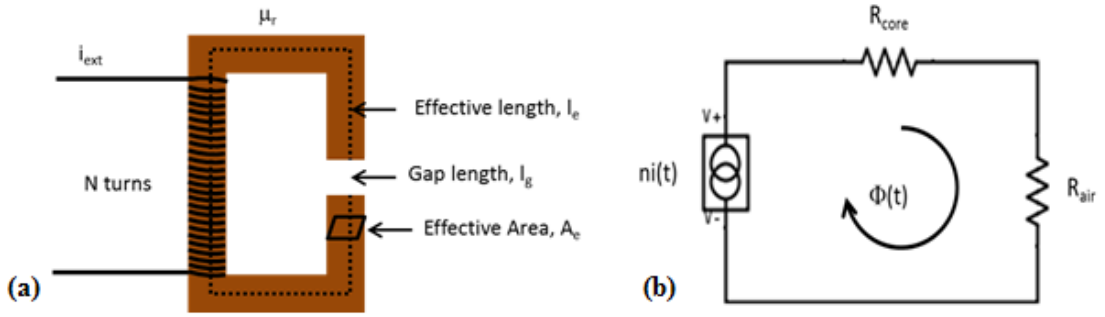

Figure 6-13 Circuit representation of UU gapped ferrite core used for fringing field reluctance calculations.

Writing the MMF in terms of flux and reluctance as in Figure 6-13 $MMF_{core} = \Phi R_{core}$ and $MMF_{air} = \Phi R_{air}$ (Hopkinson's Law),

$$MMF = \Phi(R_{core} + R_{air}) = ni. \tag{6.13}$$

From Faraday's law of induction,

$$v = n\frac{d\Phi}{dt} = L\frac{di}{dt}, \tag{6.14}$$

substituting for $\Phi = \dfrac{ni}{(R_{core} + R_{gap})}$ we get,

$$L = \frac{n^2}{(R_{core} + R_{gap})}. \tag{6.15}$$

Magnetic flux in terms of magnetic field (i.e., magnetic flux per area) can be written as

$$\Phi = \oiint B \cdot dS \,, \tag{6.16}$$

rewriting,

$$B = \frac{\Phi}{A_{eff}} = \frac{ni}{A_{eff}\left(R_{core} + R_{gap}\right)}. \tag{6.17}$$

Magnetic field can be theoretically obtained by substituting for the effective area A_{eff}, reluctance of the core R_{core} and air gap R_{gap}. The reluctance of the core and air gap can be written as a function of length, their effective area and permeability,

$$\mathrm{R_{core}} = \frac{\mathrm{l_{core}}}{\mu_0 \mu_{\mathrm{rcore}} \mathrm{A_{eff}}} \text{ and } \mathrm{R_{gap}} = \frac{\mathrm{l_{gap}}}{\mu_0 \mathrm{A_{eff}}}. \tag{6.18}$$

However, the reluctance equation for the air gap does not take into account any fringing magnetic field thereby creating a discrepancy in the calculated magnetic field. To correct for the effect of fringing flux in the gapped region on the arm of the ferrite core with air gap the following correction factor obtained from FEM simulations was introduced [133]. A fringing coefficient "F" for the dimensions of the UU core described in Figure 6-14 can be written as

$$F = \frac{1}{\pi} a\cosh\left[3.396 \times \frac{g/2}{(l_{air}/2)} + 0.15 \times \frac{g/2}{(l_{air}/2)} + 1.1155\right] \text{ and} \tag{6.19}$$

$$\Lambda_g = \mu_0 \frac{A_g}{l_g} + \mu_0 \left(2w + d\right) \times F + \frac{8}{\pi}\left(\frac{g}{2} - \frac{2d}{3}\right). \tag{6.20}$$

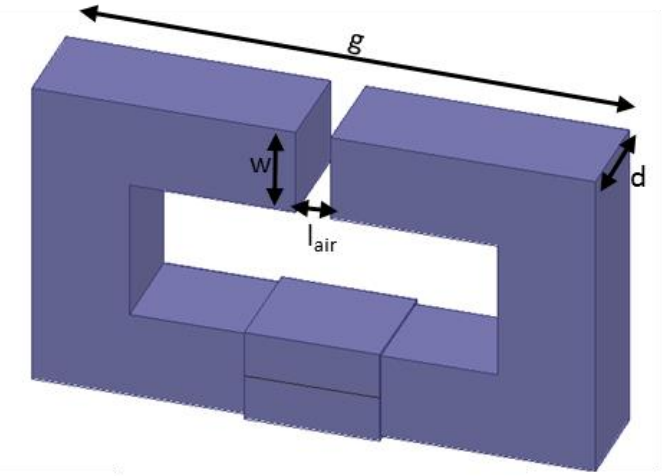

Figure 6-14 Dimensions of UU gapped ferrite core used for fringing field reluctance calculations.

The calculated correction factor for the air gap was then used to re-calculate the reluctance in the air gap,

$$R_{air\_fringing} = \frac{1}{\Lambda_g}. \tag{6.21}$$

From the corrected value of gap permeance, the inductance, magnetic flux and field can be calculated as

$$B = \frac{\Phi}{A_{eff}} = \frac{ni}{A_{eff}\left(R_{core} + R_{gap\_fringing}\right)}, \tag{6.22}$$

where, n is the number of turns in the solenoid, I is the current through solenoid and A_{eff} is the effective area of the ferrite core. 6-15 shows the comparison between measured field, PSPICE model and the theoretical reluctance calculations at resonant frequency of 316 kHz.

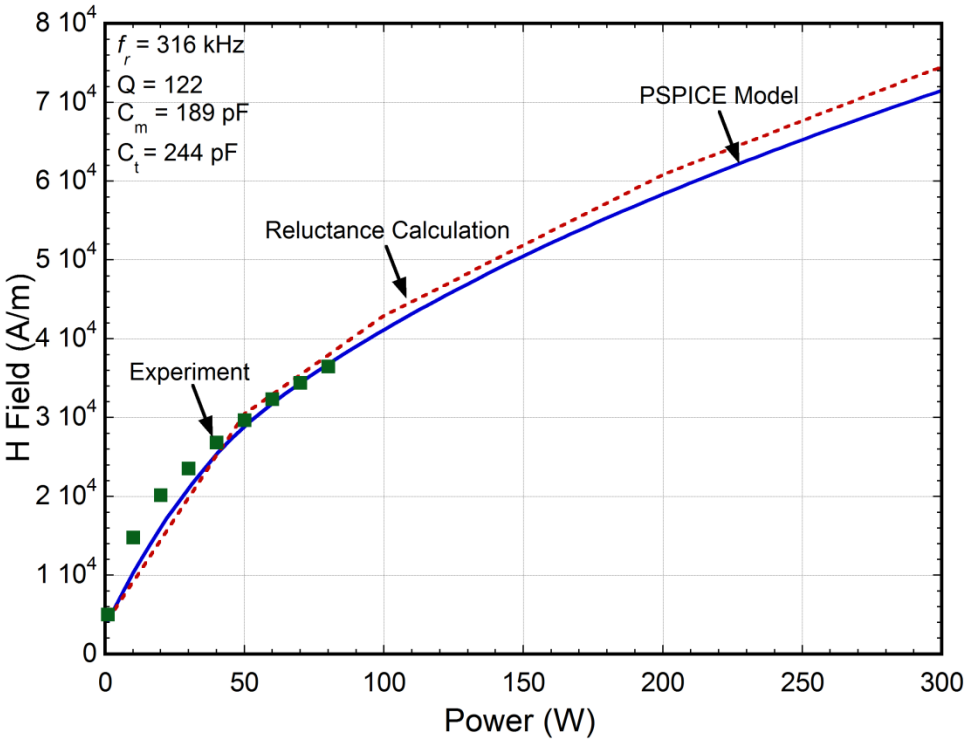

Figure 6-15 Correlation between Experiment, PSPICE and Reluctance Model.

6.4 EM Modeling of *LF* Ferrite Core LCR Resonant System

6.4.1 Ansys Maxwell

The field calculations to visualize the magnetic flux and air gap field in the LCR resonator were performed using Ansys Maxwell which is a Finite Element Analysis (FEA) based simulation tool [134]. Primarily Maxwell is used to solve electromechanical problems such as motors, transformers, solenoids, permanent magnetic, ferrite core etc. The principle behind FEA/FEM and was described in detail in chapter 3. Maxwell offers either a 2D or 3D solution interface. The 2D interface in Maxwell further offers a choice of XY symmetry or RZ symmetry to model a physical geometry accurately in 2D. User selects the solution interface based on the problem type and geometry restrictions. Next step is the selection of the solver which are classified as "Electric" and "Magnetic" solvers. As the name indicates the "Electric" solvers are used to solve for electric field, voltage,

current density, electric potential etc. Depending on the solution the user is interested in, it is further classified as (i) Electrostatic (ii) DC Conduction (iii) AC Conduction and (iv) Transient. Here the AC conduction and Transient analysis are used for frequency domain and time domain calculations. Electrostatic is used to solve static electric field cases and DC conduction is used for voltage, electric potential etc. The "Magnetic" solver classified into (i) Magnetostatic (ii) Eddy Current and (iii) Transient solvers are used for permanent magnets simulation. Similar to the electric solver, eddy current and transient are used for frequency domain and time domain respectively.

6.4.2 Geometry Modeling, Meshing and Field Visualization

To simulate the ferrite core in Maxwell, the "Magetostatic" solver in the 3D solution interface was selected since our goal was to determine the magnetic flux and field in the gapped ferrite core for static conditions. The 3D solution interface though more resource consuming, was chosen to accurately model the rectangular ferrite, airgap and the solenoid. The geometry of the ferrite core inductor was based on the experiment setup of the low frequency ferrite core LCR resonator. Two U-cores with an air gap of 10 mm on one side similar to the experimental setup was constructed. The permiability of the ferrite material (EPCOS N27) was defined through its BH curve. To reduce solution time and meshing errors arsing through "skinny elements" the solenoid was modelel as a solid rectangle aound the lower arm of the two U-cores. Copper was assigned as the material parameter. Length and thickness of the rectangular solenoid closely follows the experimental lenth and wire thickness. Current through the solenoid was defined via "excitation" to be 30 A. This translates to 1A current through each turn of the solenoid and we have 30 turns in our inductor. Further, to indicate individual wires we define the type

as stranded. The geometry is simulated to vizualize the magnetic field (H) and flux (B) distribution of the ferrite core inductor. Figure 6-16 shows the ferrite core inductor gemoetry in Maxwell and its field distribution.

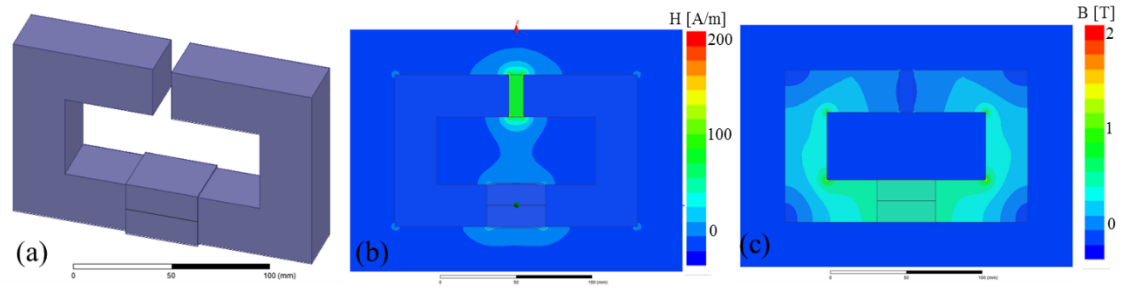

Figure 6-16 Ansys Maxwell magnetostatic simulations (a) LCR geometry (b) Magnetic Field H in A/m and (c) Magnetic Flux B in Tesla.

Further, for possible animal model experiments the minimum gap required would be 15 mm. The increase in gap would lead to much lower magnetic field in the air gap. To compensate for the desreased magnetic field, we explored various gometry modifations for field focusing. The 3D magnetostatics solver was used to simulate the effect of geometry modification such as ferrite arm focussing at the sample region. The 30 turn solenid and the current excitation were similar to the original model/simulation. The the magnetic field (H) and flux (B) distribution of the different geometry modification can be seen in Figure 6-17. We observe the homogenetiy of the magnetic field in the air gap reduce as the focusing increases in Figure 6-17a and Figure 6-17b.

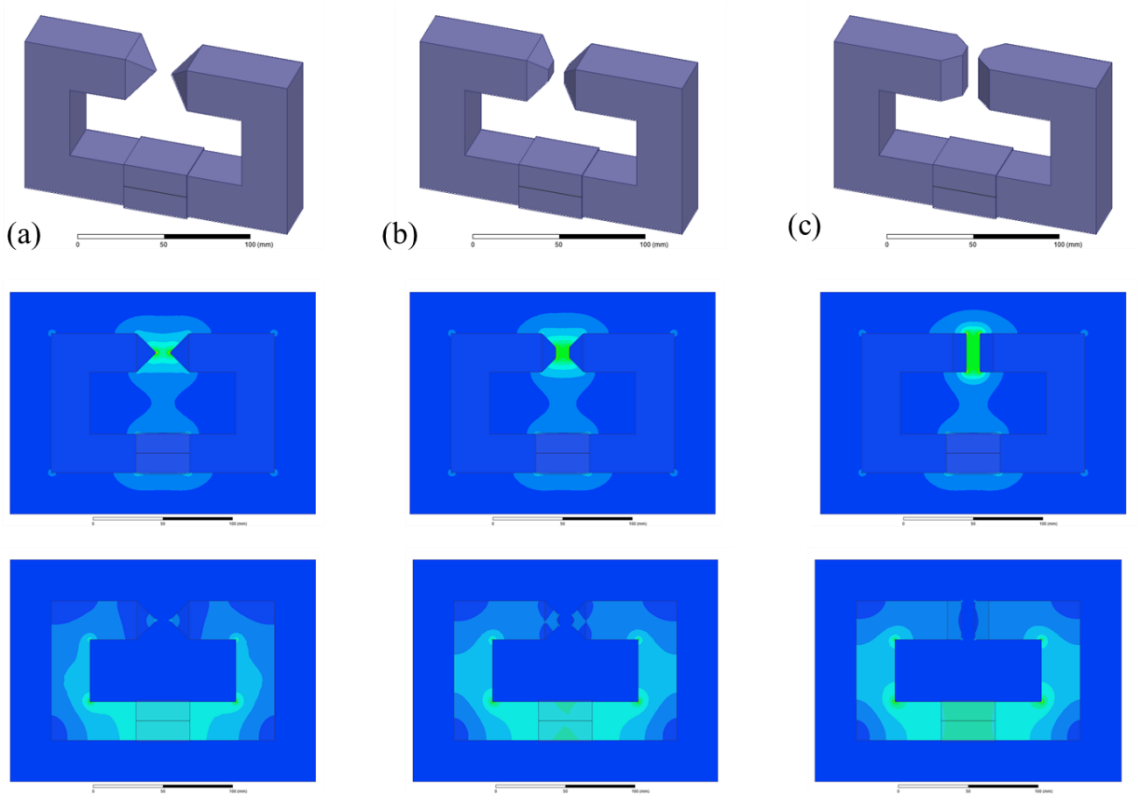

Figure 6-17 Ansys Maxwell magnetostatic simulations depicting the geometry modification, magnetic field (H) and flux (B) distribution for three different ferrite focusing geometries.

6.5 Preliminary SAR of SPIO NPs

To test the low frequency ferrite LCR resonator we used the same superparamagnetic iron oxide NPs (5 nm) embedded in a dextran matrix (30 nm) from chapter 4 and 5. The temperature T of the SPIO NPs sample was measured as a function of time t for a given input power. NPs temperature measurement, slope calculation all follow the same format as the previous chapters. The T vs t was measured for two different initial/cooling temperatures of 20.5^{o}C and 37.5 ^{o}C. In the first case, the water bath circulator was set at a temperature of 20.5^{o}C suitable for characterization of MNPs. However, in case of cell studies and/or animal model studies the water bather circulator has to be set at 37.5^{o}C. It is of importance to check the stability of the system for increased core loss due

to higher temperature. Figure 6-18 shows the SPIO T *vs* t temperature stability of the system at 20.5°C with 37.5°C which is vital to study heating characteristic of cells functionalized with NPs. In Figure 6-19, we look at the first 10s slope of the two measurements. The ΔT/Δt slopes at 20.5°C and 37.5°C are 0.06187 and 0.0666 respectively. The slope of 37.5 °C is slightly larger than the20.5 °C slope. However, the difference is non-significant and the system can be consider stable at 37.5 °C.

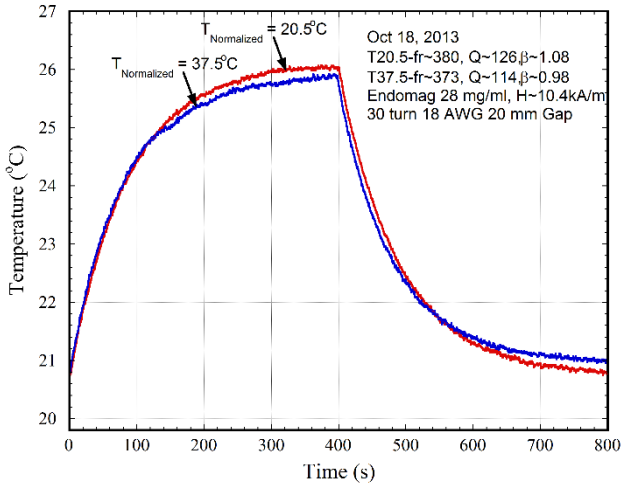

Figure 6-18 T *vs* t curve of 28mg/ml SPIO measured for two different stabilization temperatures.

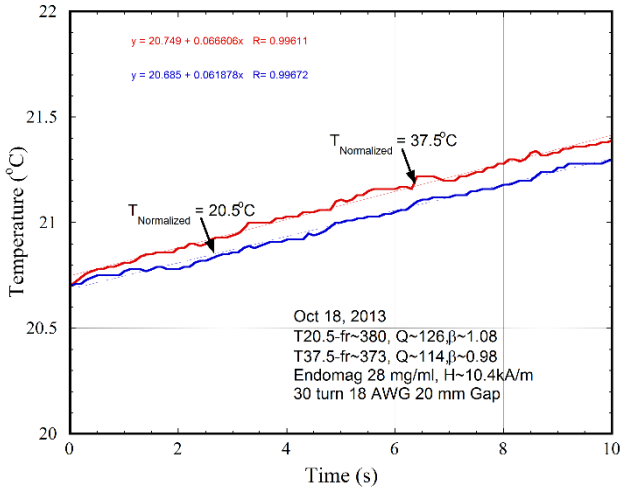

Figure 6-19 ΔT/Δt slopes curve of 28mg/ml SPIO measured for two different stabilization temperatures.

Table 6-3 SAR of SPION in ferrite

Resonator Type	f_r (kHz)	H Field (kA/m)	Slope ΔT/Δt (˚C/s)	SAR_M (kW/kg)	SAR_M/fH^2 (Wsm^2/kgA^2)
Ferrite	370	10.4	0.06	0.259	$6.5e^{-12}$

A low frequency magnetic field heating system that can be utilized in thermal triggering of MNPs was designed and developed in this chapter. Primarily, the magnetic field generator was developed to remove the EDL/E_z interaction heating. The EDL component is variable since it can be easily changed by either the bio-conjugate surrounding the MNPs or the counter-ion concentration of the colloidal suspension. Thus the current magnetic field generator utilizes ferrite core to remove any electric field component and maximizes magnetic field. Lower frequencies in kHz range (100 kHz to 500 kHz) was utilized to minimize any additional non-specific heating to healthy tissues. SPIO NPs were tested for their heating efficiency in the system and their SAR was calculated.

Chapter 7 Non-Thermal Cancer Therapy

In this chapter, we explore different methods of tumor apoptosis to serve as an alternative to hyperthermia treatment. To solve the problem of nanoparticle concentration around the tumor site in hyperthermia we look into targeting specific ion channels such as mechanosensitive using functionalized nanoparticles.

7.1 Effect of external stress on cancer cell

The goal of this chapter was to study the possibility of inducing cancer cell death through mechanical stress on the membrane. External mechanical stress on the cell has a direct impact on the microenvironment of the cell affecting the cytoskeleton. The cell responds to the external stimuli by remodeling the cytoskeleton which is viscoelastic and provides a continuous mechanical coupling throughout the cell as it changes. This in turn, induces changes in certain cellular process such as, internal cell stress, extracellular matrix (ECM), focal adhesions (FA) etc. This conversion of mechanical forces to biochemical interactions is referred to as mechanotransduction. The different mechanotransduction mechanisms in the cell due to external stimuli are described in Figure 7-1 [135, 136].

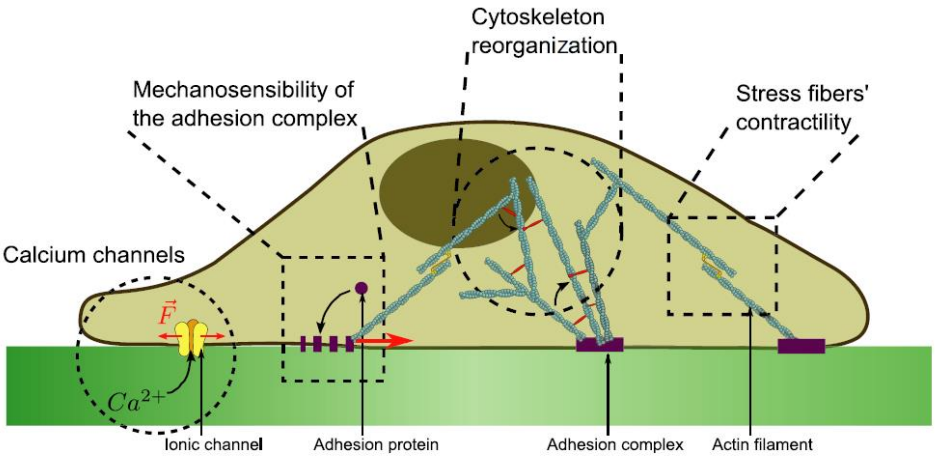

Figure 7-1 Effects of external stimuli on the cellular process.

Such external mechanical stimuli on the cell, depending on the force induced can not only membrane rupture, but more importantly influence various biochemical processes in the plasma membrane/ECM/FA ultimately leading to cell apoptosis. For example, changes in ion channel activity at the plasma membrane of cells may convey mechanical stresses from the cell membrane to internal organelles causing changes in gene transcription and inducing apoptosis [137]. Other pathways of mechanically induced cell damage can include activation of Caspase-3 protease pathway [138], TNF-related apoptosis-inducing ligand (TRAIL, Apo2L) [139] and cleavage of caspases 3 and 9 [140].

The cellular response to external force results in several induced internal force. Thus it is important to understand the forces generated by the cell itself. As an example, the traction forces i.e., adhesion force exerted by the cell to the substrate through FA's is around 1-100 nN. Table 7-1 summarizes the integral force origin, their force in Newton's and the corresponding literature adapted from [136].

Table 7-1 Cell based forces.

Biological System	Force	Reference
Single motor	~ few pN	[141, 142]
Single protein stretching	2-10 pN	[143]
Single stress fiber stretching	10 nN	[144]
Focal adhesion (FA)	1-100 nN	[23, 24]
Actin network	10pN-few nN	[145, 146]
Single cell	~100 nN	[147, 148]

It has been shown that direct external stimuli such as AFM tips produce a force in the range of nN to μN per μm^2 on the cell membrane [149, 150]. However, remote methods of inducing force on the cell are of much interest in therapeutic tumor applications. Existing studies show that static fields (3T – 7T) as in MRI do not have any significant effect on the human body/cells. Static fields in the range of 15T have shown to affect cell differential and viability [151]. Further, strong magnetic field gradients on diamagnetic structures cause an effect analogous to microgravity [26, 152, 153]. This effect is referred to as diamagnetic levitation and it extends a significant force on the cell affecting morphology, differentiation etc. [154, 155]. This process is directly related to utilizing remote force inducers on biological structures since most cells are diamagnetic. In this chapter, we explore remote force extended through via external magnetic fields [16, 22, 87, 88, 156]. For example, magnetic property of MNPs of certain material allow for their orientation to be controlled by an alternating magnetic field, thereby creating an oscillatory effect [27]. In the subsequent sub-chapters we explore this mechanism, its advantage and drawbacks to design a remote magnetic field gradient generator.

7.2 Verification of mechanical movement of magnetic microdiscs

Under the influence of an alternating magnetic field, magnetic nanoparticles functionalized on the cell membrane have been shown to induce a higher force causing apoptosis through either receptor clustering, twisting cytometry, magnetic tweezers etc. [16, 87, 88]. Figure 7-2 schematics shows the possible membrane damage caused by permalloy microdiscs movement in low frequency alternating magnetic field as reported by a research group [27]. Special spin vortex magnetic state of the permalloy was utilized to oscillate microdiscs [157]. As a first step to validate and study the shortcomings of

utilizing permalloy microdiscs, we study the magnetic property of these discs through micromagnetics simulation. The goal of the simulation studies was to understand the nucleation and annihilation of the magnetic domains specifically the vortex structure formation. By studying the magnetization changes in the material step by step through the hysteresis loop, the evolution of the domain structures can be more clearly understood at a nanoscale level.

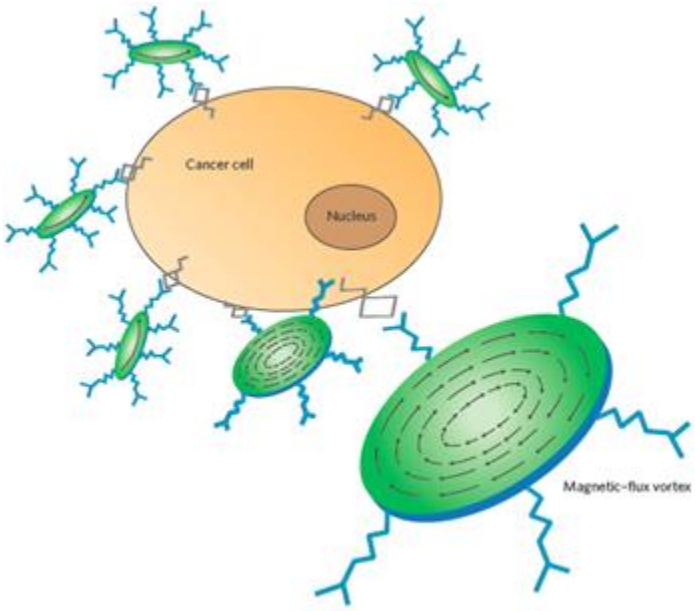

Figure 7-2 Schematic representation of functionalized microdiscs for targeted magneto-mechanical cancer cell apoptosis.

We used finite element micromagnetics simulation software (NMAG-Python interface) developed at the University of Southampton, United Kingdom [158]. The nanodiscs geometry was drawn via any CAD software capable of producing the output file as cgs, stl, iges or step format. In our case, we used csg where the geometry is defined through an ASCII text input. The csg file was then used as an input for the finite element mesh using NETGEN to generate the tetrahedral and triangular mesh elements [159]. All visualizations shown in Figure 7-3 were visualized through the 3D visualization tool Mayavi [160]. In

these simulations, we used magnetic properties of permalloy, a saturation magnetization of 795774 A/m and an exchange stiffness constant of 13.0e-12 J/m. Typical nanodisc values of diameter 200 nm and thickness 30 nm were used to obtain spin vortex state [157].

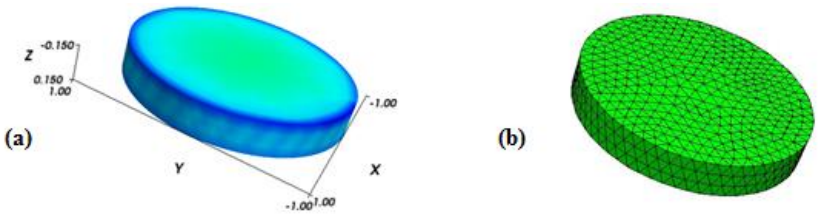

Figure 7-3 (a) Nanodisc geometry construction using CGS and (b) finite element mesh optimization using NETGEN. All vizualizations are done via Mayavi.

A maximum external magnetic field of 100 kA/m was applied along the plane of the nanodisc in steps of 5 kA/m to obtain the hysteresis loop. The vortex movement shown in Figure 7-4 with respect to the external magnetic field applied indicates the nanodisc oscillation along the plane of the magnetization.

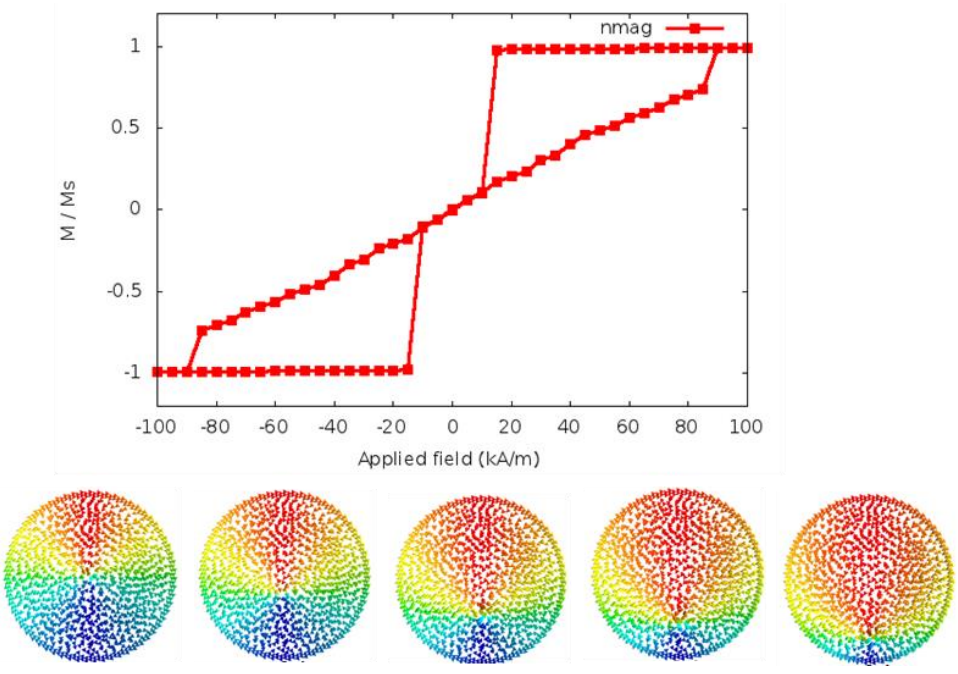

Figure 7-4 Hysteresis loop of Permalloy Nanodisc of diameter 200nm and thickness 30nm depicting the vortex nucleation and annihilation.

The vortex property of the permalloy nanodisc is dependent on the material, shape and size. However, there are several drawbacks in using permalloy nanodiscs. The vortex structure of the magnetic domains is an interplay of the material properties, particle size and particle shape. Thus to effectively utilize this method of using permalloy MNPs as remote force inducers we are severely restricted in the magnetic nanoparticle design apart from the materials cytotoxicity. Thus, in order to cause mechanical movement of nanoparticles not limited by the material or shape we focus on alternate methods to induce force on the cell membrane.

7.3 Design of Magnetic Field Gradient Generator for Modulation of MNPS

We designed a magnetic field/gradient generator capable of generating both static and sweeping field and gradients to be applied to the cell with and without the MNPs. The generator was designed to facilitate mechanical movement of MNPs which is not limited by the material, size or shape.

Here four permanent magnets (NdFeB) high surface gauss of 3600 (0.36 Tesla) were embedded in an acetal plastic plate. The plates were placed parallel to one another with a microcontroller to adjust the distance of separation. To achieve the alternating magnetic field and sweeping gradient the generator was connected to a synchronous dc motor of 15 rpm, which corresponds to 0.25 Hz. The two magnets pairs were oriented in Helmholtz (attractive) and anti-Helmholtz (repulsive) configuration. A varying magnetic field gradient (sweeping) wass setup through the alternating Helmholtz and anti-Helmholtz arrangement of bulk NdFeB magnets. The entire MNP optical modulation detection setup is described in Figure 7-5a. The schematics for the system at a vertical orientation for MNP

rotation study is shown in Figure 7-5b. Here, the cuvette with MNP suspension was placed between the two plates. The plate separation was set at 15 mm to accommodate the 12 mm wide quartz cuvette. Close up of the experimental optical measurement setup for the detection of modulation of the MNPs along with the generator, beam spot and the sample cuvette is shown in Figure 7-5c.

In the experimental setup, a low powered Helium Neon laser beam of 0.5 mW power, beam diameter 0.48 mm and wavelength 632.8 nm was directed to a spatial filter (Newport 900). The filter contains an M-10X objected lens which corrects for the scattering of the laser bean from duct particles. This so called "dirty" spatial profile was then passed through a pin-hole with an aperture size of 25μm to obtain the "clean" spatial profile. This was further passed through a collimator to focus the beam onto the sample cuvette containing the MNPs suspension which sits in between the magnet plates. A final beam diameter of ~ 0.5 mm was incident on the MNP containing cuvette. Depending on the movement of the nanoparticle in the magnetic field the output light intensity incident on the photo-detector varies. The light output from the photo-detector was collected and plotted as a function of light intensity versus time to observe the intensity variations.

The size of the magnets and the two different orientation contribute to the non-uniform field distribution across the quart cuvette for even static conditions. Further, during AC (motor rotation) the change of the magnetic field (both magnitude and direction) would affect how the MNPs are oriented. This in turn, would have a direct impact on the cell membrane to which the MNPs are adhered when the MNPs are modulated by the alternating magnetic field. The magnetic field distribution on the quartz cuvette was calculated using Ansys Maxwell described in Chapter 6. Figure 7-6 shows the vector

distribution of the magnetic field at every 60 degree of the plate rotation. Here, red and blue indicate maximum and minimum magnetic field magnitude respectively. As observed from Figure 7-6 the magnetic field distribution varies along the length of the cuvette and plate rotation. The simulations show that a MNP would experience a rotational force in the alternating magnetic field.

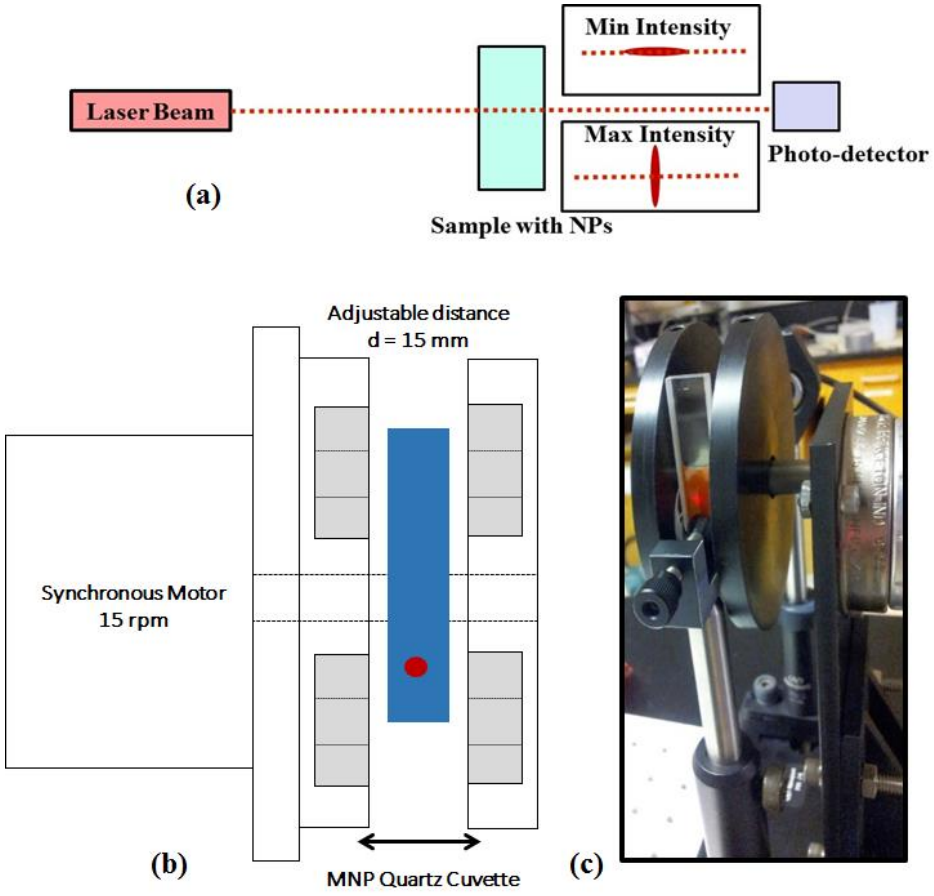

Figure 7-5 (a) Schematic depicting the optical nanoparticle modulation detection setup, (b) Geometry of the vertical MNP setup and, (c) Close-up of experimental setup.

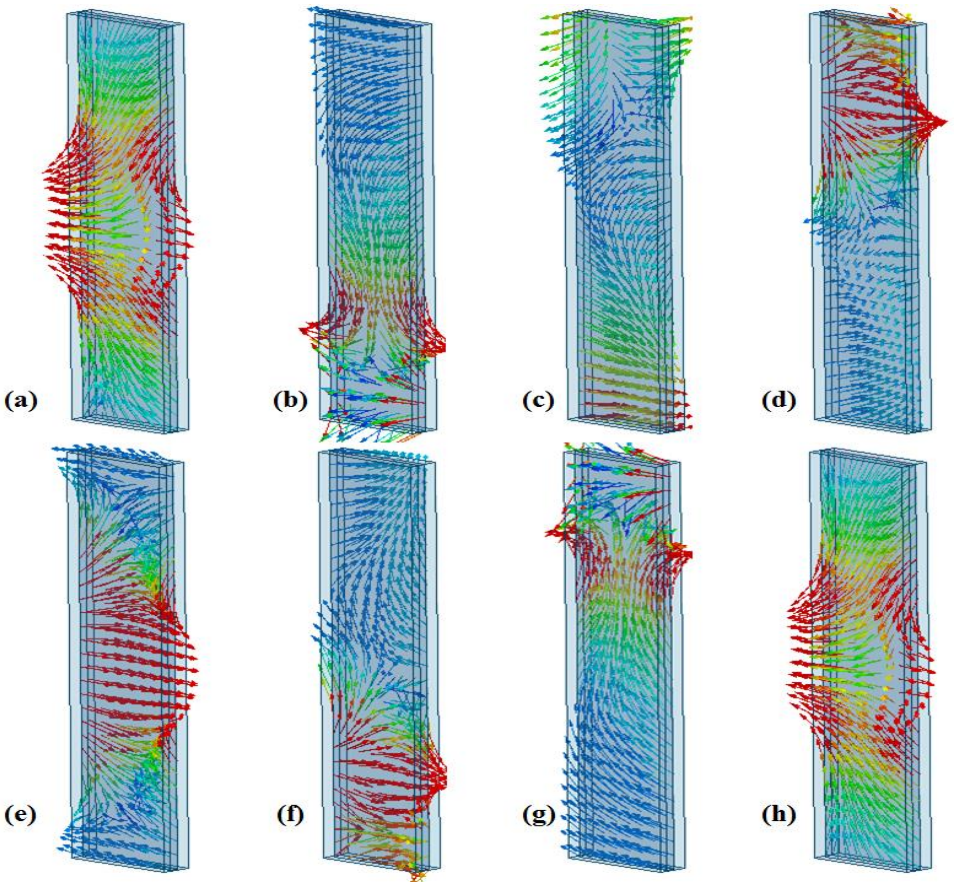

Figure 7-6 Magnetic vector field distribution in the sample holder for varying degree of rotation (a) 0 Degree, (b) 60 Degree, (c) 90 Degree, (d) 120 Degree, (e) 180 Degree, (f) 240 Degree, (g) 300 Degree and, (h) 360.

7.3.1 AC Magnetic Field Measurements

To experimentally verify the MNP rotational movement in ac magnetic field, we measured the magnetic field during ac (motor rotation) to verify if we achieve an alternating magnetic field of frequency 0.25 Hz corresponding to 15 rpm. For this we used a gaussmeter and recorded the field variation based on the plate rotation for two different plate separation. Here the gaussmeter's Hall probe was placed at the sample location to identify the field variation at the sample location. Figure 7-7 shows the field variation for two different plate separation distance of 15mm and 17mm. A 4s interval corresponding to

one cycle of rotation can be observed in both the plate separations. Further, Fast Fourier Transform (FFT) of the magnetic field variations was calculated.

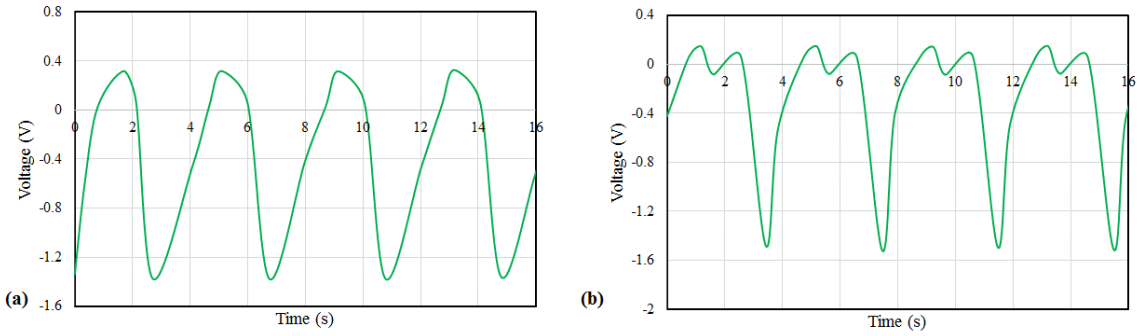

Figure 7-7 Field measured using Gaussmeter for rotation of plates using 15 rpm motor for plate separation of (a) 15 mm and (b) 17 mm.

Figure 7-8 shows the FFT of the recorded magnetic field variations. The obtained frequency spectrum of the field oscillations show a dominant peak at 0.25 Hz which corresponds to 15 rpm of the motor rotation. The solid red line corresponds to 15mm gap and the dotted blue line corresponds to the 17 mm gap. In Figure 7-8 both the plate gaps show a major peak at 0.25 Hz and also shown is its secondary harmonic at 0.5 Hz.

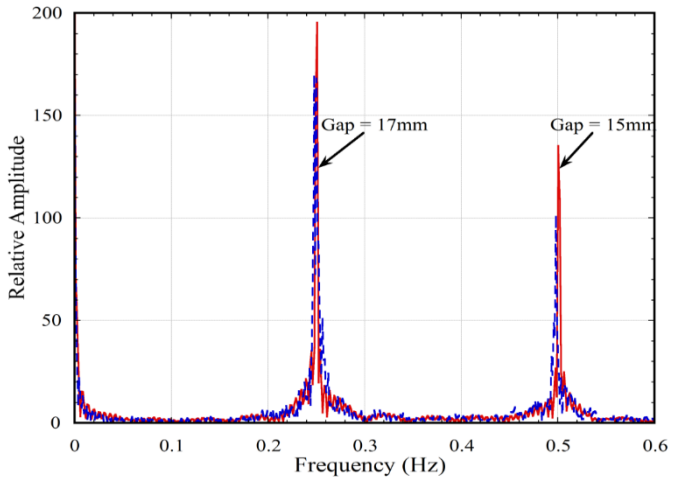

Figure 7-8 FFT of field measurement for rotation of plates using 15 rpm motor for plate separation of 15 mm and 17 mm.

7.3.2 Measurements of MNP movement in AC field

Once the field oscillation frequency was been verified, next we tested the system for rotational movement of MNPs. For this, we purchased iron oxide nanorods (powder) from NanoAmour^{TM}. The iron oxide nanorods of length 400-700nm and thickness 30-700nm were suspended in DI water to obtain various concentrations of iron oxide nanorods suspension. Figure 7-9a shows the TEM of the nanorods. The nanorod suspension was placed in the quartz cuvette which is housed between the two plates in the magnetic field generator. Data from the photodiode was collected continuously as a function of time for the modulation in light intensity. Figure 7-9b shows the light intensity recorded for 200s from the photo-detector for the nanorod oscillation. During the first 50s the motor was in "off" state where we observe no variations in light intensity. For the remaining 150s of "on" state we clearly observe light intensity variations that follow the plate rotation. A close view of the nanorod oscillation in Figure 7-9c shows that one cycle of 4s corresponds to the motor rotation at 15 rpm i.e, 0.25 Hz. The FF of the light intensity modulation of the nanorod in Figure 7-9d shows a distinct peak at 0.25 Hz confirming that the rotation movement of nanorods under the influence of the alternating magnetic field. Thus we are able to establish the MNPs rotational movement in our magnetic field and gradient generator through this proof of concept experiment.

The system was also tested for spherical MNPs as an extension for our proof of concept study. Here we used carbon onion nanoparticles with nickel iron core of 20 nm diameter surrounded by three to four layer of graphene obtained from Rice University [161]. These powder nanoparticles were then suspended in pluronic to obtain a concentration of 0.3 mg/ml. First we tested pluronic solution in the optical modulation

system which by itself showed no change in intensity of light as seen in Figure 7-10a. While the carbon onion nanoparticle in Figure 7-10b showed a distinct trend of MNP oscillation in response to the alternating magnetic field.

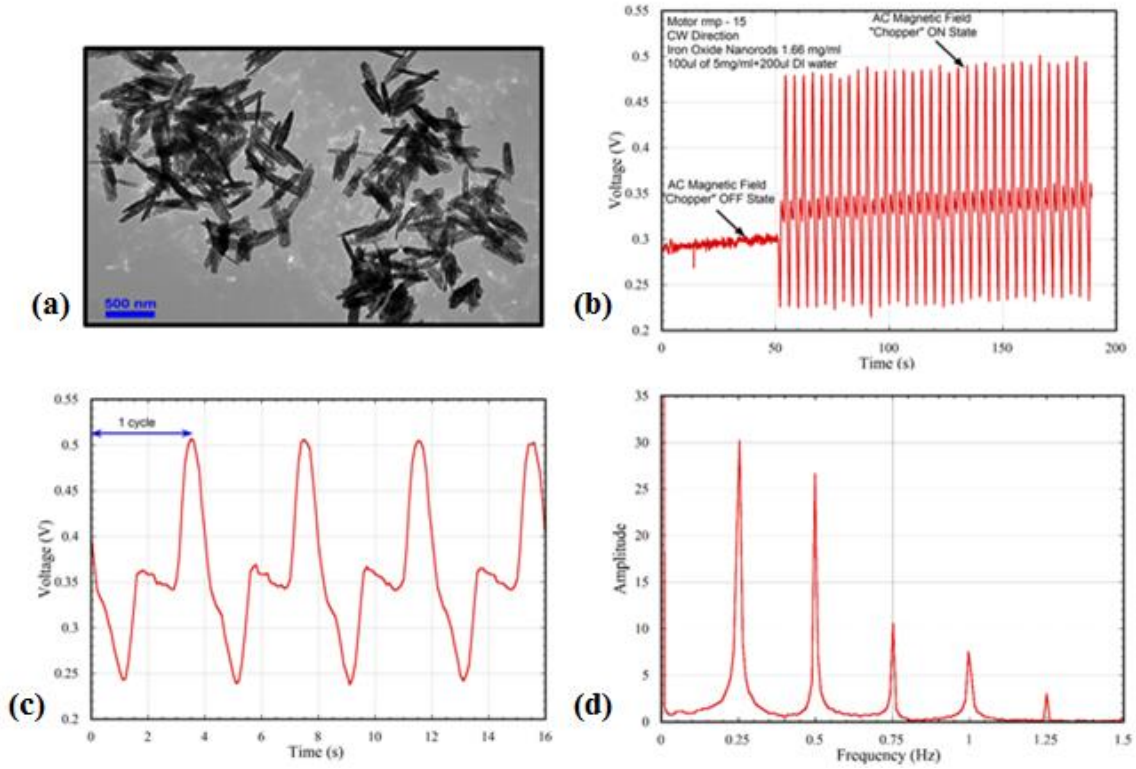

Figure 7-9 (a) TEM of nanorods (b) Output intensity of light measured from the nanorods movement in the magnetic field (c) A 16s view (d) FFT of the light intensity output.

Next, we also measured iron oxide/graphene nanoribbons of two different concentrations to extend our magnetic field and gradient generator to MNPs of different shape, size and material. The nanoribbons were also obtained from Rice University [162] and are suspended in pluronic. Distinct light intensity modulations of the nanoribbons can be observed in Figure 7-11a and Figure 7-11b for two concentrations of 0.3 mg/ml and 0.1 mg/ml respectively.

However, we do notice difference in oscillation period in the latter two cases when compared to the iron oxide nanorods. This can be attributed to the spherical shape of the MNP, wherein the light intensity modulation occurs by particle diffusion i.e., translational motion rather than by particle rotation i.e., torque. This response is similar to the magnetic tweezers, receptor clustering and twisting cytometry observed in literature when spherical MNPs are subjected to alternating magnetic flied [15, 16, 22, 87].

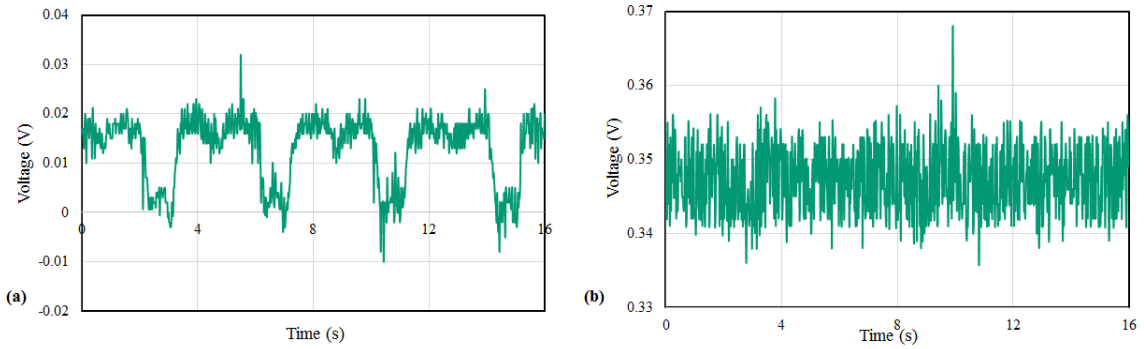

Figure 7-10 Output intensity of light measured from magnetic field modulation of (a) Carbon onion nanoparticle suspended in pluronic and (b) Pluronic.

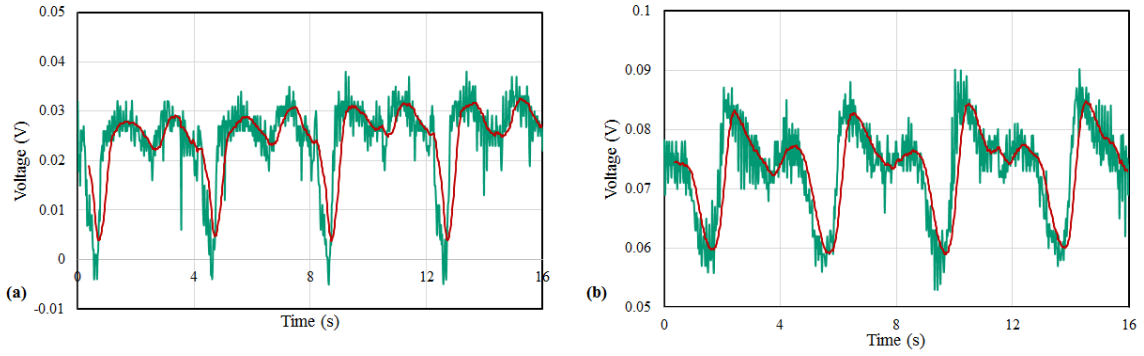

Figure 7-11Output intensity of light measured from modulation of iron oxide/graphene nanoribbons suspended in pluronic of concentrations (a) 0.3 mg/ml and (b) 0.1 mg/ml.

7.4 Calculation of Magnetic Force on Cell Membrane

Apart from utilizing MNPs, our goal was to also study the effects of magnetic field gradient on the cell viability. To that end, we explored a four-fold approach of utilizing external magnetic fields as "force-inducers", Figure 7-12 [163].

1. Static magnetic field and gradient
2. Sweeping magnetic field and gradient
3. MNP induced translational force under static fields and gradient
4. MNP induced rotational force under sweeping field and gradient

The magnetic energy experienced by any object placed in a magnetic field can be written as

$$U = -\frac{mB}{2}, \tag{7.1}$$

where, $m = \chi VB/\mu_0$ is the dipole moment with χ and V representing the susceptibility and volume of the cell respectively and μ_0 is the permeability of free space $4\pi \times 10^7$ H/m. Since the volume of a biological cell is relatively small, we assume that the magnetic field and susceptibility are constant over the cell. Re-writing magnetic energy

$$U = -\frac{\chi V}{2\mu_0} B^2. \tag{7.2}$$

Calculating the magnetic force, $\vec{F}(x, y, z) = \nabla U$,

$$\vec{F}(x, y, z) = \frac{V\Delta\chi}{\mu_0} \vec{B}.\vec{\nabla}\vec{B}. \tag{7.3}$$

7.4.1 Dependency on field gradient and medium susceptibility

The magnetic force is dependent on the product of the magnetic field $\vec{B}$ (T) with the magnetic field gradient $\nabla\vec{B}$ (T/m). Since the magnetic force is directly proportional to

the product of the two, it is often referred to as the "force product" $\vec{G}(\vec{B}) = \vec{B} \bullet \nabla \vec{B}$ given in T^2/m [164]. Expanding the force product in rectangular co-ordinates,

$$\vec{G}(\vec{B}) = \vec{B}.\vec{\nabla}\vec{B} = \left(B_x, B_y, B_z\right)\begin{pmatrix} \frac{\partial}{\partial x} \\ \frac{\partial}{\partial y} \\ \frac{\partial}{\partial z} \end{pmatrix}\begin{pmatrix} B_x \\ B_y \\ B_z \end{pmatrix}. \tag{7.4}$$

Gradient of a vector, in our case $\vec{B}$ field is a second order tensor,

$$\vec{G}(\vec{B}) = \vec{B}.\vec{\nabla}\vec{B} = \begin{pmatrix} B_x \frac{\partial B_x}{\partial x} + B_y \frac{\partial B_x}{\partial y} + B_z \frac{\partial B_x}{\partial z} \\ B_x \frac{\partial B_y}{\partial x} + B_y \frac{\partial B_y}{\partial y} + B_z \frac{\partial B_y}{\partial z} \\ B_x \frac{\partial B_z}{\partial x} + B_y \frac{\partial B_z}{\partial y} + B_z \frac{\partial B_z}{\partial z} \end{pmatrix} = \begin{pmatrix} G_x(B_x) \\ G_y(B_y) \\ G_z(B_z) \end{pmatrix}. \tag{7.5}$$

Magnitude of a tensor in our case the force product $\vec{G}(\vec{B}) = \vec{B}.\vec{\nabla}\vec{B}$ was determined by taking the square root of the matrix inner product. Thus we get,

$$\left|\vec{G}(\vec{B})\right| = \left|\vec{B}.\vec{\nabla}\vec{B}\right| = \sqrt{\left[G_x(B_x)\right]^2 + \left[G_y(B_y)\right]^2 + \left[G_z(B_z)\right]^2}\ . \tag{7.6}$$

The magnetic force on a cell apart from being strongly dependent on the magnetic field and magnetic field gradient, is also dependent on the cell/tissue susceptibility difference. Most biological cells are weakly diamagnetic with the exception of RBCs. The surrounding tissue is slightly less diamagnetic than the cell itself. Due to the difference in susceptibilities the magnetic force induced on cell membrane is larger, $\Delta\chi = \chi_{cell} - \chi_{medium}$. Magnetic force can also be increased by making the surrounding medium/tissue more paramagnetic. MRI contrast agents such as gadolinium (Gd) can be used to increase

magnetic force on cell. Its paramagnetism creates a larger difference between the cell and the medium [165].

7.4.2 Additional Effect of Nanoparticles: Translational and Rotational Force

Further, functionalizing MNPs to adhere on the cell membrane enhances enhance the induced magnetic force on the cell membrane. In static field and gradient the MNP experience a translational magnetic force (N) given by

$$\vec{F}_{Translational} = \frac{V\Delta\chi}{\mu_0}\vec{B}.\vec{\nabla}\vec{B}, \tag{7.7}$$

where, $\Delta\chi = \chi_{MNP} - \chi_{cell}$ is the difference in susceptibility between the MNP and cell, V is the volume of the MNP and μ_0 is the permeability of free space 4π x 10^7 in N/A^2. The "force product" term $\vec{G}(\vec{B}) = \vec{B}\bullet\nabla\vec{B}$ is the same as in Eq. 7.5. In the case of a superparamagnetic NPs a correction factor is introduced to account for the initial magnetization $\vec{M}_0$ [166] to represent translational force (N),

$$\vec{F}_{Translational} = \rho V\nabla(\vec{M}_0\bullet\vec{B})\frac{V\Delta\chi}{\mu_0}\vec{B}.\vec{\nabla}\vec{B}. \tag{7.8}$$

Here, ρ is the density of the MNP. Additionally, in the presence of a very low frequency alternating magnetic field the MNP adhered to the cell will induce a rotational magnetic force. Very low frequency was used here (~Hz), because the rotation of the MNPs will depend on external frequency. The torque (Nm) experienced by the MNP is given as

$$\vec{\tau} = \vec{m}\times\vec{B}, \tag{7.9}$$

where, m is the magnetic moment of the MNP. The MNP when trying to align with the external magnetic field undergoes a torque. In a continuously changing environment such

as an alternating magnetic field, the MNP extends a twisting force on the cell thereby inducing molecular changes.

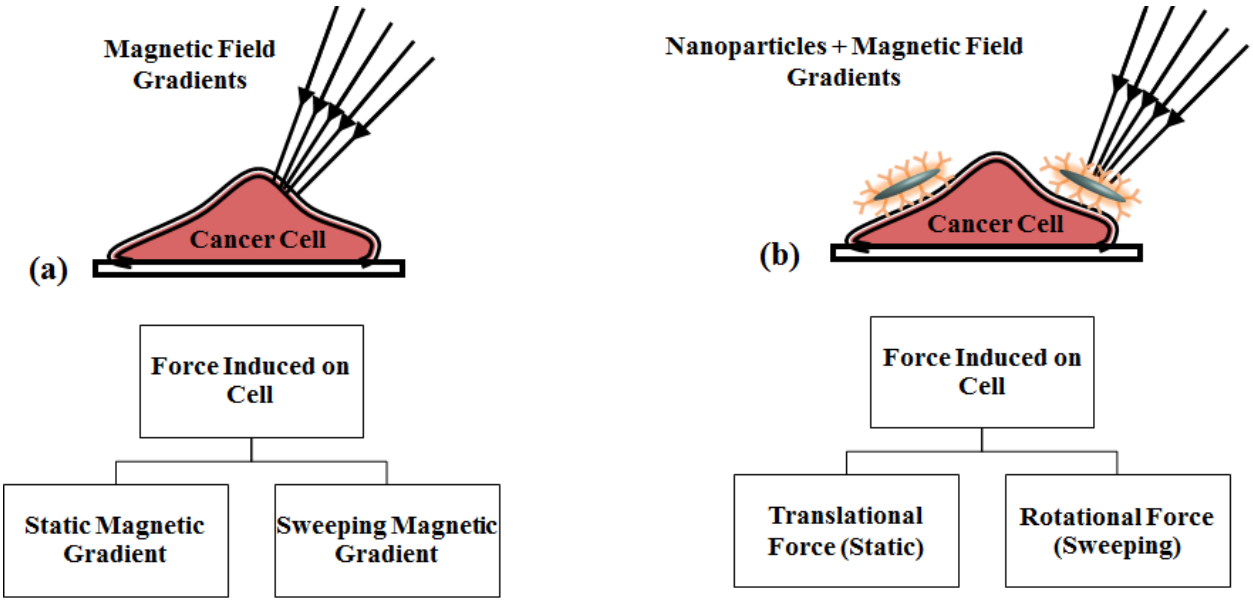

Figure 7-12 Force induced by external (a) magnetic field and gradient, (b) MNPs as force- enhancers.

7.5 Re-Design of Magnetic Field Gradient Generator for Cell Studies

The magnetic field/gradient generator described in Figure 7-5 was re-designed to accommodate cell samples. Figure 7-13 shows the schematics of the magnetic field gradient generator. The generator has the capability of generating both static and sweeping magnetic field/gradients to apply to the cell with and without the MNPs. In the horizontal setup, the plates were placed parallel to one another at an adjustable distance that ranges from 15mm to 4mm. A custom cell chamber was designed to be utilized for cell studies to allow a minimum plate distance of 4 mm to generate maximum magnetic field gradient and consequently maximum force product. To build the cell chamber we used a standard microscope slide (25mm x 75mm) with a gasket for spacing, it was sealed with a coverslip once the cells were placed inside. For the cell experiments the entire magnetic field gradient

generator was placed inside an incubator (Thermo Scientific) to keep cells health and nourished throughout the experiment as shown in Figure 7-14.

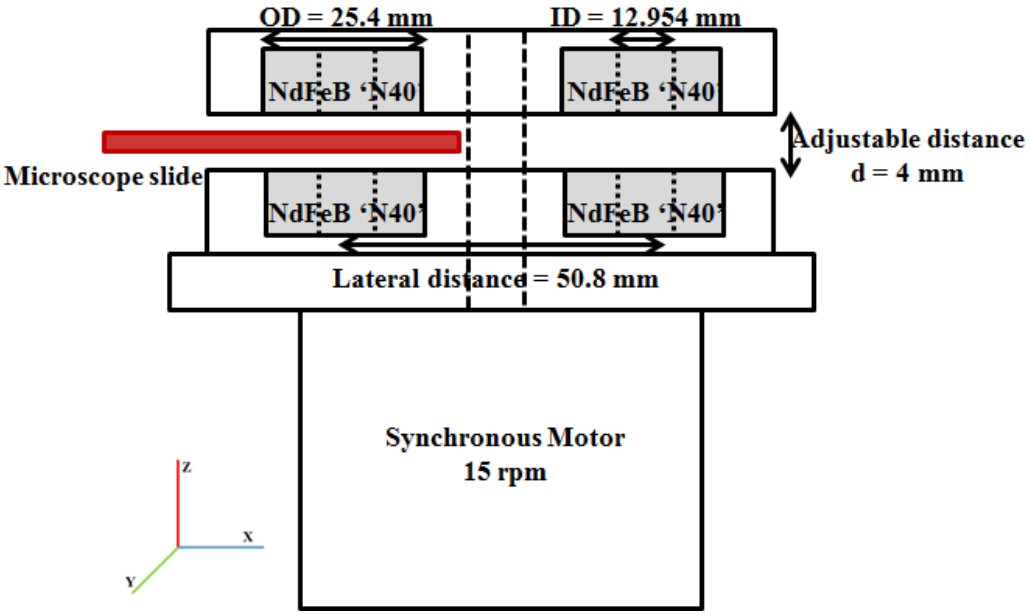

Figure 7-13 Geometry of the static and ac magnetic field gradient generator for cell studies.

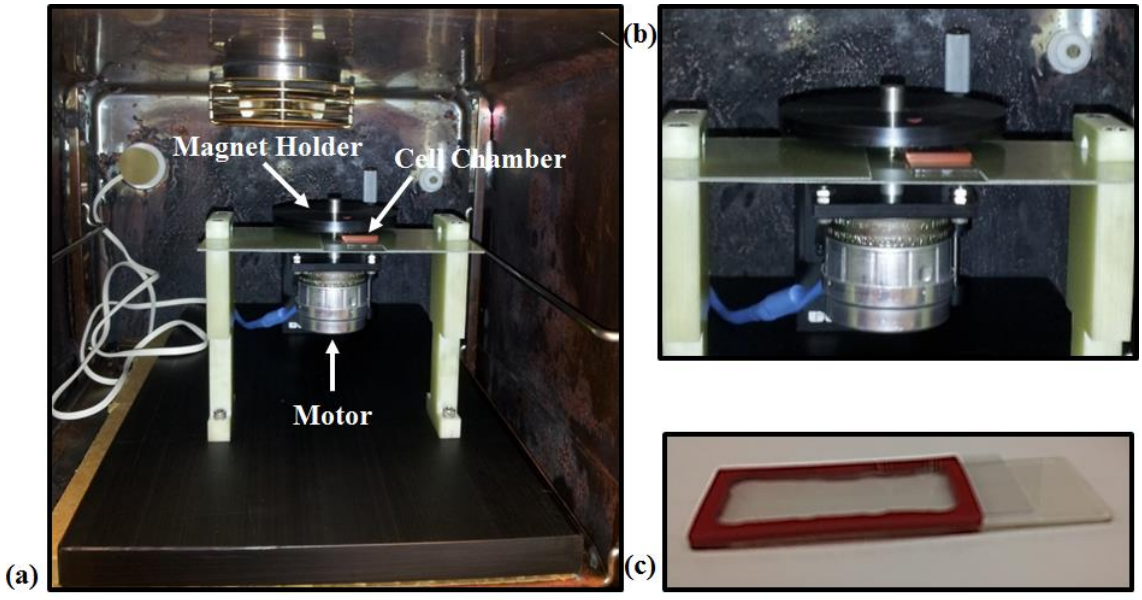

Figure 7-14 (a) Experimental setup of magnetic field gradient generator for cell studies, (b) Close-up of the experimental setup and, (c) Custom cell chamber.

7.6 EM Modeling of Static/AC Magnetic Modulator

The main purpose of the EM simulation was to calculate the force exerted by the gradient field on the cell. The simulation serves as a tool to validate, study and optimize the gradient field strength and the subsequent force exerted on the cells.

7.6.1 EM Modeling using COMSOL Multiphysics

All the simulations were carried out using the magnetic fields module of COMSOL Multiphysics 4.0 an interactive full-wave finite element based simulation [167]. As with any interactive simulation software, the user is responsible for the geometry definition, setting the material parameters, boundary conditions and identifying the source/excitation. COMSOL Multiphysics has the unique capacity to combine different modules in the same simulation file which enable the user to study the influence of multiple factors at the same time. Since the work here was primarily in static and very low frequency magnetic fields, our modules of interest were (i) AC/DC and (ii) Mathematics. AC/DC module in COMSOL is applicable when the size of the object is one-tenths smaller than the wavelength, $L < 0.1\lambda$.

Modeling the geometry in COMSOL Multiphysics starts with setting up the correct environment for the simulation which involves choosing the appropriate geometry space dimension, material parameters, physics definition, meshing, solver and post-processing. The first step is deciding the appropriate “Space Dimension” for the model ie., 2D or 3D modeling. All through the simulations a 3D geometry was used to model and capture the physics of the problem more accurately. For the “Physics”, two modules of COMSOL were utilized in the simulations, “Magnetic fields, no currents” from AC/DC module and “coefficient form PDE” from Mathematics module.

7.6.2 Simulation Geometry and Physics

The simulation geometry was drawn similar to the experimental setup and the design shown in Figure 7-13. After the geometry was drawn, the "Magnetic Field, No Currents" module was chosen from the AC/DC module, since the main goal was to study the magnetic field strength and gradient in the microscope slide. The magnetization strength of the four permanent magnets was defined through their known coercivity, Hc value. The magnetization direction can be varied to alter the orientation of the pole pairs. Flux conservation of the remaining geometry was defined through their respective material property. Shown in Figure 7-14 are the simulation results from COMSOL for the magnetic field strength and distribution in the ZX cut plane for the two configurations, Helmholtz and anti-Helmholtz of the magnets. The plate separation for the simulations was set at 4mm.

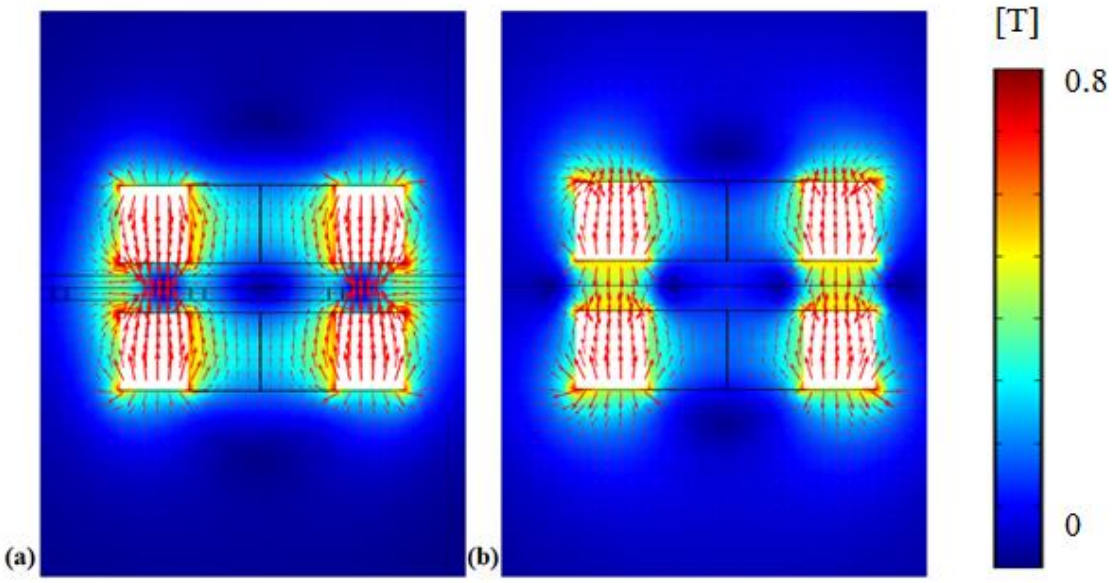

Figure 7-15 COMSOL simulation of the magnetic field distribution in (a) anti-Helmholtz and, (b) Helmholtz configuration.

As a first step, the distance between the two plates was optimized to identify the gradient peaks. Accordingly, the position of the microscope slide was also optimized to maximize the force exerted on the cells. Figure 7-15 shows the magnetic field strength and distribution in the XY cut plane for the two configurations, Helmholtz and anti-Helmholtz.

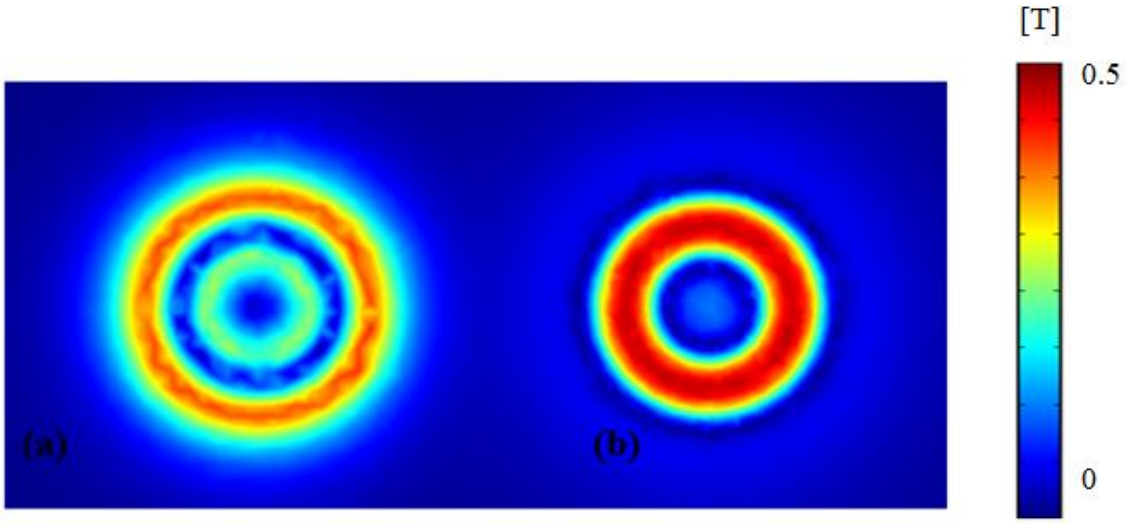

Figure 7-16 COMSOL simulation of the magnetic field distribution in (a) anti-Helmholtz and, (b) Helmholtz configuration.

7.6.3 Calculation and visualization of magnetic field gradient and force product

From the magnetic force of the field and gradient in Eq. 7.3, the gradient of the magnetic field which is a second order tensor can be written as

$$\nabla\vec{B} = \begin{pmatrix} \frac{\partial B_x}{\partial x} & \frac{\partial B_y}{\partial x} & \frac{\partial B_z}{\partial x} \\ \frac{\partial B_x}{\partial y} & \frac{\partial B_y}{\partial y} & \frac{\partial B_z}{\partial y} \\ \frac{\partial B_x}{\partial z} & \frac{\partial B_y}{\partial z} & \frac{\partial B_z}{\partial z} \end{pmatrix}. \tag{7.10}$$

The magnitude of a second order tensor was obtained by applying the square root of the inner product multiplication of the second order tensor,

$$\left|\nabla\vec{B}\right| = \sqrt{\nabla\vec{B} : \nabla\vec{B}} \text{ and} \tag{7.11}$$

$$\left|\nabla\vec{B}\right| = \left(\left(\frac{\partial B_x}{\partial x}\right)^2 + \left(\frac{\partial B_y}{\partial x}\right)^2 + \left(\frac{\partial B_z}{\partial x}\right)^2 + \left(\frac{\partial B_x}{\partial y}\right)^2 + \left(\frac{\partial B_y}{\partial y}\right)^2 + \left(\frac{\partial B_z}{\partial y}\right)^2 + \left(\frac{\partial B_x}{\partial z}\right)^2 + \left(\frac{\partial B_y}{\partial z}\right)^2 + \left(\frac{\partial B_z}{\partial z}\right)^2\right)^{1/2} . \quad (7.12)$$

In COMSOL simulation the x,y,z-component of the field gradient were computed in the "PDE" module as

$$\left|\nabla B_i\right| = \sqrt{\left(\frac{\partial B_i}{\partial x}\right)^2 + \left(\frac{\partial B_i}{\partial y}\right)^2 + \left(\frac{\partial B_i}{\partial z}\right)^2}, i = x, y, z . \quad (7.13)$$

In the field visualization the vector fields for each of the components (x,y,z) are denoted by $\left(\frac{\partial B_i}{\partial x}\right), \left(\frac{\partial B_i}{\partial y}\right), \left(\frac{\partial B_i}{\partial z}\right), i = x, y, z$ respectively as shown in Figure 7-17 along with the field gradient magnitude.

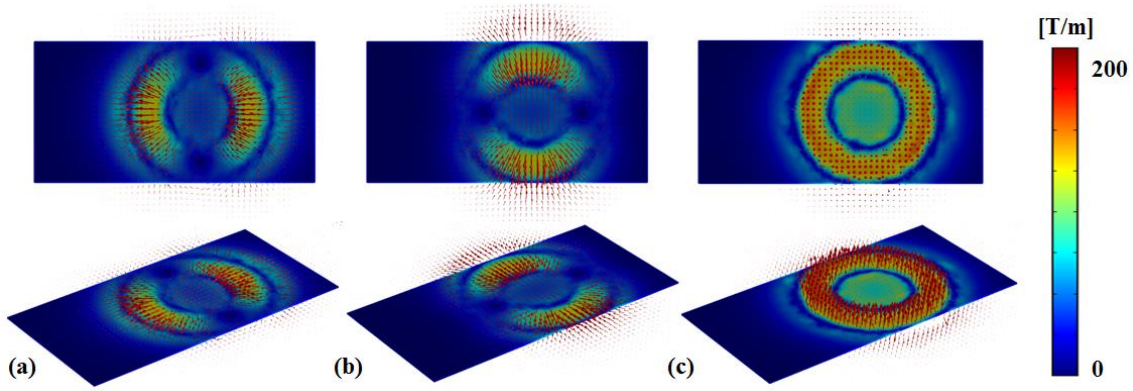

Figure 7-17 COMSOL simulation of the magnetic gradient $\nabla\vec{B}$ along (a) x-axis, (b) y-axis and, (c) z-axis. XY cut plane view of anti-helmholtz, units are in in T/m.

The force product from Eq. 7.5 was computed in COMSOL and the x,y,z components are represented as

$$G_i(B_i) = B_x \frac{\partial B_i}{\partial x} + B_y \frac{\partial B_i}{\partial y} + B_z \frac{\partial B_i}{\partial z}, i = x, y, z\ . \tag{7.14}$$

The vector fields for each of the components (x,y,z) are denoted by $B_x\left(\frac{\partial B_i}{\partial x}\right), B_y\left(\frac{\partial B_i}{\partial y}\right), B_z\left(\frac{\partial B_i}{\partial z}\right), i = x, y, z$ respectively as shown in Figure 7-18. Further, the force product was calculated in COMSOL for three different plate separations of 15mm, 12mm and 4mm. Figure 7-19 shows the decreasing trend of force product as a function of increasing plate distance. The inset describes the microscope slide orientation between the two anti-helmholtz magnets. As the distance between the two plates increases, the magnetic field decreases as a function of distance cube and hence the magnetic field gradient and consequentially the force product decreases dramatically. The values are extracted from COMSOL simulation run for three values of plate separation.

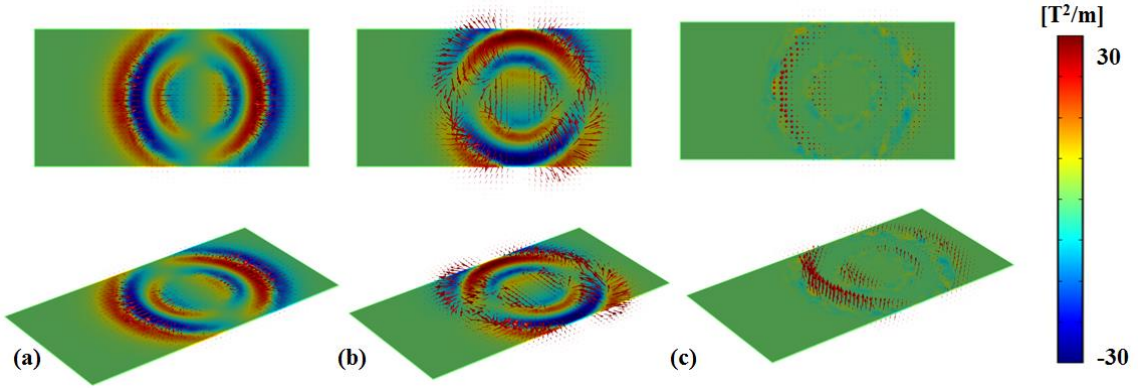

Figure 7-18 COMSOL simulation of the magnetic force product $\vec{G}(\vec{B}) = \vec{B} \bullet \nabla \vec{B}$ along (a) x-axis, (b) y-axis and, (c) z-axis. XY cut plane view of anti-helmholtz.

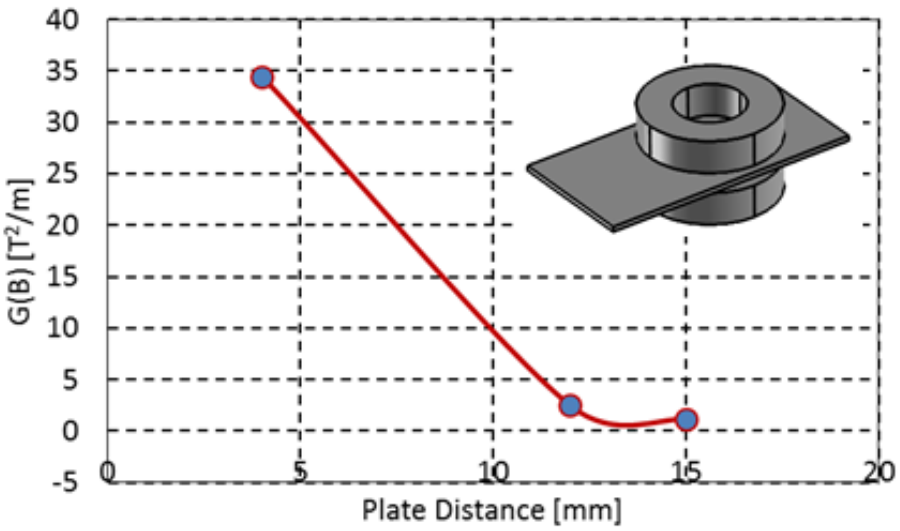

Figure 7-19 COMSOL simulation of the magnetic force product $\vec{G}(\vec{B}) = \vec{B} \bullet \nabla \vec{B}$ in T^2/m for anti-helmholtz configuration as a function of plate separation.

When placing cells on the microscope slide our interest lies in how the total magnetic gradient and force product is distributed in the sample area. From this "gradient/force map" we can predict what area in the sample region would experience the maximum effect from the magnetic force. Figure 7-20 shows the magnitude of the magnetic field gradient, with the vector fields given by $\left(\frac{\partial B_i}{\partial x}\right)+\left(\frac{\partial B_i}{\partial y}\right)+\left(\frac{\partial B_i}{\partial z}\right), i = x, y, z$. For example, summation of the x,y,z derivative of B_x denotes the x vector component in the simulation. Magnitude of the magnetic force product is shown in Figure 7-21, the vector fields given by $B_x\left(\frac{\partial B_i}{\partial x}\right)+B_y\left(\frac{\partial B_i}{\partial y}\right)+B_z\left(\frac{\partial B_i}{\partial z}\right), i = x, y, z$.

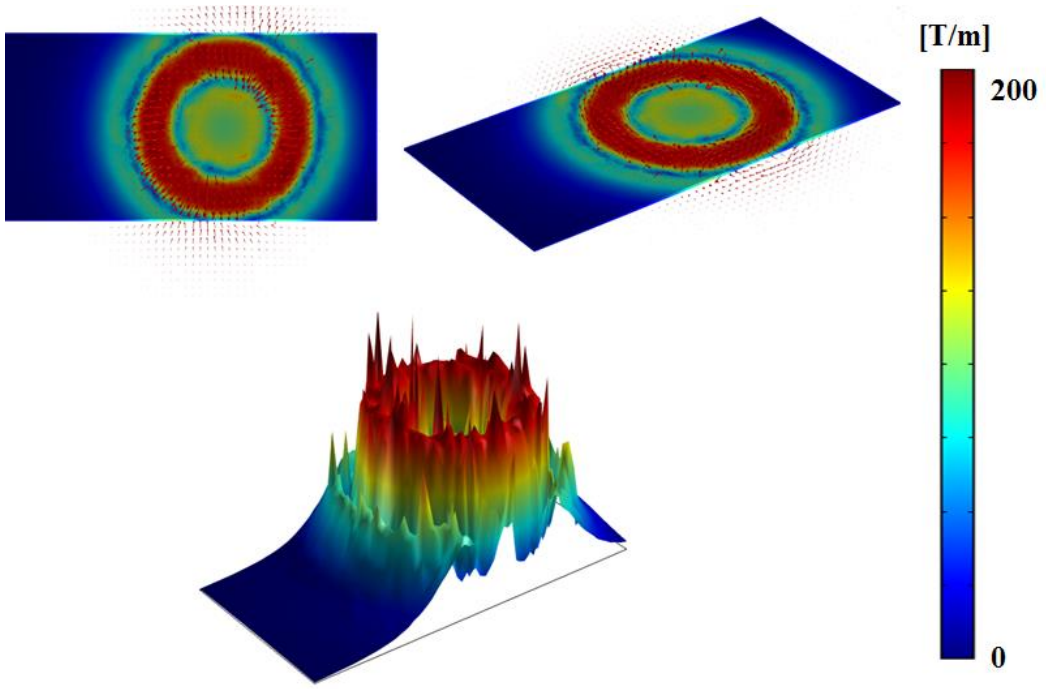

Figure 7-20 COMSOL simulation showing the magnitude of the magnetic gradient $\left|\nabla \vec{B}\right|$ in T/m (4 mm anti-helmholtz configuration).

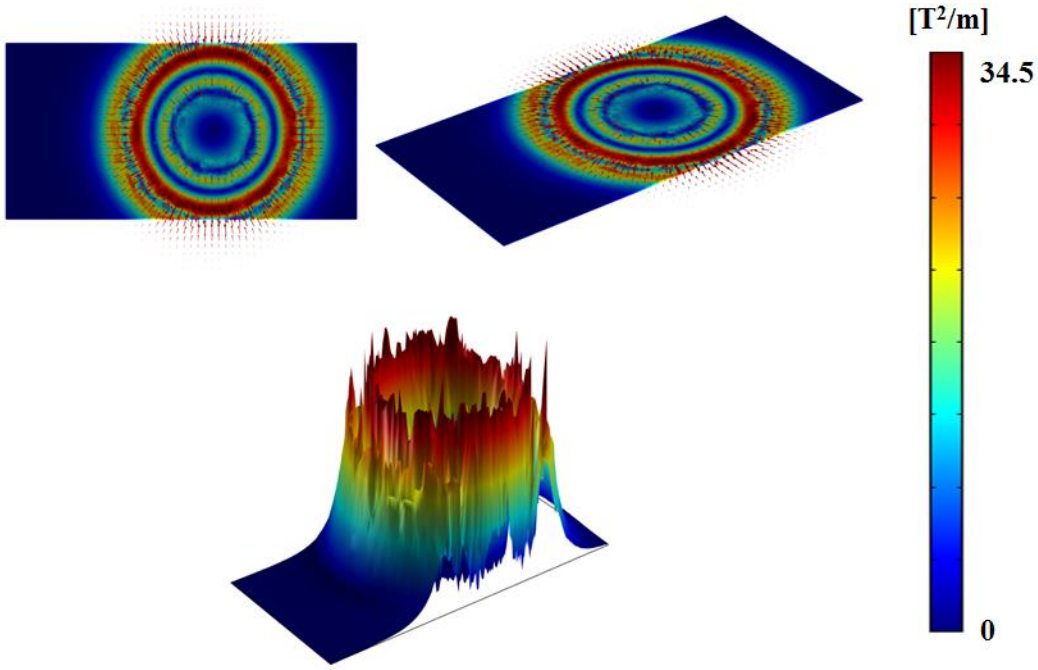

Figure 7-21 COMSOL simulation showing the magnitude of magnetic force product $\left|\vec{G}(\vec{B})\right| = \left|\vec{B}\bullet\nabla\vec{B}\right|$ in T^2/m (4 mm anti-helmholtz configuration).

7.7 Cell Studies using AsPC-1

Pancreatic adenocarcinoma cell line, AsPC-1 (ATCC® CRL-1682™) was obtained from American Type Culture Collection (ATCC). Cells were maintained in Dulbecco's modified Eagle's medium (DMEM) (Catalog No. 30–2002 from ATCC) with 10% fetal bovine serum (Catalog No.10091–148; Invitrogen). Cells were cultured in an atmosphere of 5% CO_2 in air in a humidified incubator at 37°C.

450,000 cells were seeded on a glass slide with a rubber spacer between it and the cover slip to allow cells to remain nourished in media throughout the course of the experiment. Cells were incubated for 24h so that reattachment to the surface of the slide would occur. 1720µL of media and 30µM of DRAQ7 was vortexed and added to the slide chamber after cells had been washed three times with media. 480 images of the brightfield and the DRAQ7 (Biostatus Ltd) channel (excitation/emission 633/655 nm) at 10x magnification with no space between frames were obtained of the whole slide using ImageXpress (Molecular Devices).

7.7.1 Magnetic field/gradient treatment of the AsPC-1 cells

We studied the effect of static magnetic force product, $\left|\vec{G}(\vec{B})\right| = \left|\left(\vec{B}\bullet\nabla\right)\vec{B}\right|$ on the AsPC-1 cell line. The effect of AC (sweeping) magnetic field, gradient and force product on the AsPC-1 cell line was studied. The effects studied were (i) no treatment, (ii) AC magnetic field with no MNPs, (iii) effect of MNPs with no AC field and (iv) combined effect of MNPs and AC magnetic field. To maximize the magnitude of magnetic field, gradient and consequentially the force product, the plate separation of the generator was optimally set at 4mm. However, to quantify the effect of force product on the cell death we studied 3 different plate separations of 14 mm, 5mm and 4 mm. The DRAQ7 which was

used to identify cell death before and after exposure were extracted using a segmentation protocol. DRAQ7 signals that were 1750/500 gray levels above the background pixel intensity and were sized between 10-50 μm^2 are segmented from the background and counted using MetaXpress software (Molecular Devices). The number of cells across the slide were counted using the brightfield images so that a percentage cell death measurement could be obtained

7.7.2 AC (sweeping) magnetic field treatment of the AsPC-1 cells

7.7.2a AsPC-1 with no treatment

In the first set of cell experiments, the control AsPC-1 slides were prepared. The cells were untreated with magnetic field/gradient exposure and MNPs. They were imaged once after DRAQ7 was added and once again after 30 minutes. The DRAQ7 signals from the cell chamber were color coded to generate the heat map in Figure 7-24a. As observed from the heat maps, the control cells are quite stable showing minimal background death. In the heat maps, red areas show maximum cell death while blue represent minimum cell death.

7.7.2b AC magnetic field with no MNPs

In the second step, the effect of AC magnetic field/gradient alone on the AsPC-1 cells viability was studied. The cells are imaged once imaged once before magnetic field/gradient exposure. The cells were then exposed to a sweeping magnetic field/gradient for a 30 minutes and were imaged once again after exposure. Figure 7-24b shows the heat maps of DRAQ7 signals imaged before AC exposure, after 30 minutes AC exposure. In the legend, white represents the area of maximum DRAQ7 signal i.e., cell death and red is

area of minimum signal. We do not observe significant increase in cell death after 30 minutes exposure of AC magnetic field/gradient.

7.7.2c Effect of MNPs with no AC magnetic field

In the next experiment, the cells were dosed with MNPs with no AC magnetic field/gradient exposure to observe for any MNP induced cell death. Here we used the same iron oxide nanorods that were checked for rotational movement in sub-chapter 7.6.2. We dosed the cells in the single cell chamber with 2.17×10^{10} iron oxide nanorods. The cell chamber was imaged before MNPs introduction. It was imaged again 30 minutes after dosing with MNPs to check for cell viability. Heat map of the before treatment, 30 minute particle exposure are shown in Figure 7-24c. We observe no significant increase in cell death with the introduction of MNPs. Thereby reducing the risk of cytotoxicity and cell death due to MNPs.

7.7.2d Combined effect of MNPs with AC magnetic field

In the final step, we combined the AC (sweeping) magnetic field/gradient along with the MNPs to maximize the force on the cell membrane. Due to the nanorods and sweeping magnetic field/gradient the cells experience a combination of rotational and translation force. The cells were dosed with 2.17×10^{10} iron oxide nanorods per cell chamber. The cells stained with DRAQ7 were imaged before AC field exposure. Then they were placed in the AC magnetic field/gradient system for a 30 minute and were imaged again. The experiment was repeated for 3 different plate separations i.e., magnetic gradient values. The heat maps of the before exposure and after exposure for 14 mm, 5 mm and 4 mm plate separation are shown in Figure 7-24d, Figure 7-24e and Figure 7-24f

respectively. From the after exposure heat maps we observe significant increase in cell death as the plate separation decreases i.e., the magnetic gradient increases.

The bright field image and the DRAQ7 image from the live imaging microscopy for two plate separations (i) 4 mm and (ii) 5 mm are shown in Figure 7-22 and Figure 7-23. From the live images we observe minimal cell death before any magnetic field/gradient exposure. Figure b shows the DRAQ7 image after the combined effect of MNPs and AC magnetic field/gradient. DRAQ7 enters the permiablized membrane to combine with the nucleus which appears as a white spot indicating cell death. From Figure 7-22b and Figure 7-23b we can observed an increased cell death i.e, increased DRAQ7 signals in the 4mm plate separation indicating the effect of high force product on cell death.

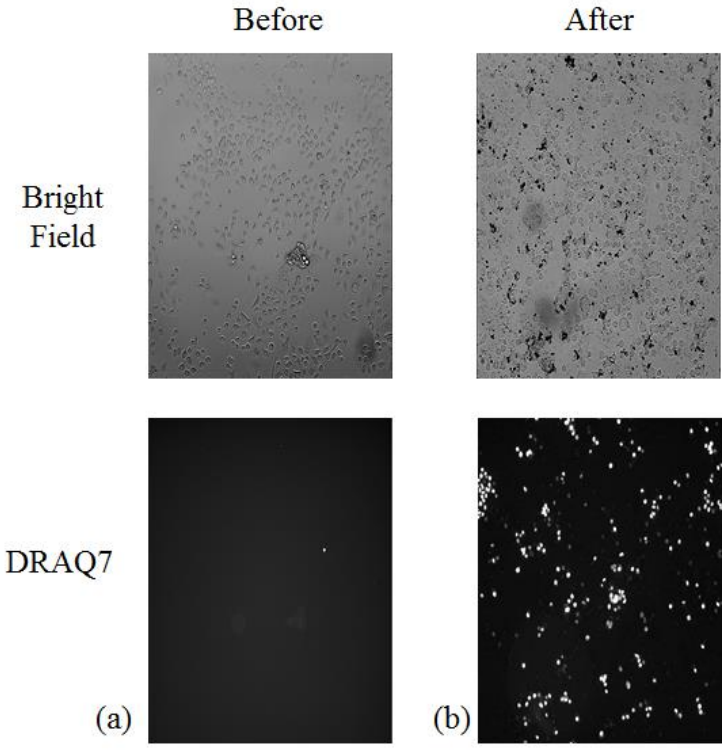

Figure 7-22 Live image microscopy of AsPC-1 (a) before field exposure, (b) with MNPs ac magnetic field/gradient exposure of 34 G(B) [T^2/m], 4 mm for 30 minutes.

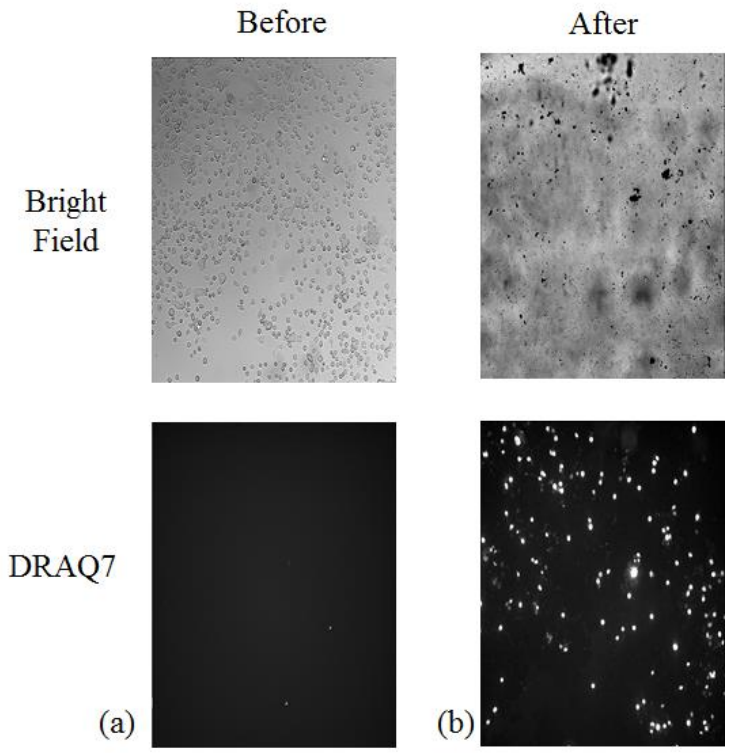

Figure 7-23 Live image microscopy of AsPC-1 (a) before field exposure, (b) with MNPs ac magnetic field/gradient exposure of 31 G(B) [T^2/m], 5 mm for 30 minutes.

The heat maps for the before and after exposure of the different cases are presented in Figure, where (a) no treatment, (b) AC magnetic field with no MNPs, (c) effect of MNPs with no AC field and (d) combined effect of MNPs and AC magnetic field/gradient for 14 mm plate separation, (e) combined effect of MNPs and AC magnetic field/gradient for 5 mm plate separation, and (f) combined effect of MNPs and AC magnetic field/gradient for 4 mm plate separation. We observed maximum cell death for the combined application of MNPs and magnetic field/gradient. Significant increase in cell death can be observed as the plate separation decreases i.e., force product increases.

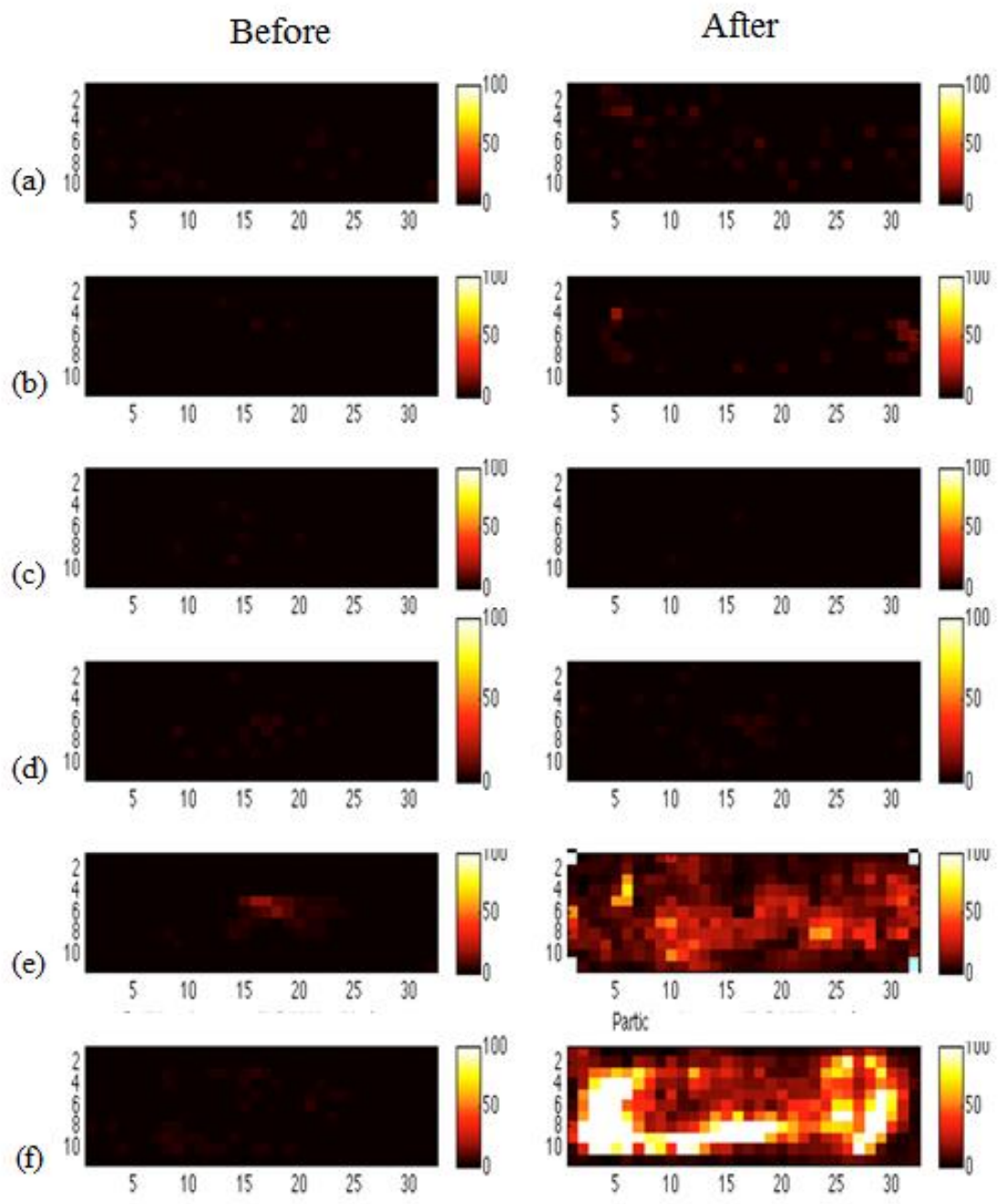

Figure 7-24 Heat map of AsPC-1 before and after exposure (a) no treatment, (b) with AC, no MNPs, (c) with MNPs, no AC, (d) 14 mm, AC and MNPs, (e) 5 mm, AC and MNPs, and(f) 4 mm, AC and MNPs.

To quantify the relation between cell death and magnetic gradient strength we calculate the percentage cell death as a function of force product for each plate separation.

Figure 7-25 shows a significant increase in percentage cell death as the force product increases.

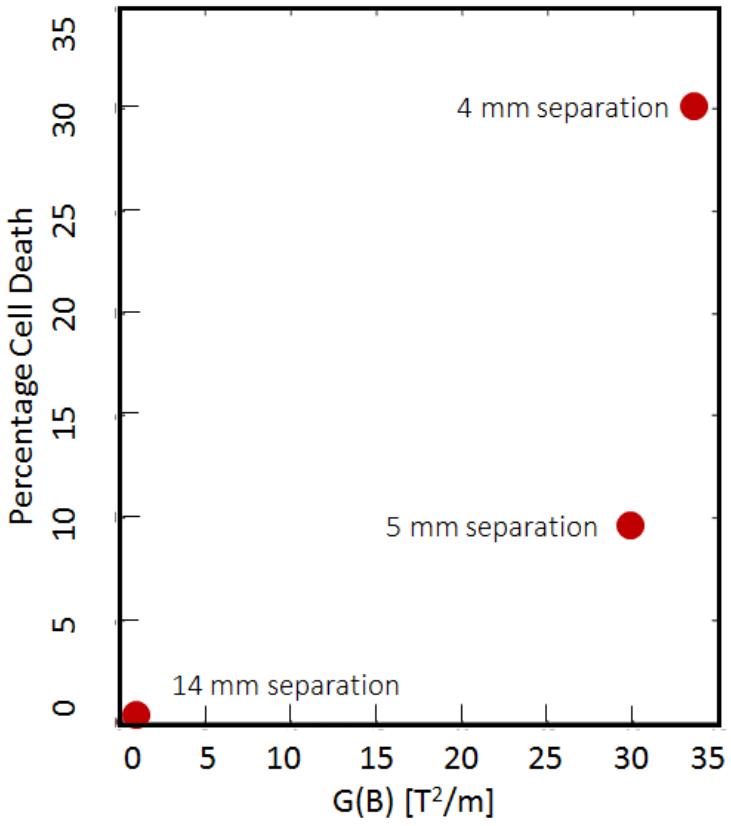

Figure 7-25 Percentage cell death as a function of force product for three different separations.

In this chapter, we explored a non-thermal approach to cancer therapy using magnetic field gradients. Cell apoptosis is caused by magnetic field/gradient induced mechanical stress on the cell microenvironment. A magnetic field/gradient generator was built to extend a multi-fold force on the cell membrane, (i) static magnetic field and static magnetic gradient combined "force-product", (ii) sweeping (ac) magnetic field and gradient, and (iii) MNPs as force-enhancers. As observed from the AsPC-1 cell experiments, increased magnetic field/gradient strength combined with MNPs induces maximum cell death. In our experiments, the MNPs experience multiple simultaneous

forces, (i) rotational motion due to static magnetic field, (ii) translational motion due to magnetic field gradient, (iii) translational and rotational motion due to sweeping (ac) magnetic field/gradient.

Chapter 8 Summary and Future Work

In this dissertation we comprehensively study the effect of magnetic field induced thermal and non-thermal therapeutics. Magnetic nanoparticles were characterization to evaluate their as role as "heat-enhancers" and "force-enhancers" in the thermal and non-thermal applications respectively. The therapeutic application of MNPs combined with magnetic field was investigated by employing a four-fold approach,

- Device development aimed at maximizing heat/ force enhancement with minimum input power. Design ensuring minimum systemic error contribution while effectively characterizing nanoparticles. Extensive system calibration was done to understand the system behavior and magnetic field dependencies.
- Physics of the interaction mechanism of the MNPs with the fields in the device. In case of thermal interaction of *rf* fields in the solenoid with the MNPs, the SAR discrepancies in literature were addressed. An extra electric field component in the solenoid was identified and its interaction with the MNPs microenvironment and consequentially the heat loss contribution to SAR was investigated. Rotational and translation force of MNPs due to magnetic fields, gradients and their non-thermal effects on the cell microenvironment was comprehensively studied.
- Electromagnetic simulations were carried out using HFSS, MAXWELL and COMSOL for each device developed. Field distributions, their individual components, vector properties and magnitude served a three-fold purpose of (a) validating the device development stage by visualizing the electric/magnetic fields in the system, (b) interpreting and analyzing the interaction mechanism of the MNPS with the fields, and (c) validating experimental data by analyzing the trends.

- Experimental analysis and verification of MNPs functional as heat/force enhancers in our devices. For inducing thermal effects, the SAR of the MNPs which is a direct measurement efficiency were extracted from measurements. The overestimation of SAR in the solenoid and its effect on MNPs accurate characterization and subsequently its impact on clinical trials were extensively verified. Further, a lower frequency solution was developed to remove the E_z/EDL interaction and provide a possible way to induce cancer cell death by targeting lower temperature gated ion channels. For verification of non-thermal effect, specifically force induced on the cell microenvironment, the rotational actuation of MNPs were experimentally established for very low frequencies (~Hz). Further, cancer cell studies on AsPC-1 were thoroughly conducted to show the significant cell death and their dependency on the magnetic force product.

The possible future work in the thermal therapy would be experimentally verifying the frequency, E_z/EDL and field strength effects on cancer cell apoptosis, specifically AsPC-1. Further, to quantify the MNPs combined magnetic field strength requirement on different cancer cell lines. The cell death comparison of cancer cells with healthy cell to monitor non-specific heating need to be carried out at both the higher (~MHz) and lower (~kHz) frequencies. For non-thermal therapy, the possibility and feasibility of utilizing magnetic gradients along with no MNPs to cause force induced cell apoptosis needs to be explored further. Comparison with the normal Human Pancreatic Ductal Epithelial (HPDE) cell line (along with Young's modulus studies could be performed to establish cancer cell selectivity of the magnetic force product.

References

[1] R. Siegel, J. Ma, Z. Zou, and A. Jemal, "Cancer Statistics, 2014," *CA: A Cancer Journal for Clinicians*, vol. 64, pp. 9-29, 2014.

[2] A. C. Society, *Cancer Facts & Figures*: The Society, 2014.

[3] C. D. Mathers and D. Loncar, "Projections of Global Mortality and Burden of Disease from 2002 to 2030," *PLoS medicine*, vol. 3, p. e442, 2006.

[4] D. M. Parkin, "Global Cancer Statistics in the Year 2000," *The lancet oncology*, vol. 2, pp. 533-543, 2001.

[5] R. A. Gatenby, "A Change of Strategy in the War on Cancer," *Nature*, vol. 459, pp. 508-509, 05/28/print 2009.

[6] W. Andrä and H. Nowak, *Magnetism in Medicine: A Handbook*: John Wiley & Sons, 2007.

[7] R. Habash, *Bioeffects and Therapeutic Applications of Electromagnetic Energy*: CRC press, 2007.

[8] D. A. Hodgson, I. B. Feldberg, N. Sharp, N. Cronin, M. Evans, and L. Hirschowitz, "Microwave Endometrial Ablation: Development, Clinical Trials and Outcomes at Three Years," *BJOG: An International Journal of Obstetrics & Gynaecology*, vol. 106, pp. 684-694, 1999.

[9] M. Noguchi, M. Earashi, H. Fujii, K. Yokoyama, K. i. Harada, and K. Tsuneyama, "Radiofrequency Ablation of Small Breast Cancer Followed by Surgical Resection," *Journal of surgical oncology*, vol. 93, pp. 120-128, 2006.

[10] C. L. Brace, "Radiofrequency and Microwave Ablation of the Liver, Lung, Kidney, and Bone: What Are the Differences?," *Current problems in diagnostic radiology,* vol. 38, pp. 135-143, 2009.

[11] Y. Liu, H. Miyoshi, and M. Nakamura, "Nanomedicine for Drug Delivery and Imaging: A Promising Avenue for Cancer Therapy and Diagnosis Using Targeted Functional Nanoparticles," *International Journal of Cancer,* vol. 120, pp. 2527-2537, 2007.

[12] M. Sebastian, N. Ninan, and E. Elias, *Nanomedicine and Cancer Therapies*: CRC Press, 2012.

[13] I. Brigger, C. Dubernet, and P. Couvreur, "Nanoparticles in Cancer Therapy and Diagnosis," *Advanced Drug Delivery Reviews,* vol. 54, pp. 631-651, 9/13/ 2002.

[14] M. C. Roco, "Nanotechnology: Convergence with Modern Biology and Medicine," *Current Opinion in Biotechnology*, vol. 14, pp. 337-346, 6// 2003.

[15] Q. A. Pankhurst, J. Connolly, S. K. Jones, and J. Dobson, "Applications of Magnetic Nanoparticles in Biomedicine," *J Phys D: Appl Phys,* vol. 36, p. R167, 2003.

[16] N. J. Sniadecki, "Minireview: A Tiny Touch: Activation of Cell Signaling Pathways with Magnetic Nanoparticles," *Endocrinology,* vol. 151, pp. 451-457, February 1, 2010 2010.

[17] I. A. Brezovich, "Low Frequency Hyperthermia: Capacitive and Ferromagnetic Thermoseed Methods," *Medical Physics Monograph,* vol. 16, pp. 82-111, 1988.

[18] A. Y. Cheung and A. Neyzari, "Deep Local Hyperthermia for Cancer Therapy: External Electromagnetic and Ultrasound Techniques," *Cancer Res,* vol. 44, pp. 4736s-4744s, Oct 1984.

[19] A. Jordan, P. Wust, H. Föhling, W. John, A. Hinz, and R. Felix, "Inductive Heating of Ferrimagnetic Particles and Magnetic Fluids: Physical Evaluation of Their Potential for Hyperthermia," *Int J Hypertherm,* vol. 25, pp. 499-511, 2009.

[20] H. Huang, S. Delikanli, H. Zeng, D. M. Ferkey, and A. Pralle, "Remote Control of Ion Channels and Neurons through Magnetic-Field Heating of Nanoparticles," *Nat Nano,* vol. 5, pp. 602-606, 2010.

[21] M. J. Gunthorpe, C. D. Benham, A. Randall, and J. B. Davis, "The Diversity in the Vanilloid (Trpv) Receptor Family of Ion Channels," *Trends in pharmacological sciences,* vol. 23, pp. 183-191, 2002.

[22] J. Dobson, S. H. Cartmell, A. Keramane, and A. J. E. Haj, "Principles and Design of a Novel Magnetic Force Mechanical Conditioning Bioreactor for Tissue Engineering, Stem Cell Conditioning, and Dynamic in Vitro Screening," *NanoBioscience, IEEE Transactions on,* vol. 5, pp. 173-177, 2006.

[23] N. Q. Balaban, U. S. Schwarz, D. Riveline, P. Goichberg, G. Tzur, I. Sabanay, D. Mahalu, S. Safran, A. Bershadsky, and L. Addadi, "Force and Focal Adhesion Assembly: A Close Relationship Studied Using Elastic Micropatterned Substrates," *Nature cell biology,* vol. 3, pp. 466-472, 2001.

[24] J. Stricker, Y. Aratyn-Schaus, Patrick W. Oakes, and Margaret L. Gardel, "Spatiotemporal Constraints on the Force-Dependent Growth of Focal Adhesions," *Biophysical Journal,* vol. 100, pp. 2883-2893.

[25] V. Zablotskii, T. Syrovets, Z. W. Schmidt, A. Dejneka, and T. Simmet, "Modulation of Monocytic Leukemia Cell Function and Survival by High Gradient Magnetic Fields and Mathematical Modeling Studies," *Biomaterials,* vol. 35, pp. 3164-3171, 2014.

[26] E. Beaugnon and R. Tournier, "Levitation of Organic Materials," *Nature,* vol. 349, 1991.

[27] D.-H. Kim, E. A. Rozhkova, I. V. Ulasov, S. D. Bader, T. Rajh, M. S. Lesniak, and V. Novosad, "Biofunctionalized Magnetic-Vortex Microdiscs for Targeted Cancer-Cell Destruction," *Nat Mater,* vol. 9, pp. 165-171, 2010.

[28] J. C. Lin, *Advances in Electromagnetic Fields in Living Systems*: Springer, 1994.

[29] C. Gabriel, S. Gabriel, and E. Corthout, "The Dielectric Properties of Biological Tissues: I. Literature Survey," *Physics in Medicine and Biology,* vol. 41, p. 2231, 1996.

[30] S. Gabriel, R. W. Lau, and C. Gabriel, "The Dielectric Properties of Biological Tissues: Ii. Measurements in the Frequency Range 10 Hz to 20 Ghz," *Physics in Medicine and Biology,* vol. 41, p. 2251, 1996.

[31] C. Furse, D. A. Christensen, and C. H. Durney, *Basic Introduction to Bioelectromagnetics*: CRC press, 2009.

[32] B. Greenebaum and F. S. Barnes, *Bioengineering and Biophysical Aspects of Electromagnetic Fields*: CRC press, 2006.

[33] R. K. Adair, "Biophysical Limits on Athermal Effects of Rf and Microwave Radiation," *Bioelectromagnetics,* vol. 24, pp. 39-48, 2003.

[34] Available: http://www.surgery.usc.edu/hepatobiliary/radiofrequencyablation.html

[35] J. L. Kirschvink, A. Kobayashi-Kirschvink, and B. J. Woodford, "Magnetite Biomineralization in the Human Brain," *Proceedings of the National Academy of Sciences,* vol. 89, pp. 7683-7687, 1992.

[36] P. Valberg, R. Kavet, and C. Rafferty, "Can Low-Level 50/60 Hz Electric and Magnetic Fields Cause Biological Effects?," *Radiation Research,* vol. 148, pp. 2-21, 1997.

[37] S. Weinbaum and L. Jiji, "A New Simplified Bioheat Equation for the Effect of Blood Flow on Local Average Tissue Temperature," *Journal of biomechanical engineering,* vol. 107, pp. 131-139, 1985.

[38] W. L. Nyborg, "Solutions of the Bio-Heat Transfer Equation," *Physics in medicine and biology,* vol. 33, p. 785, 1988.

[39] D. H. Sliney and B. E. Stuck, "Microwave Exposure Limits for the Eye: Applying Infrared Laser Threshold Data," in *Radiofrequency Radiation Standards*, ed: Springer, 1995, pp. 79-87.

[40] J. D. Hardy, H. G. Wolff, and H. Goodell, "Pain Sensations and Reactions," 1952.

[41] I. G. Zubal, C. R. Harrell, E. O. Smith, Z. Rattner, G. Gindi, and P. B. Hoffer, "Computerized Three-Dimensional Segmented Human Anatomy," *Medical physics,* vol. 21, pp. 299-302, 1994.

[42] P. Bernardi, M. Cavagnaro, S. Pisa, and E. Piuzzi, "Specific Absorption Rate and Temperature Increases in the Head of a Cellular-Phone User," *Microwave Theory and Techniques, IEEE Transactions on,* vol. 48, pp. 1118-1126, 2000.

[43] A. Straume, G. Oftedal, and A. Johnsson, "Skin Temperature Increase Caused by a Mobile Phone: A Methodological Infrared Camera Study," *Bioelectromagnetics,* vol. 26, pp. 510-519, 2005.

[44] J. E. Muscat, M. G. Malkin, S. Thompson, R. E. Shore, S. D. Stellman, D. McRee, A. I. Neugut, and E. L. Wynder, "Handheld Cellular Telephone Use and Risk of Brain Cancer," *Jama,* vol. 284, pp. 3001-3007, 2000.

[45] P. D. Inskip, R. E. Tarone, E. E. Hatch, T. C. Wilcosky, W. R. Shapiro, R. G. Selker, H. A. Fine, P. M. Black, J. S. Loeffler, and M. S. Linet, "Cellular-Telephone Use and Brain Tumors," *New England Journal of Medicine,* vol. 344, pp. 79-86, 2001.

[46] S. Lönn, A. Ahlbom, P. Hall, and M. Feychting, "Long-Term Mobile Phone Use and Brain Tumor Risk," *American journal of epidemiology,* vol. 161, pp. 526-535, 2005.

[47] G. C. Brainard, R. Kavet, and L. I. Kheifets, "The Relationship between Electromagnetic Field and Light Exposures to Melatonin and Breast Cancer Risk: A Review of the Relevant Literature," *Journal of pineal research,* vol. 26, pp. 65-100, 1999.

[48] O. P. Gandhi and X. B. Chen, "Specific Absorption Rates and Induced Current Densities for an Anatomy-Based Model of the Human for Exposure to Time-Varying Magnetic Fields of Mri," *Magnetic resonance in medicine,* vol. 41, pp. 816-823, 1999.

[49] D. Simunic, P. Wach, W. Renhart, and R. Stollberger, "Spatial Distribution of High-Frequency Electromagnetic Energy in Human Head During Mri: Numerical

Results and Measurements," *Biomedical Engineering, IEEE Transactions on,* vol. 43, p. 88, 1996.

[50] Z. Wang, J. C. Lin, W. Mao, W. Liu, M. B. Smith, and C. M. Collins, "Sar and Temperature: Simulations and Comparison to Regulatory Limits for Mri," *Journal of Magnetic Resonance Imaging,* vol. 26, pp. 437-441, 2007.

[51] F. G. Shellock, B. Rothman, and D. Sarti, "Heating of the Scrotum by High-Field-Strength Mr Imaging," *AJR. American journal of roentgenology,* vol. 154, pp. 1229-1232, 1990.

[52] F. G. Shellock and C. Schatz, "Increased Corneal Temperature Caused by Mr Imaging of the Eye with a Dedicated Local Coil," *Radiology,* vol. 185, pp. 697-699, 1992.

[53] F. G. Shellock, "Radiofrequency Energy-Induced Heating During Mr Procedures: A Review," *Journal of Magnetic Resonance Imaging,* vol. 12, pp. 30-36, 2000.

[54] C. Haarala, S. Aalto, H. Hautzel, L. Julkunen, J. O. Rinne, M. Laine, B. Krause, and H. Hämäläinen, "Effects of a 902 Mhz Mobile Phone on Cerebral Blood Flow in Humans: A Pet Study," *Neuroreport,* vol. 14, pp. 2019-2023, 2003.

[55] N. D. Volkow, D. Tomasi, G.-J. Wang, P. Vaska, J. S. Fowler, F. Telang, D. Alexoff, J. Logan, and C. Wong, "Effects of Cell Phone Radiofrequency Signal Exposure on Brain Glucose Metabolism," *Jama,* vol. 305, pp. 808-813, 2011.

[56] M. S. Kwon, V. Vorobyev, S. Kännälä, M. Laine, J. O. Rinne, T. Toivonen, J. Johansson, M. Teräs, H. Lindholm, and T. Alanko, "Gsm Mobile Phone Radiation Suppresses Brain Glucose Metabolism," *Journal of Cerebral Blood Flow & Metabolism,* vol. 31, pp. 2293-2301, 2011.

[57] A. Christ, W. Kainz, E. G. Hahn, K. Honegger, M. Zefferer, E. Neufeld, W. Rascher, R. Janka, W. Bautz, and J. Chen, "The Virtual Family—Development of Surface-Based Anatomical Models of Two Adults and Two Children for Dosimetric Simulations," *Physics in medicine and biology,* vol. 55, p. N23, 2010.

[58] L. G. Salford, A. E. Brun, J. L. Eberhardt, L. Malmgren, and B. R. Persson, "Nerve Cell Damage in Mammalian Brain after Exposure to Microwaves from Gsm Mobile Phones," *Environmental health perspectives,* vol. 111, p. 881, 2003.

[59] B. S. Jortner, "The Return of the Dark Neuron. A Histological Artifact Complicating Contemporary Neurotoxicologic Evaluation," *Neurotoxicology,* vol. 27, pp. 628-634, 2006.

[60] C. Aldinucci, J. B. Garcia, M. Palmi, G. Sgaragli, A. Benocci, A. Meini, F. Pessina, C. Rossi, C. Bonechi, and G. P. Pessina, "The Effect of Strong Static Magnetic Field on Lymphocytes," *Bioelectromagnetics,* vol. 24, pp. 109-117, 2003.

[61] J. Miyakoshi, "Effects of Static Magnetic Fields at the Cellular Level," *Progress in biophysics and molecular biology,* vol. 87, pp. 213-223, 2005.

[62] C. Alexiou, R. Schmid, R. Jurgons, M. Kremer, G. Wanner, C. Bergemann, E. Huenges, T. Nawroth, W. Arnold, and F. Parak, "Targeting Cancer Cells: Magnetic Nanoparticles as Drug Carriers," *European Biophysics Journal,* vol. 35, pp. 446-450, 2006/05/01 2006.

[63] H. Hirose, T. Nakahara, Q.-M. Zhang, S. Yonei, and J. Miyakoshi, "Static Magnetic Field with a Strong Magnetic Field Gradient (41.7 T/M) Induces C-Jun Expression in Hl-60 Cells," *In Vitro Cellular & Developmental Biology-Animal,* vol. 39, pp. 348-352, 2003.

[64] M. M. Vleugel, A. E. Greijer, R. Bos, E. van der Wall, and P. J. van Diest, "C-Jun Activation Is Associated with Proliferation and Angiogenesis in Invasive Breast Cancer," *Human Pathology,* vol. 37, pp. 668-674.

[65] J. R. Basford, "A Historical Perspective of the Popular Use of Electric and Magnetic Therapy," *Archives of physical medicine and rehabilitation,* vol. 82, pp. 1261-1269, 2001.

[66] M. Darendeliler, A. Darendeliler, and P. Sinclair, "Effects of Static Magnetic and Pulsed Electromagnetic Fields on Bone Healing," *The International journal of adult orthodontics and orthognathic surgery,* vol. 12, pp. 43-53, 1996.

[67] L. Fass, "Imaging and Cancer: A Review," *Molecular oncology,* vol. 2, pp. 115-152, 2008.

[68] D. Hanahan and R. A. Weinberg, "The Hallmarks of Cancer," *cell,* vol. 100, pp. 57-70, 2000.

[69] J. van der Zee, "Heating the Patient: A Promising Approach?," *Ann Oncol,* vol. 13, pp. 1173-1184, 2002.

[70] P. Carmeliet and R. K. Jain, "Angiogenesis in Cancer and Other Diseases," *Nature,* vol. 407, pp. 249-257, 2000.

[71] D. J. Chaplin, R. E. Durand, and P. L. Olive, "Acute Hypoxia in Tumors: Implications for Modifiers of Radiation Effects," *International Journal of Radiation Oncology*Biology*Physics,* vol. 12, pp. 1279-1282, 1986.

[72] J. M. Brown and A. J. Giaccia, "The Unique Physiology of Solid Tumors: Opportunities (and Problems) for Cancer Therapy," *Cancer Research,* vol. 58, pp. 1408-1416, April 1, 1998 1998.

[73] C. W. Song, "Effect of Local Hyperthermia on Blood Flow and Microenvironment: A Review," *Cancer Research,* vol. 44, pp. 4721s-4730s, 1984.

[74] Y. Guo, Y. Zhang, R. Klein, G. M. Nijm, A. V. Sahakian, R. A. Omary, G.-Y. Yang, and A. C. Larson, "Irreversible Electroporation Therapy in the Liver: Longitudinal Efficacy Studies in a Rat Model of Hepatocellular Carcinoma," *Cancer Research,* vol. 70, pp. 1555-1563, February 15, 2010 2010.

[75] A. Andreano, Y. Huang, M. F. Meloni, F. T. Lee, Jr., and C. Brace, "Microwaves Create Larger Ablations Than Radiofrequency When Controlled for Power in Ex Vivo Tissue," *Med Phys,* vol. 37, pp. 2967-73, Jun 2010.

[76] A. Golberg and M. L. Yarmush, "Nonthermal Irreversible Electroporation: Fundamentals, Applications, and Challenges," *Biomedical Engineering, IEEE Transactions on,* vol. 60, pp. 707-714, 2013.

[77] C. J. Simon, D. E. Dupuy, and W. W. Mayo-Smith, "Microwave Ablation: Principles and Applications1," *Radiographics,* vol. 25, pp. S69-S83, October 2005 2005.

[78] G. Carrafiello, D. Laganà, M. Mangini, F. Fontana, G. Dionigi, L. Boni, F. Rovera, S. Cuffari, and C. Fugazzola, "Microwave Tumors Ablation: Principles, Clinical Applications and Review of Preliminary Experiences," *International Journal of Surgery,* vol. 6, pp. S65-S69, 2008.

[79] M. Breton and L. M. Mir, "Microsecond and Nanosecond Electric Pulses in Cancer Treatments," *Bioelectromagnetics,* vol. 33, pp. 106-123, 2012.

[80] S. K. Frandsen, H. Gissel, P. Hojman, T. Tramm, J. Eriksen, and J. Gehl, "Direct Therapeutic Applications of Calcium Electroporation to Effectively Induce Tumor Necrosis," *Cancer research*, vol. 72, pp. 1336-1341, 2012.

[81] S. Elmore, "Apoptosis: A Review of Programmed Cell Death," *Toxicologic pathology*, vol. 35, pp. 495-516, 2007.

[82] S. L. Fink and B. T. Cookson, "Apoptosis, Pyroptosis, and Necrosis: Mechanistic Description of Dead and Dying Eukaryotic Cells," *Infection and Immunity*, vol. 73, pp. 1907-1916, April 1, 2005 2005.

[83] R. P. Feynman, "There's Plenty of Room at the Bottom," *Engineering and science*, vol. 23, pp. 22-36, 1960.

[84] G. A. Silva and V. Parpura, *Nanotechnology for Biology and Medicine: At the Building Block Level*: Springer, 2011.

[85] S. Azarmi, W. H. Roa, and R. Löbenberg, "Targeted Delivery of Nanoparticles for the Treatment of Lung Diseases," *Advanced drug delivery reviews*, vol. 60, pp. 863-875, 2008.

[86] J. R. Kanwar, X. Sun, V. Punj, B. Sriramoju, R. R. Mohan, S.-F. Zhou, A. Chauhan, and R. K. Kanwar, "Nanoparticles in the Treatment and Diagnosis of Neurological Disorders: Untamed Dragon with Fire Power to Heal," *Nanomedicine: Nanotechnology, Biology and Medicine*, vol. 8, pp. 399-414, 2012.

[87] J. Dobson, "Remote Control of Cellular Behaviour with Magnetic Nanoparticles," *Nat Nano*, vol. 3, pp. 139-143, 2008.

[88] S. Hughes, A. J. El Haj, and J. Dobson, "Magnetic Micro- and Nanoparticle Mediated Activation of Mechanosensitive Ion Channels," *Medical Engineering & Physics,* vol. 27, pp. 754-762, 2005.

[89] P. Decuzzi, B. Godin, T. Tanaka, S. Y. Lee, C. Chiappini, X. Liu, and M. Ferrari, "Size and Shape Effects in the Biodistribution of Intravascularly Injected Particles," *Journal of Controlled Release,* vol. 141, pp. 320-327, 2010.

[90] K. O'Grady, "Progress in Applications of Magnetic Nanoparticles in Biomedicine," *Journal of Physics D: Applied Physics,* vol. 42, pp. 220301-220301, 2009.

[91] Z. Liu, F. Kiessling, and J. Gatjens, "Advanced Nanomaterials in Multimodal Imaging: Design, Functionalization, and Biomedical Applications," *Journal of Nanomaterials,* vol. 2010, 2010.

[92] H. H. Kampinga, "Cell Biological Effects of Hyperthermia Alone or Combined with Radiation or Drugs: A Short Introduction to Newcomers in the Field," *International Journal of Hyperthermia,* vol. 22, pp. 191-196, 2006.

[93] B. Thiesen and A. Jordan, "Clinical Applications of Magnetic Nanoparticles for Hyperthermia," *International Journal of Hyperthermia,* vol. 24, pp. 467-474, 2008.

[94] P. Wust, U. Gneveckow, M. Johannsen, D. Böhmer, T. Henkel, F. Kahmann, J. Sehouli, R. Felix, J. Ricke, and A. Jordan, "Magnetic Nanoparticles for Interstitial Thermotherapy ‚Äì Feasibility, Tolerance and Achieved Temperatures," *Int J Hypertherm,* vol. 22, pp. 673-685, 2006.

[95] C. J. Gannon, P. Cherukuri, B. I. Yakobson, L. Cognet, J. S. Kanzius, C. Kittrell, R. B. Weisman, M. Pasquali, H. K. Schmidt, R. E. Smalley, and S. A. Curley,

"Carbon Nanotube-Enhanced Thermal Destruction of Cancer Cells in a Noninvasive Radiofrequency Field," *Cancer,* vol. 110, pp. 2654-2665, 2007.

[96] E. S. Glazer, C. Zhu, K. L. Massey, C. S. Thompson, W. D. Kaluarachchi, A. N. Hamir, and S. A. Curley, "Noninvasive Radiofrequency Field Destruction of Pancreatic Adenocarcinoma Xenografts Treated with Targeted Gold Nanoparticles," *Clinical Cancer Research,* vol. 16, pp. 5712-5721, December 1, 2010 2010.

[97] G. Hanson, R. Monreal, and S. P. Apell, "Electromagnetic Absorption Mechanisms in Metal Nanospheres: Bulk and Surface Effects in Radiofrequency-Terahertz Heating of Nanoparticles," *Journal of Applied Physics,* vol. 109, p. 124306, 2011.

[98] C. Lourenco, M. Teixeira, S. Simões, and R. Gaspar, "Steric Stabilization of Nanoparticles: Size and Surface Properties," *International journal of pharmaceutics,* vol. 138, pp. 1-12, 1996.

[99] R. Roa, F. Carrique, and E. Ruiz-Reina, "Electric Double Layer for Spherical Particles in Salt-Free Concentrated Suspensions Including Ion Size Effects," *Physical Chemistry Chemical Physics,* vol. 13, pp. 3960-3968, 2011.

[100] J. Jiang, G. Oberdörster, and P. Biswas, "Characterization of Size, Surface Charge, and Agglomeration State of Nanoparticle Dispersions for Toxicological Studies," *Journal of Nanoparticle Research,* vol. 11, pp. 77-89, 2009.

[101] S. Mornet, S. Vasseur, F. Grasset, and E. Duguet, "Magnetic Nanoparticle Design for Medical Diagnosis and Therapy," *Journal of Materials Chemistry,* vol. 14, pp. 2161-2175, 2004.

[102] S.-J. Park, S. Kim, S. Lee, Z. G. Khim, K. Char, and T. Hyeon, "Synthesis and Magnetic Studies of Uniform Iron Nanorods and Nanospheres," *Journal of the American Chemical Society,* vol. 122, pp. 8581-8582, 2000.

[103] Y. S. Kang, S. Risbud, J. F. Rabolt, and P. Stroeve, "Synthesis and Characterization of Nanometer-Size Fe3o4 and Γ-Fe2o3 Particles," *Chemistry of Materials,* vol. 8, pp. 2209-2211, 1996.

[104] B. M. Moskowitz, "Hitchhiker's Guide to Magnetism," in *Environmental Magnetism Workshop (IRM),* 1991, p. 48.

[105] R. E. Rosensweig, "Heating Magnetic Fluid with Alternating Magnetic Field," *J Magnetism Magnetic Mat,* vol. 252, pp. 370-374, 2002.

[106] M. Suto, Y. Hirota, H. Mamiya, A. Fujita, R. Kasuya, K. Tohji, and B. Jeyadevan, "Heat Dissipation Mechanism of Magnetite Nanoparticles in Magnetic Fluid Hyperthermia," *Journal of Magnetism and Magnetic Materials,* vol. 321, pp. 1493-1496, 2009.

[107] T. Tanaka, B. Godin, R. Bhavane, R. Nieves-Alicea, J. Gu, X. Liu, C. Chiappini, J. R. Fakhoury, S. Amra, and A. Ewing, "In Vivo Evaluation of Safety of Nanoporous Silicon Carriers Following Single and Multiple Dose Intravenous Administrations in Mice," *International Journal of Pharmaceutics,* vol. 402, pp. 190-197, 2010.

[108] E. Tasciotti, X. Liu, R. Bhavane, K. Plant, A. D. Leonard, B. K. Price, M. M.-C. Cheng, P. Decuzzi, J. M. Tour, F. Robertson, and M. Ferrari, "Mesoporous Silicon Particles as a Multistage Delivery System for Imaging and Therapeutic Applications," *Nature Nanotechnology,* vol. 3, pp. 151-157, 2008.

[109] H. Ansoft, "Ver. 12," *Ansoft Corporation, Canonsburg, PA,* 2010.

[110] M. Kallumadil, M. Tada, T. Nakagawa, M. Abe, P. Southern, and Q. A. Pankhurst, "Suitability of Commercial Colloids for Magnetic Hyperthermia," *J Magnetism Magnetic Mat,* vol. 321, pp. 1509-1513, 2009.

[111] T. Z. Wong, J. W. Strohbehn, K. M. Jones, J. A. Mechling, and B. S. Trembly, "Sar Patterns from an Interstitial Microwave Antenna-Array Hyperthermia System," *IEEE Transactions on Microwave Theory and Techniques,* vol. 34, pp. 560-567, 1986.

[112] P. Cherukuri, E. S. Glazer, and S. A. Curley, "Targeted Hyperthermia Using Metal Nanoparticles," *Advanced Drug Delivery Reviews,* vol. 62, pp. 339-345, 2010.

[113] Y. Yuan and D. Tasciuc, "Comparison between Experimental and Predicted Specific Absorption Rate of Functionalized Iron Oxide Nanoparticle Suspensions," *J Magnetism Magnetic Mat,* vol. 323, pp. 2463-2469, 2011.

[114] I. Baker, Q. Zeng, W. Li, and C. R. Sullivan, "Heat Deposition in Iron Oxide and Iron Nanoparticles for Localized Hyperthermia," vol. 99, p. 08H106, 2006.

[115] J. H. Lee, J. Jang, J. Choi, S. H. Moon, S. Noh, J. Kim, J. G. Kim, I. S. Kim, K. I. Park, and J. Cheon, "Exchange-Coupled Magnetic Nanoparticles for Efficient Heat Induction," *Nat Nano,* vol. 6, pp. 418-422, 2011.

[116] X. Wang, H. Gu, and Z. Yang, "The Heating Effect of Magnetic Fluids in an Alternating Magnetic Field," *J Magnetism Magnetic Mat,* vol. 293, pp. 334-340, 2005.

[117] S. Laurent, S. Dutz, U. O. H‰feli, and M. Mahmoudi, "Magnetic Fluid Hyperthermia: Focus on Superparamagnetic Iron Oxide Nanoparticles," *Advances in Colloid and Interface Science,* vol. 166, pp. 8-23, 2011.

[118] S. Purushotham and R. V. Ramanujan, "Modeling the Performance of Magnetic Nanoparticles in Multimodal Cancer Therapy," *Journal of Applied Physics,* vol. 107, pp. 114701-114701-9, 2010.

[119] F. S. Chute and F. E. Vermeulen, "A Visual Demonstration of the Electric Field of a Coil Carrying a Time-Varying Current," *Education, IEEE Transactions on,* vol. 24, pp. 278-283, 1981.

[120] B. Park, A. G. Webb, and C. M. Collins, "A Method to Separate Conservative and Magnetically-Induced Electric Fields in Calculations for Mri and Mrs in Electrically-Small Samples," *J Magnet Resonance,* vol. 199, pp. 233-237, 2009.

[121] S. Laurent, S. Dutz, U. O. Hofeli, and M. Mahmoudi, "Magnetic Fluid Hyperthermia: Focus on Superparamagnetic Iron Oxide Nanoparticles," *Adv Colloid Interface Sci,* vol. 166, pp. 8-23, 2011.

[122] S. Purushotham and R. V. Ramanujan, "Modeling the Performance of Magnetic Nanoparticles in Multimodal Cancer Therapy," *J Appl Phys,* vol. 107, pp. 114701-114701-9, 2010.

[123] J. Wosik, R. Pande, L. Xie, D. Ketharnath, S. Srinivasan, and B. Godin, "Protein Adsorption Enhanced Radio-Frequency Heating of Silica Nanoparticles," *Applied physics letters,* vol. 103, p. 043706, 2013.

[124] D. Ketharnath, R. Pande, L. Xie, S. Srinivasan, B. Godin, and J. Wosik, "A Method to Measure Specific Absorption Rate of Nanoparticles in Colloidal Suspension Using Different Configurations of Radio-Frequency Fields," *Applied physics letters,* vol. 101, p. 083118, 2012.

[125] A. Ito, Y. Kuga, H. Honda, H. Kikkawa, A. Horiuchi, Y. Watanabe, and T. Kobayashi, "Magnetite Nanoparticle-Loaded Anti-Her2 Immunoliposomes for Combination of Antibody Therapy with Hyperthermia," *Cancer letters,* vol. 212, pp. 167-175, 2004.

[126] A. Jordan, R. Scholz, P. Wust, H. Schirra, T. Schiestel, H. Schmidt, and R. Felix, "Endocytosis of Dextran and Silan-Coated Magnetite Nanoparticles and the Effect of Intracellular Hyperthermia on Human Mammary Carcinoma Cells in Vitro," *Journal of Magnetism and Magnetic Materials,* vol. 194, pp. 185-196, 1999.

[127] R. Hergt and S. Dutz, "Magnetic Particle Hyperthermia—Biophysical Limitations of a Visionary Tumour Therapy," *Journal of Magnetism and Magnetic Materials,* vol. 311, pp. 187-192, 2007.

[128] F. Maingret, I. Lauritzen, A. J. Patel, C. Heurteaux, R. Reyes, F. Lesage, M. Lazdunski, and E. Honoré, "Trek-1 Is a Heat-Activated Background K+ Channel," *The EMBO journal,* vol. 19, pp. 2483-2491, 2000.

[129] A. Dhaka, V. Viswanath, and A. Patapoutian, "Trp Ion Channels and Temperature Sensation," *Annu. Rev. Neurosci.,* vol. 29, pp. 135-161, 2006.

[130] D. E. Clapham, "Trp Channels as Cellular Sensors," *Nature,* vol. 426, pp. 517-524, 2003.

[131] T. Voets, G. Droogmans, U. Wissenbach, A. Janssens, V. Flockerzi, and B. Nilius, "The Principle of Temperature-Dependent Gating in Cold-and Heat-Sensitive Trp Channels," *Nature,* vol. 430, pp. 748-754, 2004.

[132] D. Kajfez, *Q-Factor*: Wiley Online Library, 2005.

[133] A. Van den Bossche, V. Valchev, and T. Filchev, "Improved Approximation for Fringing Permeances in Gapped Inductors," in *Industry Applications Conference, 2002. 37th IAS Annual Meeting. Conference Record of the*, 2002, pp. 932-938.

[134] A. M. Version, "15.0. 0," ed: Ansys, Inc., Canonsburg, PA.

[135] M. Ghibaudo, L. Trichet, J. Le Digabel, A. Richert, P. Hersen, and B. Ladoux, "Substrate Topography Induces a Crossover from 2d to 3d Behavior in Fibroblast Migration," *Biophysical Journal*, vol. 97, pp. 357-368.

[136] B. Ladoux and A. Nicolas, "Physically Based Principles of Cell Adhesion Mechanosensitivity in Tissues," *Reports on Progress in Physics*, vol. 75, p. 116601, 2012.

[137] P. A. Janmey, "The Cytoskeleton and Cell Signaling: Component Localization and Mechanical Coupling," *Physiol Rev*, vol. 78, pp. 763-81, Jul 1998.

[138] J. Liu, Y. Wang, X. Yuan, Y. Feng, and H. Liu, "Cyclic-Stretch Induces the Apoptosis of Myoblast by Activation of Caspase-3 Protease in a Magnitude-Dependent Manner," *Int J Biochem Cell Biol*, vol. 42, pp. 2004-11, Dec 2010.

[139] S. Oh, D. Kwon, H. J. Lee, J. Kim, and E. Lee, "Role of Elevated Pressure in Trail-Induced Apoptosis in Human Lung Carcinoma Cells," *Apoptosis*, vol. 15, pp. 1517-28, Dec 2010.

[140] F. Boccafoschi, M. Sabbatini, M. Bosetti, and M. Cannas, "Overstressed Mechanical Stretching Activates Survival and Apoptotic Signals in Fibroblasts," *Cells Tissues Organs*, vol. 192, pp. 167-76, 2010.

[141] J. T. Finer, R. M. Simmons, and J. A. Spudich, "Single Myosin Molecule Mechanics: Piconewton Forces and Nanometre Steps," *Nature,* vol. 368, pp. 113-119, 1994.

[142] A. E. Knight, C. Veigel, C. Chambers, and J. E. Molloy, "Analysis of Single-Molecule Mechanical Recordings: Application to Acto-Myosin Interactions," *Progress in Biophysics and Molecular Biology,* vol. 77, pp. 45-72, // 2001.

[143] C. Grashoff, B. D. Hoffman, M. D. Brenner, R. Zhou, M. Parsons, M. T. Yang, M. A. McLean, S. G. Sligar, C. S. Chen, and T. Ha, "Measuring Mechanical Tension across Vinculin Reveals Regulation of Focal Adhesion Dynamics," *Nature,* vol. 466, pp. 263-266, 2010.

[144] S. Deguchi, T. Ohashi, and M. Sato, "Tensile Properties of Single Stress Fibers Isolated from Cultured Vascular Smooth Muscle Cells," *Journal of Biomechanics,* vol. 39, pp. 2603-2610.

[145] P. A. Giardini, D. A. Fletcher, and J. A. Theriot, "Compression Forces Generated by Actin Comet Tails on Lipid Vesicles," *Proceedings of the National Academy of Sciences,* vol. 100, pp. 6493-6498, May 27, 2003 2003.

[146] V. Noireaux, R. M. Golsteyn, E. Friederich, J. Prost, C. Antony, D. Louvard, and C. Sykes, "Growing an Actin Gel on Spherical Surfaces," *Biophysical Journal,* vol. 78, pp. 1643-1654.

[147] A. Crow, Kevin D. Webster, E. Hohlfeld, Win P. Ng, P. Geissler, and Daniel A. Fletcher, "Contractile Equilibration of Single Cells to Step Changes in Extracellular Stiffness," *Biophysical Journal,* vol. 102, pp. 443-451.

[148] D. Mitrossilis, J. Fouchard, A. Guiroy, N. Desprat, N. Rodriguez, B. Fabry, and A. Asnacios, "Single-Cell Response to Stiffness Exhibits Muscle-Like Behavior," *Proceedings of the National Academy of Sciences,* vol. 106, pp. 18243-18248, October 27, 2009 2009.

[149] O. Chaudhuri, S. H. Parekh, W. A. Lam, and D. A. Fletcher, "Combined Atomic Force Microscopy and Side-View Optical Imaging for Mechanical Studies of Cells," *Nature methods,* vol. 6, pp. 383-387, 2009.

[150] D. J. Müller and Y. F. Dufrêne, "Atomic Force Microscopy: A Nanoscopic Window on the Cell Surface," *Trends in cell biology,* vol. 21, pp. 461-469, 2011.

[151] O. Valiron, L. Peris, G. Rikken, A. Schweitzer, Y. Saoudi, C. Rémy, and D. Job, "Cellular Disorders Induced by High Magnetic Fields," *Journal of Magnetic Resonance Imaging,* vol. 22, pp. 334-340, 2005.

[152] O. A. Kuznetsov and K. H. Hasenstein, "Intracellular Magnetophoresis of Amyloplasts and Induction of Root Curvature," *Planta,* vol. 198, pp. 87-94, 1996.

[153] M. Yamaguchi and Y. Tanimoto, "Magneto-Science," *Magneto-Science: Magnetic Field Effects on Materials: Fundamentals and Applications, Springer Series in Materials Science, Volume 89. ISBN 978-3-540-37061-1. Kodansha Ltd. and Springer-Verlag Berlin Heidelberg, 2006,* vol. 1, 2006.

[154] A.-R. Qian, X. Gao, W. Zhang, J.-B. Li, Y. Wang, S.-M. Di, L.-F. Hu, and P. Shang, "Large Gradient High Magnetic Fields Affect Osteoblast Ultrastructure and Function by Disrupting Collagen I or Fibronectin/Aβ1 Integrin," *PloS one,* vol. 8, p. e51036, 2013.

[155] D. Shi, R. Meng, W. Deng, W. Ding, Q. Zheng, W. Yuan, L. Liu, C. Zong, P. Shang, and J. Wang, "Effects of Microgravity Modeled by Large Gradient High Magnetic Field on the Osteogenic Initiation of Human Mesenchymal Stem Cells," *Stem Cell Reviews and Reports,* vol. 6, pp. 567-578, 2010.

[156] R. J. Mannix, S. Kumar, F. Cassiola, M. Montoya-Zavala, E. Feinstein, M. Prentiss, and D. E. Ingber, "Nanomagnetic Actuation of Receptor-Mediated Signal Transduction," *Nat Nano,* vol. 3, pp. 36-40, 2008.

[157] R. Cowburn, D. Koltsov, A. Adeyeye, M. Welland, and D. Tricker, "Single-Domain Circular Nanomagnets," *Physical Review Letters,* vol. 83, p. 1042, 1999.

[158] T. Fischbacher, M. Franchin, G. Bordignon, and H. Fangohr, "A Systematic Approach to Multiphysics Extensions of Finite-Element-Based Micromagnetic Simulations: Nmag," *Magnetics, IEEE Transactions on,* vol. 43, pp. 2896-2898, 2007.

[159] J. Schöberl, J. Gerstmayr, and R. Gaisbauer, "Netgen - Automatic 3d Tetrahedral Mesh Generator," ed, 2003.

[160] P. Ramachandran and G. Varoquaux, "Mayavi: 3d Visualization of Scientific Data," *Computing in Science & Engineering,* vol. 13, pp. 40-51, 2011.

[161] H. Fei, Z. Peng, L. Li, Y. Yang, W. Lu, E. L. Samuel, X. Fan, and J. M. Tour, "Preparation of Carbon-Coated Iron Oxide Nanoparticles Dispersed on Graphene Sheets and Applications as Advanced Anode Materials for Lithium-Ion Batteries," *Nano Research,* vol. 7, pp. 1-9, 2014.

[162] D. V. Kosynkin, A. L. Higginbotham, A. Sinitskii, J. R. Lomeda, A. Dimiev, B. K. Price, and J. M. Tour, "Longitudinal Unzipping of Carbon Nanotubes to Form Graphene Nanoribbons," *Nature,* vol. 458, pp. 872-876, 2009.

[163] J. F. Schenck, "Physical Interactions of Static Magnetic Fields with Living Tissues," *Progress in biophysics and molecular biology,* vol. 87, pp. 185-204, 2005.

[164] J. F. Schenck, C. Dumoulin, R. Redington, H. Kressel, R. Elliott, and I. McDougall, "Human Exposure to 4.0-Tesla Magnetic Fields in a Whole-Body Scanner," *Medical physics,* vol. 19, pp. 1089-1098, 1992.

[165] A. Winkleman, K. L. Gudiksen, D. Ryan, G. M. Whitesides, D. Greenfield, and M. Prentiss, "A Magnetic Trap for Living Cells Suspended in a Paramagnetic Buffer," *Applied physics letters,* vol. 85, pp. 2411-2413, 2004.

[166] S. S. Shevkoplyas, A. C. Siegel, R. M. Westervelt, M. G. Prentiss, and G. M. Whitesides, "The Force Acting on a Superparamagnetic Bead Due to an Applied Magnetic Field," *Lab on a chip,* vol. 7, pp. 1294-1302, 2007.

[167] C. Multiphysics, "User's Guide," *Version,* vol. 4, pp. 290-298, 2007.